CARBON ISOTOPE FUSION

thesis by

Stephen Trentalange

In Partial Fulfillment of the Requirements
For the Degree of
Doctor of Philosophy

California Institute of Technology
Pasadena, California
1983

(Submitted: December 10, 1982)

ACKNOWLEDGEMENTS

This research was supported in part by the National Science Foundation under Grant No. PHY79-23638.

I would like to thank Mark, Donna, Michael and Paul, my brothers and sister, and my father, who asked me perhaps the most fundamental question of all...."Why the hell don't you become a doctor?"

I would also like to thank my teachers: Charley Barnes and Steve Koonin, who taught me how difficult it is to *know* something; Tsutomu Ohshima, who taught me how difficult it is to *be* something, and also Paul Yergin, who I know loves me...no matter who I am.

There were those who stood by me during times of difficulty. I can only say how much their help meant to me, especially Kevin Ashby, Lisa Baylis, Joseph Caner, Minoru Furuyama, Stuart Goodnik, and Barbara Lamprecht, for their friendship; Bradley Flanders, Nai Kwong, and Daniel Wenkert, for teaching me many things; Barbara Cooper, Roy Williams, and Michelle Vine, for laboring and laughing with me, lo, these many years; Sandra Hyland, for walking with me every step of the way; and Marlow Fisher, for being there when I needed him.

ABSTRACT

The $^{13}C+^{13}C$ total fusion cross section has been determined in the range $3.26 \leq E_{c.m.} \leq 8.0$ MeV using Ge(Li) detector measurements of low-lying transitions in the residual nuclei and a statistical model calculation of excited state populations. Six different residual nuclei have been observed and their production yields are given. To constrain the parameters in fusion models for these reactions, we have also taken elastic scattering data at $\vartheta_{c.m.} = 60°$, 70°, 80°, and 90° for $4.5 \leq E_{c.m.} \leq 8.5$ MeV, as well as angular distributions at $E_{c.m.} = 7$ and 8 MeV. The relationship of low energy scattering and reaction cross sections among the carbon isotopes is discussed.

TABLE OF CONTENTS

TABLE OF CONTENTS (cont.)

I. Heavy Ion Reactions

A. Introduction

This thesis will discuss low energy measurements of the reactions $^{13}C+^{13}C$, $^{12}C+^{13}C$, and $^{12}C+^{12}C$. These systems lie in an area of nuclear science known as "light heavy-ion physics," comprising collisions between pairs in the approximate mass range $9 < A < 40$. For such a large number of nucleons one does not ordinarily demand a complete microscopic description of the reaction, and there is a natural division of reaction mechanisms into direct and compound nuclear. Direct reactions are those involving the transfer or excitation of only a few nucleons, while the nuclei remain relatively distinct. Analysis of direct reactions ultimately requires an understanding of the transition operators and/or some detailed knowledge of the internal nuclear structure. Compound processes occur when nuclei mingle more closely. In very heavy systems, compound nuclear reactions are described by simple macroscopic quantities such as charge, mass, and level density at high excitation energy. For the systems we will discuss, the distinction between compound nuclear and direct mechanisms is blurred. This is because a direct reaction may involve a significant fraction of the total number of nucleons. Conversely, the energy tied up in shell structure or alpha clustering in these light nuclei is not small compared with the kinetic energies characterizing compound nuclear formation. Not surprisingly, neither description is adequate.

The remainder of this section is a brief, general description of heavy ion cross sections over their entire energy range, along with definitions of quantities used to describe fusion in the Coulomb barrier region. Section

I.B describes the reaction sequence on a microscopic level and discusses details of the final states. We then conclude this chapter by examining a number of measurement schemes. While this approach may appear unnecessarily pedagogical, it will streamline the flow of argument in later sections where we will be concerned with more complex experimental details.

Simple geometrical arguments suffice to explain the obvious features of heavy ion fusion cross sections over most of their energy range. Large nuclei will coalesce when they approach each other to within a certain critical radius. As the collision energy increases. low impact parameters will begin fusing first and the cross section will increase until the maximum geometrical overlap is reached. Except in special cases of competing direct processes, the total reaction cross section up to this point is dominated by fusion. This behavior is seen most clearly in a graph of σ_{fus} *vs.* 1/E (fig. 1) Above this maximum, the fusion cross section falls as the increase in the centrifugal barrier begins to exclude higher partial waves from the nuclear interior. At the very highest energies one reaches the liquid drop or *yrast* limit for the compound nucleus and the cross section drops rapidly (Ca79, Di82), although this behavior has not been carefully explored.

At low energies, the cross section is dominated by penetration of the Coulomb barrier. Because charged particle cross sections fall many orders of magnitude for a decrease of a few MeV in interaction energy, one usually defines the S- factor as:

$$S(E) \equiv E\,\sigma(E)\,exp\,(2\pi\eta) \quad ; \qquad \text{I.A.1}$$

where

$$\eta \equiv Z_1 Z_2 e^2 / \hbar v_{rel} \quad .$$

This factors the s-wave Coulomb barrier penetrability energy dependence out of the cross sections. For point-like particles, the low energy S-factor should be approximately constant, but for heavy ions, the distance of closest approach at the Coulomb barrier is comparable to the nuclear radius. The next order correction to the s-wave penetrability defines the $\widetilde{S}$ -factor:

$$\widetilde{S}(E) = E\,\sigma(E)\exp(2\pi\eta + gE) \quad ; \qquad \text{I.A.2}$$

where, theoretically,

$$g = \frac{1}{3}(8\mu R^3 / Z_1 Z_2 e^2 \hbar^2)^{1/2} \quad .$$

μ is the reduced mass, and R is the rms charge radius.

The S-factor actually overcompensates for the energy dependence of the cross section. Where the cross section may fall 8 orders of magnitude over some energy interval below the Coulomb barrier, the S-factor will rise perhaps 2 orders of magnitude over the same interval. $\widetilde{S}(E)$ is relatively energy independent; however, it requires an assumption about the radius of the target and projectile. It is, therefore, seldom used.

B. Reaction Products

While direct reactions take place on a time scale of the order of the target-projectile transit time ($\sim 10^{-21}$ s), compound nuclear reactions are typically 1000 times slower. When nuclei in this mass region merge, the binding energy per nucleon goes up. The nearly equilibrated compound system is highly excited and cools itself primarily through emission of light particles during the first $\sim 10^{-18}$ s. When this becomes energetically impossible, the excited residual nuclei undergo complex γ-ray cascades until reaching their ground states ($\sim 10^{-15}$ to10^{-3} s). Finally, these nuclear ground states may be unstable with respect to β-decay ($\sim 10^{-3}$ to 10^{4} s).

Even in the lightest of these systems at low energies, the number of exit channels is enormous, very often amounting to thousands or tens of thousands of states. (The *smallest* number of final states actually measured in the lab, as of this writing, has been ~20 (Be78, Be81b)). Since one can think of the compound system as equilibrating to some temperature, the maximization of entropy requires a heavy ion collision to fill a volume of phase space consistent with the conservation laws with uniform probability. Thus, the distribution of products will be proportional to the density of final states.

The evaporation of a light particle from the compound nucleus would populate final states according to the density of states due to their relative motion, $\rho_T \propto (E_{c.m.} - Q + E^*)^{1/2}$, times the nuclear level density, $\rho_I(E^*)$, where E^* is the excitation energy in the residual nucleus. For large E^* the Fermi gas level density goes approximately as:

$$\rho_I(E^*) \propto \frac{\exp(2a[E^* - \Delta]^{1/2})}{(E^* - \Delta)^2} \quad , \qquad \text{I.B.1}$$

where Δ is a shell-dependent pairing correction. So for evaporation of a single particle, this distribution of nuclear final states is:

$$\rho(E^*) \propto (E_{c.m.} - Q + E^*)^{1/2} \frac{\exp(2a[E^* - \Delta]^{1/2})}{(E^* - \Delta)^2} \quad . \qquad \text{I.B.2}$$

A schematic plot of this function is given in fig. 2. Eqn. I.B.2 implies that the emission of a low energy light particle is much more likely than a high energy one, since there are many more internal states at high excitation. The result is that a narrow band of excited compound nuclear levels explodes into an extremely complicated distribution; in fact, it is as "complicated" as it can possibly get.

Every state in this distribution which lies above a particle emission threshold populates a similar distribution in the appropriate residual nucleus. It is necessary to add together their individual contributions to obtain the excited state spectrum in sequential emission. An example of this is also given in fig. 2. Because the evaporated particles are light and their energy is low, the laboratory angular distributions of the heavy particles are strongly peaked in the forward direction by kinematics ($\vartheta_{lab} < 20°$)), with a maximum around $\vartheta_{lab} \sim 6\text{-}10°$ (Ko79). In the center of mass system, of course, the maximum is at 0°. The angular distributions for secondary and tertiary evaporation are a little wider because of the cumulative random impulses of particle emission. (See example in fig. 3.)

It is not strictly true that all energetically possible states are populated with equal probability. Emission of very low energy charged particles is inhibited by their transmission coefficient through the Coulomb barrier. In systems for which dynamics constrains the average values of certain physical quantities, the entropy is not simply the logarithm of the

number of available states, but is instead a quantity called the "missing information," (Al80) defined for a distribution, $P(E)$, as

$$S = \ln N - P(E) \ln\{P(E)/P^{o}(E)\} \ , \qquad \text{I.B.3}$$

where N is the total number of available states and the distribution $P^{o}(E)$ is the statistical one. The mean value of the dynamic quantities are defined as

$$[A] = \int A(E) P(E) dE \ . \qquad \text{I.B.4}$$

In the case of heavy ions, dynamical constraints act to shape the nuclear excited state distribution and the partitioning into states of relative motion follows from this. The main constraints are the average value of the excitation energy, E^{*}, and the width of the exciton distribution, $(aE^{*})^{1/2}$, for each energetically possible residual nucleus (Al79). These are identified by finding the extremum of the Lagrangian:

$$L = -S + \lambda_{o}[1] + \sum_{\tau} \lambda_{\tau}[A_{\tau}] \ , \qquad \text{I.B.5}$$

where $[1] \equiv \sum_{\gamma} P_{\gamma}$ is the normalization condition. The distribution which maximizes this is (Ja57):

$$P_{\gamma}^{\max} = P_{\gamma}^{o} \exp[-\lambda_{o} \sum_{\tau} \lambda_{\tau} A_{\tau}(\gamma)] \ . \qquad \text{I.B.6}$$

From this we can see that the "surprisal," *i.e.*, the quantity $-\ln(P_{\gamma}/P_{\gamma}^{o})$,

is a linear function of the constraints. When the excited state population of a heavy ion reaction is measured directly (Al79), the surprisal is found to vary nearly linearly with energy (see fig. 4). The slight curvature is accounted for by a weak dependence on $(aE^*)^{1/2}$.

The emission of light particles results in about 2 to 7 different residual nuclear species, each possessing as much as 6 to 10 MeV of excitation energy. The gamma ray cascade that follows is extremely complicated. The matrix element for an E1 or M1 transition between two nuclear levels depends on their energy difference roughly as $(\Delta E)^3$. However, the density of states decreases exponentially with decreasing excitation, with the result that low energy, rather than high energy, transitions are favored. There is a significant probability, then, that the cascade will feed the relatively widely spaced lowest-lying levels. Because a γ transition reorients the nuclear spin, angular correlations and polarization effects tend to be washed out in multiple cascades, and the gamma rays are emitted nearly isotropically. The gamma cascade is discussed in more detail below.

Finally, it should be mentioned that, in this mass region, the valley of β-stability lies along the line $N = Z$. If the compound nucleus at any time evaporates a proton or neutron, this moves the residual nucleus off this line, where it may be $\beta^{\pm}$-unstable. Beta decays may provide a further (delayed) γ-cascade. These associated cascades are usually confined to the first few excited states, where half-lives and branching ratios are generally well-known.

C. Methods of Measurement

The first heavy ion measurements relied on the detection of the light evaporated particles (Al60, Al63, Al64). The accelerators of the time were only capable of delivering light ion beams ($^{10,11}B$, ^{12}C, ^{14}N, ^{16}O) at energies approaching the Coulomb barrier. The light particles from primary evaporation are the largest part of these reaction cross sections; therefore, the problem of double counting is minimal. The usual practice is to "range out" the elastically scattered heavy particles and evaporation residues with thin foils and measure the angular distributions of the light charged particles with surface barrier detectors. Neutrons are usually studied separately with long counters; however, the quality of their angular distribution data is invariably lower than that of charged particles.

The inherent limitation of this method is the problem of double counting. Most neutron binding energies are of the order of 5-7 MeV, so one cannot exceed this energy range before the onset of "secondary" emission. Additionally, single particle evaporation only dominates the cross section for very tightly bound nuclei (generally those with "good" alpha structure.) Thus, this technique has been limited to the study of specific exit channels of low excitation energy. The only total cross sections determined by this method have been $^{12}C+^{12}C$ and $^{16}O+^{16}O$.

In some cases it is possible to extract the fusion cross sections directly from the elastic scattering angular distributions. The total elastic scattering amplitude is the amplitude, f_{Coul}, and a nuclear compound-elastic amplitude, f',

$$f(\vartheta) = f_{Coul}(\vartheta) + f'(\vartheta) \quad . \qquad \text{I.C.1}$$

Following the derivation by Holdeman and Thaler (Ho65), we apply the optical theorem to the terms in eqn. I.C.1 . (We note that equation 16 of this reference contains two typographical errors. The formulae we present have been corrected.)

$$\sigma'^{tot} \equiv (\sigma^{tot} - \sigma_{Coul}{}^{tot}) = \frac{4\pi}{k} \mathrm{Im} f'(0) \quad . \qquad \text{I.C.2}$$

Relating σ'^{tot} to the total reaction cross section, $\sigma_R{}^{tot}$,

$$\sigma'^{tot} = \sigma_R{}^{tot} + \sigma'_{el}{}^{tot} = \sigma_R{}^{tot} + \int [\sigma_{el}(\vartheta) - \sigma_{Coul}(\vartheta)] d\Omega \quad . \qquad \text{I.C.3}$$

Although this integral is the difference of two divergent terms, we know the result is finite since the nuclear forces involved have a finite range. Therefore, we may cut off the integral at a small angle, $\vartheta_0 \sim 1/l_{grazing}$, and estimate the residue from the Coulomb amplitude, which is completely known. The result is:

$$\sigma_R{}^{tot} = 2\pi \int_{\vartheta_0}^{\pi} [(d\sigma/d\Omega)_{Coul} - (d\sigma/d\Omega)_{el}] \sin(\vartheta) d\vartheta$$

$$-4\pi |f'(0)|^2 \sin^2(\vartheta_0/2)$$

$$+ 4\pi\lambda \, \mathrm{Im}\{f'(0)\exp[2i\eta \ln\sin(\vartheta_0/2) - 2i\sigma_o]\} \quad , \qquad \text{I.C.4}$$

where $(d\sigma/d\Omega)_{Coul}$ is the Rutherford differential elastic cross section, $(d\sigma/d\Omega)_{el}$ is the experimental differential elastic cross section, η, is the Sommerfeld parameter, and σ_o is the Coulomb scattering phase shift for $l = 0$. The finite range nuclear amplitude for elastic scattering at 0°,

$f'(0)$, may be determined from elastic scattering data taken at angles smaller than ϑ_0 (Ho65).

In practice, one observes that $(d\sigma/d\Omega)_{el}$ approaches $(d\sigma/d\Omega)_{Coul}$ to within experimental errors as $\vartheta_0 \rightarrow 0°$ (Wo76). This suggests that we may drop the last two terms on the right side of eqn. I.C.4 and write, approximately,

$$\sigma_R \sim 2\pi \int_{\vartheta_0}^{\pi} [\, (d\sigma/d\Omega)_{Coul} - (d\sigma/d\Omega)_{el} \,] \sin(\vartheta)\, d\vartheta \quad . \qquad \text{I.C.5}$$

The "sum-of-differences" method, as this is called, has only been tested in a few systems, with inconclusive results. Wojciechowski *et al.* (Wo76b) obtained good agreement ($\sim$ 10%) for α-particle elastic scattering from ^{197}Au, ^{206,207}Pb, and ^{209}Bi at 24 MeV. However, in heavy ion systems, eqn. I.C.5 is often much larger than measurements. The cross sections for ^{63,65}Cu(^{16}O,X) given by eqn. I.C.5, for example, are typically 50-100% greater than the data.

A recent determination of the low energy ^{12}C+^{12}C reaction cross section seems to show a similar discrepancy with previous measurements (Tr80). For identical particles, eqn I.C.5 must be modified to:

$$\sigma_R \sim 2\pi \int_{\vartheta_0}^{\pi/2} [\, (d\sigma/d\Omega)_{Mott} - (d\sigma/d\Omega)_{el} \,] \sin(\vartheta)\, d\vartheta \quad , \qquad \text{I.C.6}$$

where ϑ is the center of mass angle and $(d\sigma/d\Omega)_{Mott}$ is the Mott differential elastic scattering cross section. At the lowest experimental energies, the grazing angular momentum corresponds to a lower limit of

integration, $\vartheta_0 \sim 5°$. This is well beyond the range of most experiments; nevertheless, when the data cover a sufficiently large fraction of the integral, one has reasonable grounds to extrapolate to smaller angles with a model calculation.

There is a practical difficulty with this. The nucleus presents a "sharp" surface to de Broglie wavelengths which are shorter than the surface diffuseness, a. When this wavelength is comparable to the diffuseness, as in sub-barrier heavy ion fusion, diffraction effects of wavelengths greater than about $1/4l_{grazing}$ will occur near the edge of the nuclear shadow ($\sim 1/l_{grazing}$). Thus, the model calculation will fluctuate about the Mott cross section at small angles. An example of this "ringing" is given in fig. 5 for the ratio of an optimized Optical Model calculation to Mott scattering for $^{13}C+^{13}C$ at $E_{c.m.} = 7$ MeV.

These fluctuations turn out to have a sizable effect on the integral I.C.6. If we think of σ_R as being the sum of "individual fluctuations," then as we decrease ϑ from $\pi/2$, successive contributions will be of opposite sign and decreasing area. In the range $\vartheta_0 < \vartheta < \pi/2$, this sign change enhances the importance of each fluctuation on the value of the integral. For $\vartheta < \vartheta_0$, however, successive terms are small and nearly equal, so the sum will oscillate rapidly about the true value of the integral.

At first sight, then, it appears that I.C.6 may be safely evaluated as long as $\vartheta_0 \ll 1/l_{grazing}$. It must be remembered, however, that the model cross sections are derived from a decomposition of the scattering amplitudes into partial waves. This series is truncated at some maximum angular momentum in order to evaluate it numerically. If, say, $l_{max} \sim 2l_{grazing}$, then the truncated series cannot meaningfully support any scattering structure subtending an angular interval smaller than about $1/l_{max}$.

Thus, we cannot expect our model to accurately describe diffraction fluctuations within $\sim 1/2l_{grazing}$ (2°) of ϑ_0. The error in σ_R should be the same order of magnitude as the total fluctuation of the sum in this region.

It should be noted, however, that the value of the small angle cutoff, ϑ_0, used in the study of Treu *et al.* was chosen as the third Mott scattering minimum (~40°). This is much larger than the angle corresponding to $1/l_{grazing}$ (~10°) and introduces a serious error into the integral. Re-evaluating integral I.C.5 at $E_{c.m.}$ = 6, 8, and 10 MeV with a 10° cutoff (using the potential parameters quoted in ref. (Tr80) gives correction of +100%, -25%, and -1%, respectively. This method, then, places fairly stringent requirements on the accuracy and completeness of the angular distribution data.

At higher energies the residual nuclei can be identified via $E-\Delta E$ telescopes.This method becomes unreliable, however, as one approaches the Coulomb barrier from above, because the changing dE/dx makes separation of elements by charge more and more difficult. Energy loss in the ΔE detector soon becomes too large a fraction of the total energy, and the products cannot be resolved from the tail of the rising background of elastically scattered particles. The only viable alternative, therefore, lies in the measurement of the γ-rays. Two methods for doing this have been devised.

The first method, developed at Caltech and employed primarily by the group at Laval University, is to essentially build a calorimeter out of NaI (Cu76). Two large NaI crystals are placed close together on opposite sides of the target. In this geometry they subtend a solid angle of almost 4π steradians. Most of the γ-rays from a cascade are of low energy, so

when the detectors are operated in coincidence, the chances of two or more γ's from a single cascade to sum is essentially unity. Thus, the probability of detecting a cascade is relatively independent of the number of steps therein. The production of positron emitters can be a problem; however, their annihilation radiation can usually be isolated and subtracted. The disadvantage of this method is that it is unable to distinguish γ-rays due to reactions on target impurities. We discuss a specific example of this in connection with our measurement of $^{13}C+^{13}C$. Its advantage is high efficiency.

The second method of gamma detection is to observe the low-lying transitions of the evaporation residue cascades. These transitions are typically in the 500-2000 keV range, where the Ge(Li) full energy peak efficiency is relatively large. The Ge(Li) spectrum one would expect, then, is a smooth background of unresolved, summed x-rays and soft γ's, punctuated by a few distinct peaks.

With energy resolution of the order of a few keV it is usually possible to avoid the problem of target contamination; however, three remarks are in order here. Firstly, it often happens that the target is contaminated by a substance (such as a different isotope) whose products are similar to those under study. Secondly, the lifetime of a γ cascade is so short that, even in solid targets, the evaporation residues may not come to rest fast enough to prevent doppler-effect distortion of the photopeak shapes. One must take care in separating closely spaced peaks. Finally, secondary reactions from materials in the shielding, target holder, and detector material itself may give spurious peaks unless a careful study of their origin can positively exclude them from the data.

An obvious advantage of this method over NaI is that production yields of several residual nuclear species are identified by their characteristic γ transitions. Reconstructing these yields from the data requires: a) knowledge of the level structure and branching ratios up to modest excitation energies ($\sim$10 MeV), and b) model-dependent calculations of the expected excited state populations as a function of excitation of the compound system. The next chapter will illustrate some details of these points in a discussion of the $^{13}C+^{13}C$ data analysis.

II. $^{13}C+^{13}C$ Measurements

A. Introduction

Low energy heavy ion fusion cross sections have been studied especially carefully ever since the discovery of resonances in α-conjugate systems such as $^{12}C+^{12}C$ (Al60, Al63, Al64) and $^{12}C+^{16}O$ (Pa71). More recently, both direct and indirect evidence for resonant behavior has been found in such non-α-conjugate pairs as $^{14}C+^{14}C$ (Ko81, Dr81) and $^{12}C+^{16}O$ (We76, Be81a). This suggests that the phenomenon relies partly on the formation of unusual doorway states and partly on the small number of available final states compared to systems differing even by the addition of a single nucleon.

Even ignoring the difficulty of resonances, the impetus for low energy measurements is the disturbing inconsistencies in our picture of reactions between pairs in the mass range $9 \leq A \leq 20$. No consistent, reasonable model has been proposed for low energy fusion cross sections which is appropriate for more than a few of these systems (St80). Part of the problem lies in the inconsistency of the data. For example, in even so well-measured a system as $^{16}O+^{16}O$, individual data sets still disagree, by factors of two, on the cross section at the Coulomb barrier (Hu80). To shed light on the more interesting physics of resonances, the minimum we would require is a general model of fusion and elastic scattering whose parameters can be varied predictably from one system to another. This program must be founded on accurate measurements between many reaction pairs.

One sensible strategy is to record differences between nearly similar systems. The most dramatic resonance structure, for example, occurs in

$^{12}C+^{12}C$; yet the closest nearby system, $^{12}C+^{13}C$, has none. Further comparisons must be made to clarify the obviously drastic effect of the extra neutron. We have chosen, then, to measure the system $^{13}C+^{13}C$, to explore further the role of neutron number in carbon isotope fusion.

The data given in this chapter are the partial cross sections for six exit channels, plus the inferred total fusion cross section, for energies in the range $3.26 \leq E_{c.m.} \leq 8.0$ MeV. Elastic scattering differential cross sections were determined at 4 angles over the energy interval $4.5 \leq E_{c.m.} \leq 8.5$ MeV, as well as angular distributions at $E_{c.m.} = 7.0$ and 8.0 MeV. The total fusion cross section and ^{24}Mg production are compared with the previous measurements by Chatterjee *et al.* (Ch80) and those of Dasmahapatra *et al.* (Cu81, Da82). The elastic scattering data of Korotky *et al.* (Er80, Ko81), as well as those of Helb *et al.* (He73), overlap the present data only for their lowest energy points; however, we have made quantitative comparisons where possible. Finally, we report no evidence for resonances in any of the cross sections, down to a level of ±10%.

B. Fusion Cross Sections

1. Apparatus

The apparatus and data reduction used in this experiment have been described previously (Da76a, Da76b, Sw76, Ch77a, Wu78). We will not repeat these, but will enlarge only on relevant details.

The beam was delivered as $^{13}C^{2+}$ or $^{13}C^{3+}$ by the ONR-Caltech EN tandem accelerator and directed onto thin ($< 20\ \mu g/cm^2$) natural carbon or ^{13}C- enriched targets, which formed the end of a deep Faraday cup. (see fig. 6.) The target/Faraday cup assembly was biased to +300 Volts to

minimize the loss of secondary electrons. By applying several values of bias from -300 to +1000 Volts, we established that our charge collection was accurate to better than ± 5%. The data were normalized to the integrated beam.

At the lowest energies the beam current was typically 300 nA; each data point represents an integrated charge of 900 μC of $^{13}C^{2+}$. Data were taken using two isotopically enriched targets. The beam energy was varied in 100 keV steps from 7.0 to 12.6 MeV, and in 200 keV steps from 6.0 to 7.0 MeV and 12.6 to 16.0 MeV on the first target. To improve our statistical accuracy, the entire excitation function was redetermined in 200 keV steps from 6.4 to 7.0 MeV and in 1 MeV steps from 7.0 to 16.0 MeV with a second target. High energy points were run with a current of about 40 nA, and a collected charge of 60 μC of $^{13}C^{3+}$. Dead time was monitored, and amounted to a 12% correction at the highest energies, although it was negligible in most runs. For orientation, the energy loss of an 8 MeV ^{13}C ion in the carbon layer of our targets was about 150 keV.

Some experimentation was necessary to consistently obtain ^{13}C beams of sufficient intensity for low energy fusion and high energy elastic scattering. We introduced ^{13}C-enriched methane gas (99.34 mole % ^{13}C, Mound Laboratory, Monsanto Research Corp.), diluted with hydrogen, as a source gas in the negative ion duoplasmatron. The optimum mixture of ^{13}C methane to hydrogen was about 1:3 (pressure). This was first dried through an acetone/dry ice cold trap to prevent water vapor contamination of the ion source. Stability and cleanliness were improved enormously by running a proton beam for about 30 minutes prior to the day's experiment. Care was also taken to prevent contamination by oxygen or hydrocarbon vapors during mixing with hydrogen. These steps are

essential for producing a negative ion source beam, in that these impurities entering the ionization cavity would make it impossible to separate the $^{13}C^-$ or $^{13}CH_3^-$ beams from the much more easily produced $^{12}CH^-$ and $^{16}O^-$. (We usually identified $^{13}C^-$ by setting the extraction voltage and varying the bending magnet current. The $^{13}C^-$ is accompanied by a $^{12}C^-$ beam about 10% as intense and at a slightly lower magnet current setting.) Under optimum conditions it was possible to extract $\sim 1\ \mu A$ of $^{13}C^-$ using hydrogen as the charge exchange gas. Using lithium vapor as the exchange gas gave much higher source currents, $\sim 3-5\ \mu A$ of $^{13}C^-$. By running a high stripper gas pressure, we were able to consistently run $\sim$200 nA of $^{13}C^{2+}$ (E = 7 MeV) on target in the South 20° beamline. Maximum beam current fell with increasing energy. Above about 8.2 MeV, $^{13}C^{3+}$ becomes the dominant charge species. At optimum focus, we measured $\sim$150 nA of $^{13}C^{3+}$ (E = 8 MeV) to $\sim$50 nA (E = 16 MeV) at the target.

2. Targets

Two targets were prepared from 90% ^{13}C-enriched elemental carbon powder (Mound Laboratory, Monsanto Research Corp.). This was pressed into pellets and slowly outgassed to white-heat *in vacuo* for about 15 minutes prior to electron beam evaporation onto 99.99% spectroscopically pure copper blanks. These blanks were 1" discs punched from 0.01" sheet metal. After evaporation, the ^{13}C target enrichment was measured to be 80-85% (see below). A ^{12}C target was made by electron beam evaporation of reactor grade graphite onto an identical copper blank.

The target chamber was isolated from the beam line vacuum by a 30 cm long (1 cm i.d.) liquid nitrogen cold trap. The target, itself, was kept under ultra-high vacuum, and during runs the pressure was usually less

than 2×10^{-8} torr. To check for carbon buildup, a copper blank was placed in the target chamber and heated for 6 hours with a proton beam which was adjusted to have the same wattage as attained with the ^{13}C beams. Using the reaction $^{12}C(^{12}C,\alpha)^{20}Ne^{*}(1634\ keV)$, $\sigma(E_{c.m.}=7.5\ MeV) \sim 100$ mb, we found less than 0.1 $\mu g/cm^2$ carbon deposited. This is a correction of less than 0.5% to our cross sections.

Total target thickness was determined, first, *in situ*, by profiling the small hydrogen contamination of the carbon layers as a function of depth (Sw75). The profiling reaction was a narrow resonance in $^{1}H(^{19}F,\alpha\gamma)^{16}O$ at $E_{^{19}F}=6.4$ MeV. This is possible even for such thin targets because the stopping power for heavy ions in solids is enormous. Some latitude exists in interpreting the thickness from these data because of adsorbed water and/or hydrocarbon layers on the front and back surfaces of the target. After unfolding this uncertainty, and the width of the resonance (47 keV), the energy loss of ^{19}F ions in ^{13}C was converted into target thickness using the stopping power tables of Northcliffe and Schilling (No70). For our two targets, these values are: $19.1\pm1.7\ \mu g/cm^2$ and $18.8\pm1.7\ \mu g/cm^2$, respectively.

Both target thickness and isotopic composition were later determined more accurately by using a combination of Rutherford α-scattering and resonant proton scattering at 160° in the reactions $^{12}C(p,p)$ at E_p = 1.73 MeV and $^{13}C(p,p)$ at E_p = 1.46 MeV (Mi54, Aj76). First, the total thickness of each target was determined by α-scattering. Next, a known thickness of ^{12}C was used in conjunction with the $^{12}C(p,p)$ resonance to establish the count rate per incident proton in a detector at 160°. The ^{12}C content of the isotopically enriched ^{13}C targets was found by comparison with this count rate. The maximum count rate per incident

proton was located empirically to within 3 keV by varying the incoming proton energy in 5 keV steps. The thicknesses of all the targets were comparable, and the proton energy loss was about 3-4 keV. At the resonance, the proton count rate is about 35 times larger for ^{12}C than for an equal thickness of ^{13}C.

The ^{13}C content was measured independently with the proton resonance at 1.46 MeV by comparison with a self-supporting ^{13}C foil standardized previously by α-backscattering. Here, however, the effective ratio of the ^{13}C-to-^{12}C cross sections is only about a factor of 5 at the resonance energy. The thicknesses inferred for the two ^{13}C targets by this procedure were (14.11 ± 0.42) $\mu g/cm^2$ ^{13}C + (3.16 ± 0.10) $\mu g/cm^2$ ^{12}C and (16.58 ± 0.49) $\mu g/cm^2$ ^{13}C + (3.15 ± 0.10) $\mu g/cm^2$ ^{12}C. These values agree well with measurements by the hydrogen profiling technique.

3. Gamma Measurements

The Q-value diagram for $^{13}C+^{13}C$ is given in fig. 7. Gamma ray yields from low-lying transitions in the evaporation residues were observed with an 80 cm^3 Ge(Li) detector located at 0° with respect to the beam, as close as possible to the target. The front face of the Ge(Li) *crystal* was 12 mm from the target, including 1.7 mm of lead for preferential absorption of soft γ-rays, 1.5 mm of aluminum in the crystal housing, 0.51 mm of stainless steel (vacuum chamber), 3.0 mm of quartz (electrical insulation), and 1.0 mm of copper from the target backing and heat sink. The detector was heavily shielded from room background by at least 10 cm of lead in every direction except upstream. From our check on carbon buildup and previous experiments, we found the detector is not sensitive to beam-scraping on the 5/32" tantalum aperture located 40 cm upstream

from the target. Gamma transitions observed in this geometry are indicated in the typical spectra for both ^{12}C and ^{13}C -enriched targets (see fig. 8).

Note that since the valence neutron of ^{13}C is so loosely bound, background from the capture or inelastic scattering of neutrons on nearby materials (especially on the isotopes of germanium and lead) had to be checked to ensure no overlap with peaks of interest. Levels with short lifetimes (< 1 ps) were doppler-shifted because they did not have time to come to rest before decaying; this accounts for the high energy tail on some peaks. For the energies relevant in this experiment, typical shifts are on the order of 3% or, say 30 keV. A few spectra were taken at 90° to the target, where this distortion is minimal, to aid in identifying background peaks. At a few selected points, spectra were extended to $E_\gamma = 12$ MeV. We shall refer to these in our discussion of target impurities and competing reactions.

A constant consideration in this experiment was to limit neutron damage to the Ge(Li) crystal structure, and the attendant loss of resolution. We monitored the neutron flux by regular measurement of the Ge(Li) resolution and by neutron dosimeters which were standardized by a known flux. The most accurate method, however, was to use the Ge(Li) detector, itself, as a neutron detector by monitoring the number of counts in the pulse-height spectrum at 691 keV. This line comes from the reaction $^{72}Ge(n,n')$. Inelastic neutron scattering cross sections typically rise abruptly from a threshold (691 keV) and quickly level off to a constant value, in this case ~0.2–0.3 barns (Ch70). We can utilize the fact that this is a $0^+ \rightarrow 0^+$ transition of less than 1 MeV and, therefore, goes by internal conversion. The efficiency of detecting a conversion electron

produced within the crystal itself is essentially 1. Very few high-lying states in ^{72}Ge have a significant branching ratio to this level, therefore, inelastic scattering to higher states will not affect the yield of 691 keV γ-rays. We can rule out contributions from neutron capture gamma rays because ^{71}Ge is unstable. Assuming an exponential form for the neutron spectrum gives the rule of thumb that for each count in the peak at 691 keV, approximately 200 neutrons have passed through the detector. Since a Ge(Li) will begin to show some neutron-induced damage at a dosage of about 10^7, we were careful to minimize our running time in order to limit the neutron flux from this experiment to around 10^6.

The reaction channels observed with the Ge(Li) detector were the following: n + ^{25}Mg (E_γ = 390, 585 keV), n + n + ^{24}Mg (1369 keV), α + ^{22}Ne (1274 keV), α + n + ^{21}Ne (351 keV) and p + n + ^{24}Na (472 keV). For beam energies above 12 MeV, the channel α + α + ^{16}O (1982 keV) was also measurable. One reaction product, ^{24}Na, is β-unstable; it decays to ^{24}Mg with a half-life of 15.02 hours. Essentially every decay of ^{24}Na feeds the 1369 keV transition in the daughter nucleus. For several energy points (approximately every 1 MeV in bombarding energy) the beam was stopped and the delayed activity was monitored, and then subtracted from the gamma yield of the 2n channel. (A sample Ge(Li) spectrum of the delayed activity is given in fig. 9.) In addition, when any channel involved the evaporation of a neutron plus another particle, a correction was made for the yield from the ^{12}C content of the target. We did not attempt to remeasure the ^{12}C+^{13}C cross section because that reaction had been previously determined by another group using the same apparatus and analysis (Da76). The yields from this reaction vary smoothly enough that we felt justified in interpolating this correction from widely-spaced

measurements.

4. Detector Efficiency

The data were stored as 4096 channel spectra, adjusted for an approximate energy calibration of 1 keV per channel. Peak areas were extracted on the ND4420 MCA (Nuclear Data) by assuming a linear background and averaging background over small intervals on either side of the peak, then corrected for dead time, ^{12}C contribution or delayed activity. These raw yields were then normalized to the integrated charge. The production cross section of a particular residue, σ, is related to the γ yields, y, by

$$\sigma = \frac{y}{n_i n_t \varepsilon \beta} \quad , \qquad \text{II.B.1}$$

where n_i is the incident flux, n_t is the ^{13}C target thickness, ε is the Ge(Li) full energy peak (photopeak) efficiency, and β is the summing-branching correction factor. Both ε and β depend on the transition energy and dynamics of the parent cascade. The quantity, "$\varepsilon\beta$," then, is the probability that a nucleus in a given distribution of excited states will produce a count in the full energy peak of a specific low-lying transition, in our experiment geometry. Obviously, β is also dependent on beam energy.

Absolute photopeak efficiencies for transition energies in the range $250 < E_\gamma < 3300$ KeV were found using standard calibration sources and known branching ratios. Data concerning these sources and other input data are listed in Appendix A. To determine the detector efficiency to better than ±5%, a number of effects were considered.

When the detector is so close to the target, small changes in geometry may effect the reproducibility. Beam spot travel was not monitored during the experiment; however, the maximum excursion allowed by the defining slits, cold trap channel, and tantalum collimator was ±1 cm. Visual detection of light target deterioration (slight discoloration) after several hours of use revealed that the actual wandering was considerably less, in fact, comparable to the beam spot size (~0.5 cm). This was verified by installing a beam viewer at the target position and studying the effects of various accelerator controls on the beam spot after optimizing the current. Because the crystal face is large (4.85 cm dia.), this was a negligible correction to the detector efficiency.

The photopeak efficiency is extremely sensitive to small changes in the distance to the target or source. Investigations with ^{60}Co ($E_\gamma = 1172$ keV) demonstrated that at such close distances, a shift of 1 mm resulted in a 10% change in efficiency. This systematic error would be averaged over several measurements and sources in the detector calibration, but would be present if the shift occurred during a run. The detector, therefore, was not moved, except to change targets. Generally, an entire excitation function was taken before disturbing the setup. When this was not possible, data were taken at several overlapping energies to provide a normalization and check for consistency. The only notable change in geometry during the experiment was in the small amount of low energy data (6.6 to 10 MeV) taken without the 1.7 mm lead absorber, to improve the counting rate.

The absolute efficiency curve was determined for the geometry and set of absorbers corresponding to a complete set of data from a single target (fig. 10). The efficiency curve of the data taken with the other

target was approximated with sufficient accuracy by normalizing the fusion photopeak yields at several overlapping energies. This ratio was 1.16±0.06 . Similarly, efficiencies with and without a lead absorber were found by comparison of two data sets taken at the same energy (ratio equals 1.12 ±0.06). The detection efficiencies of the two targets were not identical because a double thickness of copper backing was used as a heat sink for the high-current, low energy runs on one target.

5. Data Analysis

Because of the importance of 3-body final states (which have a higher ground state branching ratio than 2-body decays), we have performed a Hauser-Feshbach statistical model calculation to predict the excited state distributions for each exit channel; we used the computer code HAUSER*4 (Ma75). This code has been used extensively, explored in detail, and compared with alternative calculations (see, for example, Christensen *et al.* (Ch77a) or Olmer *et al.* (Ol74)). As there is quite a large body of data involved, the technical details are gathered, with a brief summary of Hauser-Feshbach theory, in Appendix B.

Once a good estimate of the excited state populations was made, we computed the interaction of the gamma cascade with the detector. To give an elementary example; assume an evaporation residue with two excited states, $E_2 > E_1$. If our Hauser-Feshbach calculation predicted relative populations, P_i ($\sum P_i = 1$), then the number of counts in the photopeak at E_1 would be given by

$$y_1 = N\varepsilon(E_1)P_1 + NP_2 b(E_2,E_1)\varepsilon(E_1)\{1 - t(E_2-E_1)b(E_2,E_1)\}, \quad \text{II.B.2}$$

where N is the production yield of a particular evaporation residue, $\varepsilon(E_1)$ is the absolute photopeak efficiency for a gamma ray of energy, E_1, $b(E_2,E_1)$ is the gamma branching ratio of level 2 to level 1, and $t(E_2-E_1)$ is the total detection efficiency of a gamma ray of energy, E_2-E_1. This last quantity is the probability that the concurrently produced gamma ray of energy E_2-E_1 will reach the detector and deposit *any* energy. This may be readily computed, given the geometry of the local absorbers and their attenuation coefficients:

$$t(E) = \int d\Omega \{ 1 - exp[-\mu(E) l(\vartheta,\varphi)] \} \exp[-\mu'(E) l'(\vartheta,\varphi)] \quad , \qquad \text{II.B.3}$$

where μ is the attenuation coefficient of germanium and $l(\vartheta,\varphi)$ is the path length through the active volume of the crystal; μ' and l' take into account the attenuation through materials between the target and detector (Pb, Cu, SiO_2, Al), and the "dead" layer on the Ge(Li) crystal surface. The summing effect is, at most, ~10%; this has been verified by measurements in cascades from calibrated sources (*e.g.*, ^{133}Ba and ^{22}Na). Therefore, we can confidently neglect Compton scattering by the shielding as a few percent error in this correction factor.

With the definitions:

$$\beta_1 \equiv P_1 + P_2 b(E_2,E_1) \{ 1 - t(E_2-E_1) b(E_2,E_1) \} \qquad \text{II.B.4a}$$

and

$$N \equiv n_i n_t \sigma \quad , \qquad \text{II.B.4b}$$

eqn. II.B.2 can be put into the same form as eqn. II.B.1. Of course the

realistic summing-branching factors are much more complicated, being the sum over a large number of levels. We have used the experimentally established spins, parities, and branching ratios wherever possible. These are generally available up to excitation energies of 10 MeV or so; we typically included the lowest 20 discrete states. Beyond this we must rely on level density formulae whose parameters were fitted to each residual nucleus for optimum accuracy. The calculated summing-branching ratios for the observed transitions are plotted in fig. 11. The accuracy is difficult to assess, but has been estimated to be ~10% (Wu78).

Finally, a correction must be applied to the beam energy to find the effective energy of the projectile. Because the cross section falls so rapidly with energy, the beam interacts preferentially with the front of the target. The effective energy is slightly higher than the energy in the center of the target. A suitable expression for E_{eff} is:

$$E_{eff} = \frac{\int_{E}^{E-\Delta E} \sigma(E) E \, dE}{\int_{E}^{E-\Delta E} \sigma(E) \, dE} \quad , \qquad \text{II.B.5}$$

where ΔE is the target thickness. Using $\sigma \sim E^{-1} exp\,(2\pi\eta)$ gives an analytic form for eqn. II.B.5 involving Exponential Integral functions. A numerical approximation of this effect gives a difference of only 6 keV from the energy at the center of the target for the lowest energy point, $E_{c.m.}$ = 3.262 MeV. This is less than the uncertainty in energy loss (~ 8 keV) and is negligible. But this correction is increasingly important at lower energies and has sometimes unjustifiably been omitted from the data taken on other systems. We will return to this point in our discussion.

6. Results

Partial and total fusion cross sections for each observed channel are listed in Table 1. The errors on these numbers represent counting statistics alone. The numbers in Table 1 are plotted in figs. 12, 13, and 14. The yield of ^{25}Mg is the average of two measurements. A comparison of the cross sections inferred by the yields in the 390 keV peak and the 585 keV peak is a check on the consistency of our data analysis. Fig. 15 plots the ratio $\sigma_{390}/\sigma_{585}$ as a function of energy. The cross sections agree to within 25%; certainly within the accuracy claimed for the Hauser-Feshbach calculation and statistical fluctuations.

Gamma rays from the ^{25}Na + p channel were not observed. One would expect ^{25}Na production to be low, since the ^{25}Mg yield is only a few percent of the total cross section. Proton and neutron evaporation are somewhat similar in that the spin and energy structure of the ^{25}Na and ^{25}Mg levels are comparable. With roughly the same Q-value, a naive guess is that the proton channel should therefore be suppressed by the effect of the Coulomb barrier on the transmission coefficients. Q-value considerations argue for even further proton suppression.

The ^{24}Mg + 2n channel comprises about 40-60% of the total cross section. Neutron channels dominate, as expected, with single particle and α channels one or two orders of magnitude smaller. The summing and branching correction for ^{24}Mg (fig. 11) is fairly constant, and insensitive to changes in the excited state distribution. This is evidence that the model dependence of the data reduction induces little distortion of the ^{24}Mg excitation function and, hence, the total cross section. The systematic uncertainty in the total cross sections is roughly the same in each channel and over the entire energy range. The systematic error is

derived from uncertainties of ±10% in the summing-branching factors, ±4% in target thickness, ±5% in beam integration and ±4% in Ge(Li) efficiency. The sum (in quadrature) of these errors is about ±15%.

C. Elastic Scattering Measurements

1. Apparatus

To supplement the fusion work, $^{13}C+^{13}C$ elastic scattering data were taken for an overlapping energy range. Incident $^{13}C^{3+}$ were scattered from self-supporting target foils into a pair of silicon surface-barrier detectors placed symmetrically about the beam direction. This arrangement allowed us to monitor changes in the beam spot position by checking for asymmetries in the counting ratio. The detectors were masked by circular tantalum apertures, each subtending a lab angle of 0.6°, with a solid angle of $\sim 1\times10^{-4}$ steradians. The maximum excursion of the beam allowed by the defining slits, after careful adjustment to minimize slit scattering, was ±0.2° in the lab.

The surface-barrier detectors used (ORTEC, model no. BA-017-050-100) were specially fabricated from low resistivity silicon (650 Ω-cm). Their small defect and excellent resolution were ideal for heavy ion work. Their rated resolution for 5.486 MeV alphas is 13.5 keV FWHM. Typical resolutions we encountered were 150 keV for $E(^{13}C) = 7.5$ MeV. The limitations in this experiment were always due to kinematics or straggling rather than detector resolution.

2. Targets

Self-supporting ^{13}C foils were prepared, as in the fusion work, by electron beam evaporation onto glass slides, followed by flotation onto tantalum holders. Our first attempts were heavily contaminated by the $BaCl_2$ used to separate the carbon film from the slide. Although we never produced foils as clean as those available commercially, we reduced this contamination to tolerable levels by flotation in a warm, 50-50 mixture of acetone and water.

A standard practice in low energy elastic scattering is to normalize the data to Rutherford scattering from a thin layer of some high Z material, such as gold, evaporated onto the target. We found gold was sputtered away too rapidly from either side of our foils under ^{13}C bombardment. (We believe the mechanism to be sputtering, rather than evaporation, because the gold loss was roughly proportional to dosage, not current.) This sputtering was effectively suppressed by constructing a sandwich consisting of about 15 $\mu g/cm^2$ of enriched carbon on either side of a 1.5 $\mu g/cm^2$ layer of gold. These targets were very stable and no noticeable deterioration occurred under the 100 nA $^{13}C^{3+}$ beams of this experiment. The ^{12}C foils were obtained commercially and floated onto identical holders. Hydrocarbon buildup was minimized by a liquid nitrogen cold trap located about 5 cm beneath the targets.

3. Excitation Functions

Differential elastic scattering excitation functions were taken at $\vartheta_{c.m.}$ = 60°, 70°, 80°, and 90°. The beam energy was varied in 250 keV steps from 9 MeV to 14 MeV, and in 500 keV steps from 14 MeV to 17 MeV. To minimize deterioration or carbon buildup effects, several targets were

used. Their thicknesses and composition were checked by α-scattering before and after each set of measurements. These targets were thicker than those in the fusion work, they ranged from 24 to 32 $\mu g/cm^2$ of ^{13}C + 6 to 8 $\mu g/cm^2$ of ^{12}C + 1.5 to 2.0 $\mu g/cm^2$ of *Au*.

Pulses from both detectors were stored on magnetic tapes as 512 channel spectra. Typical particle spectra at three different angles for ^{13}C incident on our enriched targets are given in fig. 16, and for commercial ^{12}C foils in fig. 17. For ^{13}C scattering on ^{12}C, the particle spectrum at a given angle consists of two peaks which are closely spaced in energy. The low energy one arises from ^{13}C scattering, while the higher energy peak comes from the ^{12}C recoils. This recoil peak overlaps the $^{13}C+^{13}C$ elastic peak, making it necessary to subtract off this contribution. For each energy and angle, the ratio of the $^{13}C+^{12}C$ scattering-to-recoil peaks was measured with a ^{12}C target. Next, the enriched target spectrum was taken, and the ^{12}C contribution to the elastic scattering peak was inferred and subtracted. A further small correction was calculated from the oxygen peak and subtracted. The ^{13}C yield was then normalized to the *Au* peak. Because the energy dependence of Rutherford scattering is $1/E^2$, the ratio of the $^{13}C+^{13}C$ elastic scattering to the Mott cross section is found by multiplying the data by E^2/σ_{Mott}, and normalizing to unity at low energies.

The results are plotted in fig. 18 and listed in Table 2. The quoted errors arise solely from the propagation of statistical uncertainties; we presume systematic errors to have been avoided. A number of systematic errors would be averaged out by experimental design. Small fluctuations in the beam spot location, carbon buildup, oxygen contamination, peak extraction and dead-time errors would be second order effects in the

cross sections. This method also relaxes the need for precise measurements of target thickness, beam current, detector solid angle and scattering angle. All of these are effects of second order or less. Nonetheless, several low energy points were repeated to check reproducibility. They agree to within statistical errors.

4. Angular Distributions

Elastic scattering angular distributions were also examined at E_{lab} = 14.0 and 16.0 MeV. We took advantage of the symmetry in non-relativistic identical particle scattering of the center-of-mass angular distributions about 90°. At back angles, the inevitable background from hydrogen and heavy metals is much lower. The two peaks are more easily separated, except at low energies and for angles greater than about 70° (due to straggling in the target). As the detectors are moved to greater and greater angles, straggling rapidly worsens. To postpone this, both detectors were placed on the same side of the beam, with one detector fixed at $\vartheta_{lab} = 30°$ to monitor current and target thickness. The angular setting of the other detector was varied in 0.5° to 2° intervals from $\vartheta_{lab} = 40°$ to 76°, with the more closely spaced measurements needed to define the minimum at $\vartheta_{lab} = 45°$. The orientation of the target to the beam was varied to minimize the path length (and the straggling) of the *scattered* ^{13}C, since the straggling of the higher energy *beam* was much less. The angular scale was calibrated to an accuracy of about ±0.3° (lab) by the location of the Mott cross section minimum at $\vartheta_{lab} = 45°$.

The (relative) product of incoming flux times target thickness was given by the number of counts in the monitor detector. To find the elastic cross sections, angular distributions were measured for the enriched and

^{12}C targets and separately normalized to the monitor. Next, the ^{12}C contribution is found from the ratio of the lower energy ($^{13}C+^{12}C$) peaks in both spectra. Normalizing the angular distribution of the ^{12}C target by this ratio will give the correction. Again, the points are corrected for ^{16}O scattering. The final curves were then normalized to the previously obtained excitation functions.

The angular distributions are of lower quality than the excitation data because: 1) more corrections were applied, and 2) they are more susceptible to systematic errors. Because both detectors were on the same side of the beam, inaccuracies in the beam spot position were not averaged. The angular distribution would also tend to be averaged over the angular acceptance of the apertures and beam spot size, and energy due to straggling. This would tend to "fill in" the minima, although this is a 10% effect, at most. The most serious systematic effect is that of distortion of the angular scale by slow wandering of the beam spot, probably due to improper focusing of the beam. An error of 1° in the laboratory measurements at 70° distorts the data by about 20%. Simply shifting the laboratory scale of the data to enforce symmetry about 45° indicates an error of $\sim 0.5°$ for the data sets at both energies.

As in the excitation functions, the angular distributions are fairly insensitive to carbon buildup, oxygen contamination, and energy loss in the target. Target thickness and beam current are monitored effectively, but are vulnerable to angular errors. Finally, peak error determination at angles greater than about 75° proved too unreliable for analysis due to straggling, detector noise, and low energy contaminants.

Table 3 and fig. 19 exhibit the angular distribution cross sections and their statistical errors. An estimated, roughly constant distortion of

about 10% over the angular range covered by the data could arise from small uncertainties in the scattering angle ($\Delta\vartheta_{lab} \sim 0.5°$).

D. Previous Measurements

1. Fusion

There are few reported measurements of the low energy $^{13}C+^{13}C$ system. A search for quasi-molecular resonances by Halbert and Nagatani (Ha72) in the range $11.5 \leq E_{lab} \leq 16$ MeV found the excitation function but did not establish the absolute yields. The total fusion cross section and production of ^{24}Mg were measured over the range $3.05 \leq E_{c.m.} \leq 6.88$ MeV by Chatterjee *et al.* (Ch80) by the NaI method, as discussed in Chapter I. Dasmahapatra *et al.* (Cu81, Da82) have remeasured a few points and corrected for the (radiationless) ground state branching; however, the experiment is essentially identical. All three data sets are compared in fig. 20.

(To facilitate comparison of our data, cross sections have been converted to S(E) (eqn. I.A.1)). The value of $2\pi\eta = 90.832/\sqrt{(E_{c.m.})}$. For obscure reasons, the S-factor of refs. Ch80, Cu81, and Da82 were converted using $2\pi\eta = 90.775/\sqrt{(E_{c.m.})}$. This error is only about 2% for the lowest energies, but for consistency, all data quoted or graphed in this thesis have been corrected to our definition.)

Above $E_{c.m.} = 4$ MeV there is excellent agreement (5-10%) among the data sets, but we diverge fairly strongly below this, where the Ge(Li) data are ~50% lower. This discrepancy is probably caused by hydrogen contamination in the targets used by Chatterjee *et al.* (Ch80). Since their experiment does not resolve most of the individual transitions, their

detectors would be sensitive to the 8.062 MeV γ-rays from the reaction $^{1}H(^{13}C,\gamma)^{14}N^{*}$. Unless very special precautions are taken, the normal concentration of hydrogen in evaporated carbon is at least of the order of a few tenths of an atomic percent (Ke80). Although Chatterjee *et al.* examined their Ge(Li) and NaI spectra for the presence of contaminants, this check was performed at only a few beam energies between 9 and 11 MeV. The reaction $^{13}C(p,\gamma)^{14}N^{*}$ has a resonance at $E_{c.m.}$ = 0.512 MeV ($\Gamma_{c.m.}$ = 30 keV), corresponding to a ^{13}C bombarding energy of 7.163 MeV. Taking into account the energy loss in their target, the effective $^{13}C+^{1}H$ resonance energy on the $^{13}C+^{13}C$ scale in fig. 20 is $E_{c.m.}$ = 3.77 MeV ($\Gamma \sim 400$ keV), which is precisely the area of disagreement between the two data sets.

It is possible to be more precise about this effect by utilizing the detector efficiencies given in (Ch80). One can estimate the total detection efficiency for 8.062 MeV gamma rays by knowing the efficiency at E_γ= 1.37 MeV and scaling standard NaI efficiency tables ($\varepsilon_t \sim 0.33$; they have already given the cascade detection efficiency as ~ 0.49. The $^{14}N^{*}$ γ yield can be calculated from the published resonance parameters ($\omega\Gamma_\gamma$ = 9.2 eV) (Aj76). The observed disagreement in the S-factors of 50% could be produced by a hydrogen concentration as low as 0.2 atomic percent. This concentration is the same order of magnitude as that of a single monolayer of adsorbed water or hydrocarbons.

2. Elastic Scattering

We have compared our elastic scattering data with previous measurements. The elastic scattering excitation function at $\vartheta_{c.m.} = 90°$ was taken from the graphs given by Korotky *et al.* (Er80, Ko81), while the excitation functions at $\vartheta_{c.m.} = 60°$ and 90°, and an angular distribution at $E_{c.m.} = 8.0$ MeV were compared to the graphical data taken from Helb *et al.* (He73). The excitation functions of Helb *et al.* extend down to $E_{c.m.} = 7.0$ MeV. Their excitation functions at both 60° and 90° are in excellent agreement with ours (fig. 18). We also found quite good agreement with their angular distribution measured at $E_{c.m.} = 8.0$ MeV (fig. 19).

Our data for elastic scattering at 90° differs strongly from that of Korotky *et al.* They found a much larger cross section immediately above the Coulomb barrier. There is very good agreement between 5 and 7 MeV, but above 7.5 MeV, their values abruptly jump nearly 100% higher than ours. In their experiment, they used a kinematic coincidence technique to distinguish ^{12}C from ^{13}C. Since those data lie at the extreme lower limit of their energy range, this suggests that the reliability of their $^{12}C/^{13}C$ discrimination may be deteriorating as the energy is lowered. Further speculation concerning this discrepancy should await the publication of a fuller account of their experiment.

III. Carbon Isotope Fusion

A. Low Energy Data

Low energy fusion data in the carbon isotopes present a somewhat misleading picture. Fig. 21 is a comparison of the S-factor data of the carbon systems available prior to the year 1980. The references are given in the figure caption. The general impression is that in $^{12}C+^{12}C$ and $^{13}C+^{13}C$ there is an upturn in the S-factor at extremely low energies, while for $^{12}C+^{13}C$ there is a leveling or slight falloff. Let us examine this more carefully.

The strongest evidence for a low energy rise in the $^{12}C+^{12}C$ S-factor is the light particle data of Mazarakis and Stephens (Ma73b). Researchers have suspected for some time that there is a systematic shift of $\Delta E_{c.m.} \sim -50$ keV in these points, based on the location of the resonance energies (Ke80). At these low energies, the S-factor conversion factor $E\,exp(2\pi\eta)$ is an enormous number, and a rapidly varying function of energy. A change of 250 keV in energy translates to an order of magnitude in $S(E)$. When the target energy loss in the laboratory is about 250 to 500 keV (as it is in most studies) the attendant errors on the S-factors should be exhaustively checked.

A careful reading of Mazarakis's thesis (Ma71) and later correspondence (St72) reveals a number of errors. In their experiment, the beam energy was calibrated against proton groups from the $^{2}H(^{12}C,p_0)^{13}C$ reaction at $E(^{12}C) = 7.0$ MeV. This gave a 0.71 percent correction to the energy defined by the proton NMR reading of the 90° analyzing magnet, previously calibrated by the $^{27}Al(p,n)$ threshold. It appears that this correction was subtracted, rather than added, to the NMR-defined energy. A

proper correction would shift their lowest data point by +40 keV, and the highest point by +70 keV, in the center of mass.

We mention in passing that the energies given by Mazarakis and Stephens are those at the center of the target. Although an effective energy "correction" was applied, it was computed improperly; it is only about half of the true correction and amounts to a 20-40% decrease in the lowest points. Reconstructing the exact bombarding energies, target thicknesses and cross sections (St72) allows a more sophisticated determination of the effective energies. We include the approximate influence of the known resonances in eqn. II.C.6. The correctly determined points are compared to the original data in fig. 22. A few lower energy points have changed by factors of two, and any general upswing of the $\tilde{S}$-factor is questionable. For comparison, we have also included a recent measurement of the light particles by Becker *et al.* (Be78, Be81b). The corrections to the energy scale in the more recent data have been corroborated by a very careful determination of effective beam energies using several thin (9, 13, 14, and 55 $\mu g/cm^2$) targets (Ke80). In contrast, the lowest energy point of Mazarakis used a 65 $\mu g/cm^2$ target.

Uncertainty in the target energy loss (*e.g.*, from target thickness errors) produces not merely a systematic error, but an energy-dependent distortion of the S(E) or $\tilde{S}(E)$ curves. When counting statistics are negligible, the systematic error in the S-factor is approximately:

$$\Delta S(E)/S(E) \sim \pi\eta(\Delta E/E) \quad . \qquad \text{III.A.1}$$

At bombarding energies greater than 12 MeV, an error of ±20% in the thickness of a 50 $\mu g/cm^2$ target translates to an error of less than 5% in

the S-factor. But at $E(^{12}C) = 5$ MeV, the same error is more than 30%. Below $E_{c.m.} \sim 3.2$ MeV, the interaction of energy loss and resonance structure further compounds the worsening distortion of expression III.A.1, and large errors are unavoidably introduced into S(E).

Target energy loss problems can be handled in two ways: by very thick or very thin targets. Thick target data (Hi77) suggest general features of the cross section such as a pronounced minimum in $\tilde{S}(E)$ at $E_{c.m.} \sim 3.1$ MeV, and a possible resonance below that. It must be remembered, though, that these points are effectively averaged over $\Delta E_{c.m.} \sim 125$ keV. To assess the distortion induced by unfolding the thick target data, we have reconstructed the bombarding energies of High and Cujec (Hi77) and recomputed the effective energies and $\tilde{S}$-factors, assuming $\tilde{S}$ is proportional to the resonance structure found in recent thin target data (Ke80). These errors are in the 10% range. Because the relative minimum in $\tilde{S}(E)$ near $E_{c.m.} = 3.0$ MeV was checked very carefully by repeated measurements, we tentatively accept the thick target data down to this point.

As a final remark on the low energy $^{12}C+^{12}C$ data analysis, we find it curious that no estimate of the effect of ^{13}C has been made, despite the use of natural carbon targets. It is possible that it is sizable, particularly in gamma experiments, where it is difficult to separate $^{12}C(^{12}C,p)$ from $^{12}C(^{13}C,pn)$ and $^{12}C(^{12}C,\alpha)$ from $^{12}C(^{13}C,\alpha n)$. Although the isotopic abundance is only 1.1%, its contribution may be amplified by several effects. Firstly, the experimental ratio $\sigma(^{12}C+^{13}C)/\sigma(^{12}C+^{12}C)$ seems to grow larger (on the average) with decreasing energy. This is because the $^{12}C+^{12}C$ cross section is smaller than "expected" from its average behavior at higher energies. Secondly, the excess neutron in ^{13}C has a low

binding energy and a small potential barrier. Therefore, the pn and αn evaporation channels are a large part of the $^{12}C+^{13}C$ cross section. These two effects combine to enhance the yield by a factor of roughly 2 to 10. Finally, a given ^{12}C bombarding energy looks 4% higher in the $^{12}C+^{13}C$ system. This contributes an additional factor of about 3 ($E_{c.m.} \sim 3$ MeV). Depending on the details of the branching to residual nuclei in $^{12}C+^{13}C$, this effect may result in the overestimate of the $^{12}C+^{12}C$ cross sections by 5 to 50% below $E_{c.m.} < 4$ MeV.

Published gamma spectra (Hi77, Ke80) for ^{12}C on natural carbon targets show gamma rays characteristic of the $^{12}C+^{13}C$ reaction, often unlabeled or attributed to other sources. In particular, one finds the expected gamma peaks at 350.5, 472, and 1369 keV from the alpha, proton, and neutron channels, respectively. The lines at 440, 871, and 1369 (pn, $\alpha\alpha$, and αn) are either masked by $^{12}C+^{12}C$ or very weak. Taking approximate numbers from the spectrum at $E_{c.m.} \sim 3.0$ MeV given in (Hi77) would place the $^{12}C+^{13}C$ correction to the proton and alpha cross sections at about 10-15%. Without $^{12}C+^{13}C$ data at lower energies, it is impossible to predict whether this effect becomes greater or smaller at still lower energies.

It would be disingenuous of us to rely on the low energy $^{12}C+^{12}C$ data (Pa69, Ma73b, Hi77) without a clear demonstration of the magnitude of the above effects. A comparison of the $\tilde{S}$-factors of these three groups (with effective energy corrections) and the most recent data (Be78, Be81b) is given in fig. 23. Notice the thin target data (Be78, Be81b)($\Delta E_{c.m.} \sim 30-70$ keV) match the other data well in magnitude at the resonance peaks, but are somewhat lower off-resonance. With peaks spaced so closely together, this effect could come from smearing the cross section over larger energy bins ($\Delta E_{c.m.} \sim 125-150$) keV.

In the light of the above-mentioned corrections and recent measurements, a more cohesive picture of carbon isotope fusion is forthcoming. The experimental data, summarized in fig. 24, now argue for a leveling-off or even a downturn in the S-factor (or its average behavior) at the lowest accessible laboratory energies. That the S-factor deviates from its linear behavior near the barrier is not entirely unexpected; this subject is examined in the next section.

B. S-factor

1. Definition

Before returning to our comparison of the carbon isotopes, it would be profitable to examine the expected energy dependence of the S-factor. The S-factor is normally extracted from the $l = 0$ Coulomb barrier penetrability (Ev55). The cross section is related to the transmission coefficients:

$$\sigma = \pi \lambda\!\!\!^{-2} \sum (2l+1)\, T_l \qquad \text{III.B.1a}$$

$$\sim S(E)\, E^{-1}\, T_0 \quad , \qquad \text{III.B.1b}$$

where $\lambda\!\!\!^{-2} = \hbar^2 / 2\mu E_{c.m.}$. At energies well below the barrier, the transmission coefficient has the well-known Gamow form:

$$T_0 = e^{-\gamma} \quad , \qquad \text{III.B.2}$$

with

$$\gamma \equiv \frac{2}{\hbar}\sqrt{2\mu}\int_{r_1}^{r_2}[V(r)-E]^{1/2}dr \quad , \qquad \text{III.B.3}$$

where r_1 and r_2 are the (classical turning points for a system of reduced mass, μ, and energy, E, penetrating a potential, $V(r)$. The standard assumption is to take r_1 to be the internuclear grazing distance, R; therefore the nuclei tunnel through the *exterior* Coulomb potential until their surfaces touch, and they fuse. In this case, $V(r) = Z_1 Z_2 e^2/r$ and integral III.B.3 can be performed analytically to yield:

$$\gamma = 4\eta\,[\cos^{-1}(E/B)^{1/2} - (E/B)^{1/2}(1-E/B)^{1/2}] \quad , \qquad \text{III.B.4}$$

where B is the Coulomb barrier height, $Z_1 Z_2 e^2/R$. With these assumptions, γ has the (approximate) energy dependence:

$$\gamma(E) \sim 2\pi\eta + C + gE \qquad \text{III.B.5a}$$

or

$$S(E) \propto exp(-gE) \quad ; \quad g \equiv \frac{1}{3}(8\mu R^3/Z_1 Z_2 e^2\hbar^2)^{1/2} \quad . \qquad \text{III.B.5b}$$

Unfortunately, few heavy ion systems can be studied down to energies where these approximations are valid. For the available data, it would be worthwhile to find a simple parametrization of the cross section which is valid in the region $0.5B < E_{c.m.} < B$. Examination of a number of light/heavy ion systems suggests that at least the functional form of eqn. III.B.5a may hold over certain energy regions. It may be possible to find a simple method to extend the applicability of the S-factor to the low

energy behavior of heavier systems. We will consider three possible errors in our initial assumptions, and compute their effects to at least order E^2 in the expansion III.B.5a. These three errors are the form of the transmission coefficient, the shape of the barrier, and the influence of higher partial waves.

2. Modifications

The functional form of the transmission coefficient depends on the exact shape of the potential barrier, particularly when the potential changes appreciably over distances comparable to the de Broglie wavelength. The Gamow factor is only valid at very low energies ($E \ll B$), where it is insensitive to the details of the barrier top. Since nuclear surfaces are diffuse over distances on the order of 1 fermi, physically, one would expect any features of the potential to be averaged over a similar length scale. Thus smoothed, any potential would behave roughly quadratically near the maximum. For parabolic barriers, the WKB method gives the general form for the transmission function (Ke35):

$$T = (1+e^{\gamma})^{-1} \quad , \qquad \text{III.B.6}$$

where γ is defined in III.B.4. This formula is not restricted to low energies, but is valid up to the barrier height, and may be extended beyond that by allowing the (semiclassical) turning points to become imaginary. Notice that this form reduces to the conventional Gamow factor for large γ ($E \ll B$), but is only half that value at $E = B$. (See fig. 25) The discrepancy between the two expressions becomes severe in the region $E/B \geq 0.8$, but may be safely ignored below about 0.7.

We have thus far assumed that when two nuclei approach to within a critical distance, they fuse. In simple models, this is taken to be the radius at which they "touch," and adjustments of this parameter are made to fit the data. It is not difficult to allow the more realistic situation where the critical radius for fusion, R_c, may be inside the nuclear surface, R. The nuclei are exposed to a lower Coulomb barrier here; closer, say, to that of two interpenetrating spheres. (The nuclear potential will also act to lower the barrier height, but the Coulomb force still dominates just inside the surface.) This distorts the energy dependence of the cross section because fusion will be relatively easier at higher energies.

To make an estimate of this effect we take the Coulomb force at close distances to be that of a point charge inside a uniform, spherical, charge distribution. This case can be integrated exactly to give:

$$\gamma = \gamma_0 + \left(\frac{\mu}{\hbar^2}BR^2\right)^{1/2}\left\{(a^2-1)^{1/2} - x_1(a^2-x_1^2)^{1/2} + a^2\left(\sin^{-1}\frac{1}{a} - \sin^{-1}\frac{x_1}{a}\right)\right\}, \qquad \text{III.B.7}$$

where $x_1 = R_c/R$ and $a^2 = 3 - 2E/B$. The choice of the critical radius now has a tremendous effect on the absolute value of the cross section, but this can be partially offset by a redefinition of the constants C and g in III.B.5a. Residual terms introduce nonlinearities of the order of 15% into the subbarrier expansion of $\gamma(E)$. As is our discussion of the transmission function, this correction is of the correct sign and magnitude to account for observed discrepancies with data.

(In the following discussion we will confine our attention to reactions between p-shell nuclei, $9 \leq A \leq 16$. If not stated otherwise, specific

numbers refer to the $^{12}C+^{12}C$ system.)

The third assumption of s-wave dominance is grossly inadequate for heavy ions. The centrifugal potential for $l = 5$ raises the barrier height by only about 1 MeV. Obviously, the transmission functions will be comparable. Some useful insight can be obtained from an expression for the total cross section due to Wong (Wo73, De81). In each partial wave the potential may be approximated by a parabolic barrier, characterized by a common position, R, and curvature, $\hbar\omega_0$, with varying height

$$E_l = E_0 + \frac{\hbar(l+\tfrac{1}{2})^2}{2\mu R^2} \quad . \qquad \text{III.B.8}$$

Explicitly,

$$V_l(r) = E_0 - \tfrac{1}{2}\mu\omega_0^2(r-R)^2 + \frac{\hbar(l+\tfrac{1}{2})^2}{2\mu R^2} \quad . \qquad \text{III.B.9}$$

Transmission functions for each partial wave are given by the well-known Hill- Wheeler expression (Hi53):

$$T_l(E) = \frac{1}{1+\exp\dfrac{2\pi(E_l - E)}{\hbar\omega_l}} \quad . \qquad \text{III.B.10}$$

Setting $x = l + \tfrac{1}{2}$, we replace the sum over l by an integral (Wong's formula):

$$\sigma_T = 2\pi\lambda\!\!\!^{-2} \int_0^\infty \frac{x\,dx}{1+be^{ax^2}} = \frac{\pi\lambda\!\!\!^{-2}}{a}\ln\left[1+\frac{1}{b}\right] \quad , \qquad \text{III.B.11}$$

where

$$\alpha = \frac{\pi \hbar c^2}{(\hbar \omega_0)(\mu c^2) R^2} \quad \text{and} \quad b = \exp\left[\frac{2\pi}{\hbar \omega_0}[E_0 - E]\right] .$$

These formulae are valid in the vicinity of the Coulomb barrier. They may be used to find the fraction for the reaction strength residing in each partial wave. At the barrier we find the s-wave contributes less than 10% of the total. Using Wong's formula as a guide, and examining more exact model calculations, several model-independent features can be discerned.

The sub-barrier cross sections of p-shell nuclei are essentially governed by the lowest few partial waves ($l < 8$). The simplest case is $^{12}C+^{12}C$ where symmetry forbids states of odd orbital angular momentum. We need only consider $l = 0$, 2, and 4. The behavior of these transmission functions is shown in fig. 26. Sub-barrier fusion is dominated to the lowest energies by the partial wave $l = 2$ ($\sigma_2/\sigma_T \sim 50\%$). The S-wave fraction falls about linearly from its low energy maximum ($\sim 40\%$) to nearly zero just above the barrier. The behavior of the $l = 4$ fraction is anti- correlated with this; it rises from zero at low energies to about 40% at the barrier. At greater energies, higher partial waves quickly predominate.

With non-identical reactants, the cross section strength is shared more evenly amongst the lowest few partial waves, as shown in fig. 27 for the $^{12}C+^{13}C$ system. It is likely that two or three partial waves predominate; shifting smoothly from $l \leq 2$ for $E \leq B/2$ to $l \geq 2$ for $E \geq B/2$. Again, higher partial waves enter quickly above the barrier.

When only a few partial waves contribute, spin may have an important effect on their relative contribution in identical particle systems. For nuclei of spin, I, the spin-averaged cross section is:

$$\sigma_T = \pi \lambda\!\!\!^{-2} \sum_{l=0}^{\infty} \left[1 + \frac{(-1)^{l+2I}}{2I+1} \right] (2l+1)\, T_l \quad . \qquad \text{III.B.12}$$

Identical particles of spin ½ are required to be in a totally antisymmetric relative wavefunction (product of space times spin factors). On the average there are three times as many symmetric as antisymmetric spin states; therefore, odd l (anti-symmetric) orbital angular momenta will be 3 times as likely as even l. This is evident in $^{13}C+^{13}C$, where $l=1$ and $l=3$ are the primary fusion channels, and $l=1$ is 50% of σ_T below about 5 MeV.

The action integral, $\gamma(E)$, cannot be evaluated analytically for a Coulomb plus a centrifugal barrier. Many approximate formulae have descended to us from studies of the α-decay of heavy elements (*e.g.*, Ga49). To an accuracy relevant in our calculations, a higher angular momentum wave perceives a slightly higher barrier:

$$B_l = B\,(1+\sigma_l) \quad , \qquad \text{III.B.13a}$$

where

$$\sigma_l = [\,l(l+1)\hbar^2/2\mu R^2\,]/\,B \ll 1 \quad . \qquad \text{III.B.13b}$$

Performing the low energy expansion of γ,

$$\gamma_l = 2\pi\eta + C_l + g_l E \quad , \qquad \text{III.B.14a}$$

with

$$C_l = C_0(1-\sigma_l/2) \qquad \text{III.B.14b}$$

and

$$g_l = g\,(1-3\sigma_l/2) \quad . \qquad \text{III.B.14c}$$

Inclusion of higher partial waves has the effect of reducing the slope of $\ln S(E)$. The magnitude of this effect is comparable for the systems $^{12}C+^{12}C$ and $^{13}C+^{13}C$. The parameter g_1 could be as much as 10-15% smaller than g_0. In $^{12}C+^{13}C$ this effect is less, only about 5%.

We list, then, the following conclusions: The canonically defined S-factor appears to be the highest-order, model-independent, energy dependence which can be factored out of the heavy ion cross fusion cross sections. Each of the above considerations produces effects at least of order C and E in the low energy expansion of $\ln(S)$. By fortuitous cancellation, corrections of order E^2 may be suppressed in the region of the barrier, and again, very far below the barrier. Nevertheless, there is no simple way to relate C and g to physical features of the nuclei. The renormalization of these constants is minimal only in certain cases, namely, collisions between light and/or identical p-shell nuclei, for $E < B/2$. The presence of resonance structure in several of these systems further reduces the utility of simple models.

C. Model Calculations

1. Standard Model

Historically, our efforts to describe low energy scattering rely on the concept of the optical potential. Together with the theory of resonances, this has been the main thrust of more exact quantum mechanical models. As both a method and a language, the success of potential scattering in light particle reactions makes it seems a natural step to extend the optical potential to heavier systems. Although these potentials may not be simple, they represent the only practical alternative to the unwieldy and complex microscopic theories.

It is not obvious that heavy ion scattering is reconcilable with potential scattering. Microscopically, of course, the nuclear-nuclear force is non-local, since the relative motion of the nuclei disturbs their internal motion. Mathematically, the Schroedinger integro-differential equation for the wavefunction, $\psi(\vec{r})$, contains (in addition to the local Coulomb and centrifugal parts) the term:

$$\int V(\vec{r},\vec{r}')\,\Psi(\vec{r}')\,d\vec{r}' \quad .$$

Expanding $\Psi(\vec{r}') = \sum_{l,m} \Psi(r')\, i^l\, Y_l^m(\vartheta',\varphi')$ in a series about r (Ho71),

$$\int V(\vec{r},\vec{r}')\,\Psi(\vec{r}')\,d\vec{r}' = \int V(\vec{r},\vec{r}') \sum_{l,m} \left[\Psi(r) + (r'-r)\frac{\partial}{\partial r}\Psi(r) \right.$$

$$\left. + \frac{(r-r')^2}{2}\frac{\partial^2}{\partial r^2}\Psi(r) + \ldots \right] \times i^l\, Y_l^m(\vartheta',\varphi') \quad . \qquad \text{III.C.1}$$

Making the canonical operator substitution ($\partial / \partial r \rightarrow -ip/\hbar$) and integrating over angles, we get

$$\int V(\vec{r},\vec{r}')\,\Psi(\vec{r}')\,d\vec{r}' = V_o(r) + V_2(r)p^2 + \ldots \quad . \qquad \text{III.C.2}$$

Thus we find that a non-local potential is formally equivalent to an energy-dependent local interaction. Small non-local influences may be compensated by a simple linear energy dependence, albeit, in practice this magnifies the difficulty of applying the optical model.

One approach is to pick a class of similar nuclei and compare their measurements with a physically reasonable model. The standard strong absorption optical potential, like most models, assumes a centrifugal barrier and a point-sphere Coulomb interaction and relegates all degrees of freedom to the nuclear strong force. They are taken to be the strength, $(V_o + iW_o)$, radius, $R_o = r_o\,(A_1^{1/3}+A_2^{1/3})$, and diffuseness, a, of a Woods-Saxon potential:

$$V_N(r) = -(V_o + iW_o)(1 + \exp[(r - R_o)/a])^{-1} \quad . \qquad \text{III.C.3}$$

The so-called "standard" optical model (St76) arose originally from a study of the exceptional systems $^{12}C+^{12}C$, $^{12}C+^{16}O$, and $^{16}O+^{16}O$ (Mi72, Mi73). For this reason, and reasons of convenience, the standard model gives V_o a large value. This decision has a practical element: the results are insensitive to V_o for large V_o, thus restricting the parameter search to variations of r_o and a. (W_o is set large enough to damp reflection resonances from the centrifugal barrier.) Thus the strength parameters are fixed at V_o = 50 MeV and W_o = 10 MeV. From their fit of 9 heavy ion

systems they conclude that $r_0 = 1.27$ fm and $a = 0.40$ fm.

The standard model suffers from a number of flaws. It is crucial to note that 3 of the 9 systems which were used to fit r_0 and a were the (atypical) α-conjugate systems $^{12}C+^{12}C$, $^{12}C+^{16}O$, and $^{16}O+^{16}O$. The low energy $^{12}C+^{12}C$ data were those of Mazarakis and Stephens (Ma73b) which we have discussed in the previous section. Likewise, there is evidence that the $^{16}O+^{16}O$ cross sections may be in error by 50% or more (Hu80). It should also be pointed out that satisfactory fits are obtained only in 2 or 3 of the 9 cases; the systems $^{10}B+^{12}C$, $^{11}B+^{12}C$, and (possibly) $^{14}N+^{14}N$. In the remaining cases, the standard model has the wrong energy dependence. When fitted near the Coulomb barrier, the low energy cross sections are too high, often by a factor of two at $E \sim B/2$. The predictions of the standard model for the carbon isotopes are compared to the low energy data in fig. 28.

Stokstad (St80) has shown that the standard model is only adequate for very light ions on boron isotopes. Deviations begin to appear for projectiles as light as ^{14}N. For other pairs of p-shell nuclei the standard model is, again, too large at low energies (when fitted at the Coulomb barrier).

2. Incoming Wave Boundary Condition (IWBC) Model

A full search of parameter values in a general optical model is prohibitively time-consuming. The presence of an imaginary potential multiplies this difficulty, as well as obscuring the physical interpretation with additional ambiguities in fitting. An alternative quantum-mechanical prescription for achieving absorption can be made by imposing an incoming wave boundary condition (IWBC), *i.e.*, at a specified radius one allows

only incoming waves (Ra63, Ch77a). This calculation is insensitive to the form of the potential inside this radius, thus obviating the need for an imaginary potential. (Recall that the role of W_0 in the standard model was to absorb waves reflected from the centrifugal barrier.)

A study of this model for $^{12}C+^{12}C$, $^{12}C+^{16}O$, and $^{16}O+^{16}O$ was made by taking $V_0 = 50$ MeV, as before, and varying r_0 and a (Ch77a). The value of these fusion data is still questionable, but the emphasis of this study was on the elastic scattering. While the values of r_0 and a did not vary systematically, large values of $a (> 0.6$ fm) were required to fit the elastic scattering excitation functions. Our own investigations of $^{13}C+^{13}C$ confirm this. The curves in figs. 29 (elastic excitation functions) and 30 (angular distributions) demand $a > 0.60$ fm. However, while it is true that the fusion data (fig. 31) can be matched fairly well with the values $R_0 = 5.19$ fm and $a = 0.64$ fm, the cross section once again has the wrong energy dependence.

3. Realistic Optical Potential

More "universal" parameters of the internuclear potential have emerged from a survey by Christensen and Winther (Ch76) of the elastic scattering data for more than 50 systems. Assuming a deep central well, their investigation of the realistic ion-ion potential gives:

$$r_B = 1.07(A_1^{1/3} + A_2^{1/3}) + 2.72 \text{ fm} \quad , \qquad \text{III.C.4}$$

and

$$a = 0.63 \text{ fm}. \qquad \text{III.C.5}$$

Despite the apparent desription of elastic scattering, a blind attempt to use these parameters produces a poor fit to fusion data. Switkowski *et al.* (Sw77) have shown this to be true for the systems $^{12}C+^{14}N$, $^{14}N+^{14}N$, and $^{14}N+^{16}O$. They find instead that a equals about 0.4 fermis. This inconsistency arises because we have been too vigorous in our simplifying assumptions.

When η is large, low energy elastic scattering of distinguishable particles has relatively few features; *i.e.*, the energy for which the cross section deviates from Rutherford, and the energy slope of this curve. Ultimately, these can be shown to depend strongly on only one potential parameter, the barrier height, V_B, with a weaker dependence on its radial position, r_B (Ma73a). Fusion, naively speaking, must depend on two parameters: the geometrical cross section $\sim r_B^2$, and the barrier penetration probability, which is roughly a function of the width times the height of the barrier. Thus, only two parameters can possibly be well-determined by the low energy data. If we substitute, instead, the three parameters, V_0, r_0, and a, then we should expect some continuous ambiguity to exist among them (Si74). For certain ranges of parameter values, this might be expressed as a functional relation. With reasonable accuracy, we find the approximate equation for the barrier height:

$$V_B \sim \frac{Z_1 Z_2 e^2}{r_B}\left(1-\frac{a}{r_B}\right) , \qquad \text{III.C.6}$$

where r_B solves the implicit relation

$$R_0 = r_B - a\ln[\kappa - 1 + (\kappa^2 - 2\kappa)^{1/2}] \qquad \text{III.C.7}$$

and

$$\kappa \equiv r_B^2 V_0 / 2 Z_1 Z_2 e^2 a \quad . \qquad \text{III.C.8}$$

This effectively reduces the number of degrees of freedom from 3 to 2. Thus, V_0, r_0, and a are not uniquely determined by low energy scattering, and the exact values found by different parameter searches need not vary systematically.

In the above-mentioned studies, V_0 was assumed to be large for simplicity. By varying a and r_0 it is possible to fit the elastic scattering. This fixes V_B, albeit, with large values of a. Because the radial position of the barrier top is well outside the strong interaction radius to which the absorptive potential is bound, we know the real potential must predominate at low energies. The fusion cross sections from parameter fits to the elastic scattering do not fall with energy as fast as the data, unmistakable evidence that the barrier is not wide enough at low energies. The "true" ion-ion potential should retain the same barrier height as predicted by elastic scattering, yet increase the barrier width still further. Both conditions can be satisfied by reducing V_0 ($\sim$15 MeV). To some extent V_0 and a are now redundant and their exact values will be ill-determined; however, this family of potential shapes should be capable of describing both elastic and fusion data.

A barrier penetration and critical radius model (which incorporates the improvements of the previous section) has recently been analyzed by Descouvement *et al.* (De82). They are very successful in describing fusion between p-shell nuclei from the sub-barrier region up to *yrast* energies, where the critical radius picture breaks down. For computational

purposes, they specify the three parameters of a shallow Woods-Saxon nuclear interaction and add the centrifugal and point-sphere Coulomb parts. The transmission coefficients for each partial wave were computed numerically, and the best fit parameters were found for each data set.

Next, they tested the sensitivity of their model with two different approximations to their potentials. By fitting the sub-barrier data of 16 light-heavy systems, they deduced the systematic variation of two (model-independent) features of the s-wave interaction, V_B and r_B.

$$r_B = 1.128\,(A_1^{1/3} + A_2^{1/3}) + 2.709 \text{ fm} \quad , \qquad \text{III.C.9}$$

$$V_B \equiv V(r_B) = 0.938\, Z_1 Z_2 e^2 / r_B \quad . \qquad \text{III.C.10}$$

Data exist for 4 systems ($^{12}C+^{12}C$, $^{12}C+^{14}N$, $^{12}C+^{16}O$, $^{16}O+^{16}O$) at energies high enough to weakly determine the critical radius, r_c. They find $r_c \sim 0.6 r_B$ ($\sim 0.8 R_o$). This is near the position of the relative maximum in the s-wave barrier.

Although Descouvement *et al.* did not check the elastic scattering, we have noted that this is largely fixed by V_B and r_B. Expressions for the systematic variation of V_B and r_B resulting from the elastic scattering fits of Christensen and Winther (Ch76) can be derived from eqns III.C.4, III.C.5, and III.C.6. These are to be compared with the fusion-determined counterparts III.C.9 and III.C.10. The agreement between both parameter sets is excellent. The barrier heights differ by less than 1%; r_B as found from elastic scattering is consistently 3.5% smaller than that for fusion.

The quality and consistency of these predictions lend credence to the idea that a shallow Woods-Saxon potential produces a more realistic barrier shape. A shallow real potential has another advantage: fewer reflection resonances, because a relative minimum or "pocket" exists for fewer higher partial waves. Constructive and destructive interference oscillations were a large effect in this barrier penetration model, especially above the barrier. Smooth cross sections were obtained by averaging the interference terms. The structure and shape of these resonances depends on the choice of critical radius; thus their presence or absence must be related to the absorptive part of the interaction.

Even well above the Coulomb barrier where some transmission coefficients approach unity, both fusion and elastic behavior are governed by barrier penetration. The largely real potential is dominated by the Coulomb and centrifugal forces and depends on the real nuclear potential only in second order. These facts can be used to restrict the form of the imaginary potential. One obvious constraint is that there cannot be appreciable absorption much beyond the radius of the real nuclear potential, and certainly well inside the the barrier radius. Another constraint is that the absorption may be energy-dependent. The imaginary potential, more than the real, embodies any non-local influences because absorptive processes are initiated by rearrangement and internal excitation. As these grow in importance with collision energy, so should the imaginary potential. Lastly, interference effects from waves reflected from deep inside the nucleus seem to occur, but are phase-averaged. The rarity, but not absence, of shape resonances and the energy-dependence constraint are consistent with a shallow imaginary potential at low energies.

Shallow complex optical potentials between heavy ions have been previously invoked by a Yale group (Re73) to explain the average behavior of $^{12}C+^{12}C$, $^{14}N+^{14}N$, and $^{16}O+^{16}O$ elastic scattering. Their real potential is a shallow Woods-Saxon form ($V_o \sim 10-20$ MeV). The imaginary part is proportional to a separate Woods-Saxon whose depth can vary linearly with energy. This study is valuable for its exploration of changes in each parameter. The presence of continuous and discrete ambiguities prevent one from drawing conclusions about the inferred potentials. However, barrier penetration through the real parts of the Yale potentials is, reportedly, in good agreement with the results of Descouvement *et al.* (De82).

The energy slope of the imaginary potential was found to affect only the magnitude of the high energy scattering (above about twice the barrier height), while only weakly affecting the position of scattering minima and maxima. The placement and character of these structures is mainly fixed by the real potential. When the real potential is adjusted at low energies, the slope of the imaginary potential can be forced to account for the normalization at higher energies. In principle, this procedure could be iterated to give the constant term also, but in practice there is too much ambiguity in the other parameters. It is sufficient to take W_o large enough to dampen any remaining low energy shape resonances ($W_o \sim 0.5-2.0$ MeV). The Yale study deduces a value for the energy slope in the range 0.1-0.2, but we must emphasize that none of their calculations "fits" the data, or even its average behavior, by any means.

Continuing in this vein, Korotky *et al.* (Ko81) have attempted to fit the $^{13}C+^{13}C$ elastic data in the energy region $7 < E_{c.m.} < 36$ MeV with a shallow, surface-transparent potential ($V_o = 16.0$ MeV, $W_o = 0.22 E_{c.m.}$,

$R_{real} = R_{imag} = 6.35$ fm, $a_{real} = 0.45$ fm, and $a_{imag} = 0.30$ fm). We have retained this same form and refitted this potential to our data by making only slight parameter adjustments. As in the IWBC model, the optical model could not fit the excitation functions at different angles simultaneously. The dotted curves in figs. 29, 30, and 31 were obtained by using $V_o = 12.5$ MeV, $W_o = 1.0 + 0.22 E_{c.m.}$, $R_{real} = R_{imag} = 6.35$ fm, $a_{real} = 0.52$ fm, and $a_{imag} = 0.30$ fm. The radial position and barrier height of the real parts of both potentials agree to 1% ($V_B = 6.05$ MeV, $r_B = 8.06$ fm). These values are in excellent agreement with the conclusions of Descouvement *et al.* ($V_B = 6.07$ MeV, $r_B = 8.01$ fm).

D. Molecular Wave Function Method

The optical potential is incapable of describing the $^{13}C+^{13}C$ angular distributions over a range of different energies. This failure may be the signal of an anomalous contribution to the nuclear-elastic amplitude caused by the presence of the loosely-bound valence neutrons. Excess neutrons have a pronounced effect on the elastic scattering of the other carbon systems: $^{12}C+^{13}C$ (Go68, Bo71), $^{12}C+^{14}C$, $^{13}C+^{14}C$ (Bo72), and $^{14}C+^{14}C$ (Ko80, Dr81). As we shall see, it is possible to formally consider the general problem of carbon isotope scattering, and then, to quantify the effect of neutron number in each of these systems.

Below the energy where the fusion mechanism saturates, and certainly below the barrier, the total reaction cross section is usually dominated by σ_{Fus}. It sometimes happens, though, that conditions are favorable for competition by direct reactions. Systems must be individually examined for these conditions, since low energy direct reactions depend strongly on the details of nuclear structure. Because the energy needed

for breakup into three nearly equal bodies is relatively high, the allowable direct reactions may be generically classified as transfer reactions. The most likely candidates (due to barrier penetration arguments) are neutral particle transfers, especially neutron transfer, or excitation (Coulomb excitation or inelastic scattering).

It is even possible for transfer reactions to dominate the low energy total reaction cross section. The light particle can be pictured as changing from one state of internal motion to another during the close encounter of the two heavy centers. The amplitude for transfer is, thus, proportional to a constant (the "coefficient of fractional parentage") times the overlap of the entrance and exit channel wavefunctions with the form factor of the transferred particle. Different methods of attacking this problem are usually tailored to one's knowledge of the entrance and exit wavefunctions, *e.g.*, Nucleon Tunneling (Be56a, Be56b), Coulomb T-Matrix Theory (CTM) (Gr62), or the Distorted Wave Born Approximation (DWBA) (Pe67). For the purposes of discussion we will use the DWBA. This theory is valid for transfers of small Q-value.

For the transfer $(a+c)+b \rightarrow a+(b+c)$ or $b\,(A,a)\,B$, we define:

$$
\begin{array}{ll}
\mu_i = m_A m_b/(m_A+m_b) & m_i = m_a m_c/m_A \\
\mu_f = m_B m_a/(m_B+m_a) & m_f = m_b m_c/m_B \\
k_i = (2\mu_i E_i{}^k/\hbar^2)^{1/2} & \alpha_i = (2m_i B^A/\hbar^2)^{1/2} \\
k_f = (2\mu_f E_f{}^k/\hbar^2)^{1/2} & \alpha_f = (2m_f B^B/\hbar^2)^{1/2} \\
k = \tfrac{1}{2}(k_i+k_f) & \alpha = \tfrac{1}{2}(\alpha_i+\alpha_f) \\
\Delta = m_i Z_a Z_c/\mu_i Z_b Z_A & \eta = \tfrac{1}{2}(\eta_i+\eta_f)
\end{array}
\qquad \text{III.D.1}
$$

where B^A and B^B are the binding energies of particle c in nuclei A and B, respectively. When Q and the bombarding energy are not too large,

the DWBA matrix element is

$$M_{if} = \int_0^\infty F_{l_f}(k_f r)\, e^{-\kappa r}\, F_{l_i}(k_i r)\, dr \quad , \qquad \text{III.D.2}$$

where the F_l's are the regular Coulomb functions, and κ is

$$\kappa = \alpha_i \int^r dr\, [\, 1 + Z_a Z_c e^2/(1+\Delta) B^A r\,]^{1/2} \quad . \qquad \text{III.D.3}$$

Switkowski *et al.* (Sw74) noticed that $F_{l_f}(k_f r)$ has a maximum near the classical turning point in the exit channel, while the product of the two functions $e^{-\kappa r} F_{l_i}(k_i r)$ has a well-defined peak (at low energies). At a certain value of Q, the two peaks will coincide, and the transfer probability will be maximized. The optimum Q value occurs at:

$$Q_{opt} = \left[\frac{Z_B Z_a}{Z_A Z_b (1-\Delta)} - 1 \right] E_i + \left[\frac{Z_B Z_a}{Z_A Z_b (1-\Delta)} - 1 \right] \frac{\hbar^2 \alpha_i^2}{2\mu_i} \quad . \qquad \text{III.D.4}$$

When Q is not too large, the DWBA cross section is, to within spectroscopic factors, (Pe67):

$$\sigma_{tr}(E) \propto k^{-2} e^{B\eta \arctan(\alpha/2k)} \quad . \qquad \text{III.D.5}$$

Eqn. III.D.5 predicts several important properties of these reactions. When $Q \to Q_{opt}$ and $E_i \to 0$, we make the substitution $tg^{-1}(x) = \frac{1}{2} tg^{-1}(2x[1-x^2]^{-1})$ and obtain (to first order) the expression of Switkowski *et al.* (Sw74):

$$\sigma_{tr}(E) \propto E_i^{-1} e^{4\eta_i \arctan(\kappa/k_i)} \sim E_i^{-1} e^{-2\pi\eta_i + 2\eta_i k_i/\kappa - \cdots} \quad . \quad \text{III.D.6}$$

The value of η_i is large for heavy ions, so the probability for transfer can be comparable to that for fusion. Furthermore, depending on the higher order terms, this cross section need not diminish with energy as rapidly as fusion. It follows that below some energy, transfer must dominate.

It is obvious from the form of the matrix element, III.D.3, that the transfer process is greatly inhibited for Q much different from its optimum value. The reason for this is that the Coulomb functions oscillate with a period determined by $kr \sim 2\pi$. The main contribution to the matrix element comes from the overlap integral within about one half wavelength about the classical turning point in the outgoing wave. This coherence would be largely destroyed by a shift $\Delta kr_{max} \sim \pi/2$ in the phase of this wave. Thus, it is unlikely that sizable transfer cross sections will occur if Q_{exp} differs from Q_{opt} by more than a few MeV. The conditions for a large transfer cross section are satisfied in the case of elastic transfer of one or two loosely bound neutrons ($Q_{exp} = 0$, $Q_{opt} \propto m_n B^A/\mu_i$).

In principle, the only undetermined quantity in the transfer amplitude is the spectroscopic factor, which is a multiplicative constant. The total cross section, however, contains a second unknown in the relative phase of the optical and transfer amplitudes (Go68). This ambiguity may be avoided in a formalism which utilizes the underlying symmetry of the total amplitude: the Molecular Wave Function Method.

The Molecular Wave Function Method (MWFM) was originally used in atomic physics, and extented to heavy ions by v. Oertzen (Oe70). By analogy with atoms, the scattering is divided into the relative motion of the

two slowly-moving central cores, and the average motion of the loosely-bound valence particle(s). When the probability for transfer is high, the valence particles will be in molecular orbitals which can be constructed from the DWBA form factors by the Linear Combination of Nuclear Orbitals (LCNO). To simplify the problem, assume that only a single transfer amplitude will dominate (others will be suppressed by non-optimum Q-values), and thus, scattering will occur to only two molecular states (two state approximation).

Taking the example of $^{12}C+^{13}C$, we expand the total wavefunction as the product of the neutron wavefunction for relative separation of the heavy centers, $\chi(R)$. The total wavefunction must be symmetric with respect to interchange of the ^{12}C cores, separating the problem into even and odd L-wave solutions. (The subscript, p, can take values: $g=(+)=$ gerade or $u=(-)=$ ungerade.)

$$\Psi = \varphi_g \chi_g(L\ even) + \varphi_u \chi_u(L\ odd) \quad . \qquad \text{III.D.8}$$

The parity of the single particle states is $p(-)^l$, where l is the quantum number of the single particle shell model state. For the carbon isotopes, the valence neutrons will all be in the $p_{\frac{1}{2}}$-shell. The LCNO gives:

$$\varphi_p = \frac{1}{(2[1+p\Delta(R)])^{\frac{1}{2}}} \{\varphi_l(r) + p\,\varphi_l(r')\}_{g,u} \quad . \qquad \text{III.D.9}$$

The relative separation of centers A and A' is R, and $r(r')$ is the neutron co-ordinate with respect to nucleus $A(A')$. Substituting this into the Schroedinger equation, we multiply from the left by the molecular wavefunctions and integrate over the internal variables to get:

$$\left\{-\frac{\hbar^2}{2\mu}\nabla_R{}^2 + V_L(R) + iW(R) + E_p(R) - E\right\}\chi_{L,p}(R) = 0 \quad . \quad \text{III.D.10}$$

where

$$E_p(R) = \frac{K(R) + pJ(R)}{1 + p\Delta(R)}$$

$$K(R) = \int \varphi(r')\, V(r)\, \varphi(r')\, d\tau$$

III.D.11

$$J(R) = \int \varphi(r')\, V(r)\, \varphi(r)\, d\tau$$

$$\Delta(R) = \int \varphi(r')\, \varphi(r)\, d\tau$$

The net effect of neutron exchange is to perturb the relative motion of the centers with the symmetry-dependent, adiabatic potential, $E_p(R)$. We can incorporate $K(R)$ into the symmetry-independent potential, $V(R)+iW(R)$, to ensure that the asymptotic interaction is that of the complete system. The sign of the adiabatic potential depends on the symmetry of each partial wave. In $^{12}C+^{13}C$, the overall sign of the potential at large distances is $(-)^L$. The angular distribution, then, is mainly influenced by even L waves, for which E_p is repulsive. Conversely, odd L waves are preferentially absorbed.

The opposite is true in the case of $^{13}C+^{14}C$. Here we require anti-symmetrization under interchange of the ^{13}C cores (Oe73). Their relative wavefunction is now a product of space and spin factors. For core spin $\vec{J} = \vec{J}_1 + \vec{J}_2$:

$$\Psi = \sum_J \sum_L (\varphi_g{}^J \chi_{L,g}{}^J + \varphi_u{}^J \chi_{L,u}{}^J) \quad , \qquad \text{III.D.12}$$

where the molecular wavefunction now has the additional phase $(-)^J$;

$$\varphi_p = \frac{1}{(2[1+p(-)^J \Delta(R)])^{1/2}} \{ \varphi_l(r) + p(-)^J \varphi_l(r') \}_{g,u} \quad . \qquad \text{III.D.13}$$

The relative wavefunction is the solution of the differential equation for even and odd partial waves, for each value of J:

$$\{ -\frac{\hbar^2}{2\mu} \nabla_R{}^2 + V_L(R) + iW(R) + E_p{}^J(R) - E \} \chi_{L,p}{}^J(R) = 0 \quad , \text{III.D.14}$$

with

$$E_p{}^J = \frac{(-)^{L+J} J(R)}{1 + (-)^{L+J} \Delta(R)} \quad . \qquad \text{III.D.15}$$

The asymptotic form of the radial wavefunction is:

$$\chi^J \sim \frac{e^{iKR}}{R} \sum (f_{L,g}{}^J + f_{L,u}{}^J) \quad . \qquad \text{III.D.16}$$

Averaging over initial core spins $J = 0$ or 1 and summing over final states, the $^{13}C+^{14}C$ differential cross section is

$$d\sigma / d\Omega = \frac{1}{4} | 3 f^1(\vartheta) + f^0(\vartheta) |^2 \quad . \qquad \text{III.D.17}$$

The character of the angular distribution is determined by the statistical

weight of the $J = 1$ state. The sign of E_p for $J = 1$ is attractive for even angular momentum and repulsive for odd. This is the reverse of the previous case. Indeed, a comparison of the two systems $^{12}C+^{13}C$ and $^{13}C+^{14}C$ shows that at comparable energies, the anomalous structure in the angular distributions are of opposite phases (Bo72, Oe73).

The corresponding analysis for $^{12}C+^{14}C$ and $^{13}C+^{13}C$ is more complicated. The identical cores A and A' each have single particle states, φ_1 and φ_2, which may have different binding energies. Because the cores are spinless, the solutions once again separate into even and odd partial waves. The general form of the wavefunction for two identical valence particles outside of identical cores is:

$$\varphi_{p_1p_2} = \frac{1}{2+2p_1\Delta(R)}\{\varphi_1(r_1)\varphi_2(r_2) + p_1p_2\varphi_1(r'_1)\varphi_2(r'_2)\}+$$

$$\frac{p_1}{2+2p_2\Delta(R)}\{\varphi_1(r'_1)\varphi_2(r_2) + p_1p_2\varphi_1(r_1)\varphi_2(r'_2)\} \quad . \qquad \text{III.D.18}$$

The total wavefunction, Ψ, is built from linear combinations of $\varphi_{\mu\mu'}$. The asymptotic form of Ψ is, then, the sum of plane waves and even and odd spherical waves with amplitudes, $f^{\mu\mu'}$, calculated from the Schroedinger equation with symmetry-dependent energies, $E^{\mu\mu'}$. Oertzen and Bohlen (Oe75) give explicit expressions for $E^{\mu\mu'}$ when the cores have zero spin and the valence particles are non-interacting. Even partial waves require $p_1 = p_2$, while odd waves require $p_1 \neq p_2$:

$$E^{p_1p_2} = -p_1\left[\frac{J_1}{1+p_1\Delta_1} + \frac{(p_1p_2)J_2}{1+p_2\Delta_2}\right] \quad . \qquad \text{III.D.19}$$

The cross section for $^{12}C+^{14}C \rightarrow {}^{12}C+^{14}C$ (ionic) or $^{13}C+^{13}C$ (covalent) would be calculated with the valence neutrons is the anti-symmetric spin state ($S=0$):

$$(d\sigma/d\Omega)_{ion} = |\tfrac{1}{2}(f_g{}^{++} + f_g{}^{--}) + \tfrac{1}{2}(f_u{}^{+-} + f_u{}^{-+})|^2 \quad , \quad \text{III.D.20}$$

$$(d\sigma/d\Omega)_{cov} = |\tfrac{1}{2}(f_g{}^{++} + f_g{}^{--}) + \tfrac{1}{2}(f_u{}^{+-} - f_u{}^{-+})|^2 \quad , \quad \text{III.D.21}$$

where the covalent amplitudes are computed with $E = E_{c.m.} + Q$ to recover the difference in binding energies. In the covalent channel, the valence states are identical, so $f^{+-} = f^{-+}$, and the cross section is symmetric about $\vartheta_{c.m.} = 90°$. The symmetry dependence of two nucleon exchange is mixed into even and odd partial waves. Even partial waves have equal amplitude to be scattered by adiabatic potentials $\pm 2J(R)$, while odd L waves perceive a small, positive potential.

The ionic configuration in $^{12}C+^{14}C$ is clearly strong, since the Q-value for the single neutron transfer $^{12}C+^{14}C \rightarrow {}^{13}C+^{13}C$ is -3.23 MeV, and the covalent amplitudes would thus be much smaller. The asymptotic wavefunctions would then be almost purely ionic. In terms of the original wavefunctions:

$$\varphi_g = \frac{1}{\sqrt{2}}(\varphi_{++} + \varphi_{--})$$

III.D.22

$$\varphi_u = \frac{1}{\sqrt{2}}(\varphi_{+-} + \varphi_{-+}) \quad .$$

The adiabatic potentials are now (to first order in the overlap integrals):

$$E_g = \tfrac{1}{2}(E^{++} + E^{--}) = -(J_1\Delta_2 + J_2\Delta_1) \quad ,$$

III.D.23

$$E_u = \tfrac{1}{2}(E^{+-} + E^{-+}) = +(J_1\Delta_2 + J_2\Delta_1) \quad .$$

The net adiabatic potential is repulsive for odd L-waves and attractive for even L-waves. This is the same as $^{13}C+^{14}C$ and opposite to the situation in $^{12}C+^{13}C$. The binding energies for single neutrons in ^{13}C and ^{14}C are comparable, so we would expect that at the same c.m. energy (above the barrier), the structure in the elastic scattering of $^{12}C+^{14}C$ would be in phase with that in $^{13}C+^{14}C$. The magnitude of the two-particle exchange structure is smaller than in single-particle, since the potential relies on the overlap of two wavefunctions. These observations are all borne out by experimental data (Bo72, Oe75).

The asymptotic wavefunctions for $^{13}C+^{13}C$ must account for the symmetry in the spin variables of the valence particles:

$$\Psi = \varphi_g \chi_g \sigma_{S=0} + \varphi_u \chi_u \sigma_{S=1} \quad . \qquad \text{III.D.24}$$

The spin-averaged cross section is

$$d\sigma/d\Omega = \frac{1}{4}|f_+|^2 + \frac{3}{4}|f_-|^2 \quad , \qquad \text{III.D.25}$$

where f_p contains only even or odd partial amplitudes, computed with adiabatic energies:

$$E_p = (-)^{L+1} \frac{2\Delta(R)J(R)}{1 + (-)^L \Delta(R)^2} \quad . \qquad \text{III.D.26}$$

It is sufficient to specify $E_p(R)$ for large R only. At low energies, we have already stated that fusion and elastic scattering are insensitive to the interior nuclear potential. The asymptotic form for $E_p(R)$ is also sufficient in higher energy elastic scattering, where the absorptive potential will attenuate lower partial waves and, again, only peripheral collisions will contribute to the transfer amplitude.

The integrals $J(R)$ and $\Delta(R)$ can be estimated from DWBA theory. We are mainly concerned with their behavior outside the nuclear surface. Buttle and Goldfarb (Bu66, Bu68) have shown that the neutron wavefunction is very nearly proportional to a spherical Hankel function:

$$\varphi_l(r) = N h_l^{(1)}(i\alpha r) \quad , \qquad \text{III.D.27}$$

where N is a normalization constant and

$$\alpha^2 \equiv 2\mu_n E_B / \hbar^2 \qquad \text{III.D.28}$$

for neutron binding energy, E_B. The integrals $J(R)$ and $\Delta(R)$ have the approximate analytical form:

$$J(R) = \frac{[SN]^2}{\alpha^3} E_B \frac{e^{-\alpha R}}{\alpha R} \quad . \qquad \text{III.D.29}$$

and

$$\Delta(R) \sim J(R)/E_B \quad . \qquad \text{III.D.30}$$

These formulae are only valid when $\Delta(R) \ll 1$.

Helb *et al.* have analyzed their elastic scattering data with the MWFM, where they assume that the R-dependence of $\Delta(R)$ derives from the long-range bound state wavefunctions, while the R-dependence of $J(R)$ is due to the short-range potential, $V(r_1)$. They achieve this by replacing α by $2\alpha/3$ in the equation for $\Delta(R)$. Taking $[SN]=1$, we compare the adiabatic potentials in both even and odd partial waves for $^{12}C+^{13}C$ and $^{13}C+^{13}C$. (See fig. 32.)

Our data are in excellent agreement with those of Helb *et al.*, so their conclusions regarding the MWFM should hold true for our data as well. Their optical potential, however, has a deep real part which gives essentially the same results as the standard model. We have, therefore, re-investigated the $^{13}C+^{13}C$ system with a shallower optical potential. In fig. 33 we compare the theoretical curves obtained for the angular distribution at 8.0 MeV for different values of $[SN]$. We have assumed $[SN]$ to be energy-independent at low energies; this should be a fairly good approximation below the barrier, where the neutron wavefunctions are expected to approach their asymptotic forms.

Unfortunately, the value for the spectroscopic factor as determined from the $^{12}C(d,p)^{13}C$ reaction is energy dependent, as well as being in disagreement with theoretical predictions. There is speculation that this may be due to resonance effects (Sc67). Measurements of S vary from slightly greater than the theoretical value of 0.61 to more than twice that amount. It should, however, be possible to fix the value of S using the $^{12}C+^{13}C$ and $^{13}C+^{13}C$ data, since the spectroscopic factor should be the same in both systems. From previous studies of the $^{12}C+^{13}C$ elastic

scattering, S appears to be in the neighborhood of 0.85 (Bo71, Oe75) (note: Oertzen (Oe70) deduced an incorrect value for S due to an error in his program.) Using $S = 0.85$ along with shallow optical model parameters similar to those chosen earlier, one obtains the theoretical curves in fig. 34 ($^{13}C+^{13}C$ elastic scattering excitation functions) and fig. 35 ($^{13}C+^{13}C$ S-factor). The adiabatic potential, thus, seems to improve the fit to the data in the area of the traditionally persistent discrepancies. The ability of the optical model to describe the angular distributions is especially enhanced.

It is possible that light particle exchange is a widespread source of distortion in heavy ion cross sections, even well below the barrier. Oertzen and Bohlen (Oe75) give a review of the large effects present in the experimental data for such systems as $^{12}C+^{16}O$, $^{16}O+^{18}O$, $^{12}C+^{14}N$, etc. In each case, the success of the molecular wave function method seems to support particle transfer as the mechanism.

It may be worthwhile to re-examine the exchange process $^{12}C(^{12}C,^{8}Be^{*})^{16}O$. (Transfer to the ^{8}Be ground state has a less favorable Q-value.) A calculation by Kozlovsky (Ko70) indicated that this process was a few percent of the total reaction cross section at the barrier, but the steeper energy dependence reduced it to a negligible fraction at low energies. The spectroscopic factors are unknown, but are taken to be unity for the sake of argument. Although careful in other respects, Kozlovsky seems to have ignored the effect of particle identity, and thus, his estimate may be too small by about a factor of two. In addition, Kozlovsky compares his calculations to the extrapolation of Patterson *et al.* (Pa69). This may bias the ratio in three ways. First, the experimental cross sections themselves may be distorted by a factor of two at low

energies by the effects of target thickness and effective energy corrections. Second, alphas from the decay of $^{8}Be^{*}$ could be inadvertently included in the fusion evaporation yields and enhance the cross section. Third, if the resonances are *produced* by the transfer mechanism, then clearly one should compare the DWBA calculation to the "off-resonance" background in the fusion cross section. The combination of these effects, and that of particle identity, could easily enhance the Kozlovsky estimate by a factor of 10, *i.e.* the α-transfer strength may persist at the few percent level well below the barrier. On the basis of this evidence, the question of α-transfer in $^{12}C+^{12}C$ should be reopened.

Appendix A

Detector Efficiency Calibration

Appendix A describes the calibration of the full energy peak (photo-peak) efficiencies of an 80 cm^3 Ge(Li) detector (Princeton Gamma-Tech, Model LCG14ED, Serial No. 909) over the energy range $250 < E_\gamma < 3300$ keV.

The source/detector geometry is given in figure 6. The inventory of absorbing materials between the source (target) and detector crystal is:

0.051 cm	Cu	(Target backing and heat sink)
0.297 cm	SiO_2	(Quartz insulating rods)
0.051 cm	Fe	(Stainless steel target chamber walls)
0.170 cm	Pb	(Absorber)
0.152 cm	Al	(Detector housing)
0.175 cm	Ge	(Dead layer on crystal surface).

Standard radioactive sources were placed at the target position and enough counts were collected to achieve 0.5% statistical errors: small compared to the uncertainty in source strength. Dead time corrections were kept below 5%. These standard sources are listed below, along with their absolute activities (corrected for decay since time of manufacture). The values for the abundances (number of gamma rays per nuclear disintegration) are taken from Atomic and Nuclear Data Tables, **13** (1974) 89 (Bo74). These abundances must be corrected for the summing of two or more members of a cascade. The total detection efficiency, including the

attenuation through the materials listed above, is computed as a function of gamma energy from eqn. II.B.3 and plotted in figure 36. The presence of the lead absorber makes the total efficiency negligible below about 200 keV; thus the summing of low energy gamma rays is small. The largest summing correction is only 15%, and is generally less than 10%. Table A1 lists the calibration sources used, their gamma ray energies, and published values for the abundances. The values in the fourth column are these abundances, corrected for summing. The last column is the absolute source strength at the time of the calibration.

Also listed in Table A1 are the relative intensities for the six strongest transitions in ^{56}Co. Absolutely calibrated sources determine the efficiencies for photopeak energies up to about 1500 keV. The efficiency calibration was extended to higher energies by using ^{56}Co activity ($t_{½}$ = 78.5 d) from high energy proton bombardment of iron. This isotope has a large number of peaks over the range $500 < E_\gamma < 3500$ keV, making this source an attractive one for relative efficiency calibrations. The relative efficiencies for $E_\gamma < 1333$ keV were normalized to the absolute efficiencies. Since the summing corrections are less than 10%, we have not corrected the relative gamma intensities taken from Camp and Meridith (Ca71). The intensity of each gamma ray relative is taken relative to that of the transition at 847 keV.

The absolute photopeak efficiencies are plotted in figure 10. Points are labeled by nuclide, and the errors arise primarily from the source strength uncertainties. The ^{56}Co errors are solely statistical. A conservative estimate of the overall error is approximately the sum in quadrature of the strength uncertainties (~3%) and the reproducibility (~2%), or about ±4%.

Appendix B

Statistical Model Calculation

In contrast to direct reactions the compound nucleus is assumed to live long enough to be thought of as a collection of individual nucleons in thermal equilibrium, *i.e.*, the decay of this state is independent of its formation. From the time-reversal invariance of the evaporation amplitudes, it is possible to express the fusion cross section in terms of the transmission coefficients of the inverse processes.

When the density of compound nuclear discrete states is high enough, the expression for the cross section may be simplified by averaging over a small energy interval. The energy-averaged cross section to go from a particular initial channel, α (spins $\vec{I}_1$ and $\vec{I}_2$), to a particular channel, β, is

$$\sigma_{\alpha\to\beta} = \frac{\pi\lambda\!\!\!^{-}{}_{\alpha}^{2}}{(2I_1+1)(2I_2+1)} \sum_{J^\pi} \frac{(2J+1)\sum_{l,s}[T_\alpha]_{l,s}{}^{J^\pi} \sum_{l',s'}[T_\beta]_{l',s'}{}^{J^\pi}}{T^{J^\pi}} \quad , \text{A.B.1}$$

where

$$T^{J^\pi} \equiv \sum_{\gamma,l,s} [T_\gamma]_{l,s}{}^{J^\pi} \quad .$$

and the sums are performed over values of l and s conserving total angular momentum and parity:

$$\vec{J} = \vec{l} + \vec{s} = \vec{l}' + \vec{s}' \quad ,$$

$$\vec{s} = \vec{I_1} + \vec{I_2} \quad .$$

For a state of intrinsic parity, n, and overall parity, π:

$$(-1)^{s+l+n} = (-1)^{\pi} \quad .$$

The code HAUSER*4 (Ma75, Ma76) was used to evaluate eqn. A.B.1 at discrete energies in the range covered by the data. As an example, the partial cross section for $^{13}C+^{13}C \rightarrow ^{25}Mg^{*} + n$ to go to a particular level in ^{25}Mg of excitation , E^{*}, is converted into a probability distribution,

$$P_{^{25}Mg}(E_{cm}, E^{*}) = \sigma(E_{cm}, E^{*}) \,/\, \int d\varepsilon\, \sigma(E_{cm}, \varepsilon) \quad . \qquad \text{A.B.2}$$

Successive evaporations are more complicated. The cross section of the two stage process:

$$^{13}C+^{13}C \rightarrow ^{25}Mg^{*} + n \rightarrow ^{24}Mg^{*} + n + n$$

is found by inverting the "intermediate" state. The probability of forming $^{24}Mg^{*}$ as a function of $^{25}Mg^{*}$ excitation, spin, and parity was multiplied by the cross section for $^{13}C+^{13}C \rightarrow ^{25}Mg^{*} + n$ and summed over all energetically allowed excitations of ^{25}Mg. The general expression for this is:

$$\sigma_{\alpha\to\beta\to\gamma} = \sum_{J^\pi}\left[\frac{\pi\lambda\!\!\!^{-}{}_{\alpha}^{2}}{(2I_1+1)(2I_2+1)}\sum_{l,s}[T_\alpha]_{l,s}{}^{J^\pi}\right]\times$$

$$\times\left[\frac{\sum_{l',s'}[T_\beta]_{l',s'}{}^{J^\pi}}{T^{J^\pi}{}_{\alpha\to\beta}}\right]\left[\frac{\sum_{l'',s''}[T_\gamma]_{l'',s''}{}^{J^\pi}}{T^{J^\pi}{}_{\beta\to\gamma}}\right] . \qquad \text{A.B.3}$$

These were converted to probability distributions, as before.

The transmission coefficients were computed by specifying the nuclear potentials and level densities of each species, then integrating the Schroedinger equation out from the origin in each partial wave. At some radius, well outside the nucleus, these solutions were matched to the radial Coulomb wavefunctions to give the complex phase shifts, from which:

$$T_l \equiv 1 - |e^{2i\delta_l}|^2 . \qquad \text{A.B.4}$$

The accuracy of the integration-matching procedure (Co10, Fo49) is insufficient for $T_l < 10^{-4}$. When the transmission coefficients approached this value, they were computed directly from the wavefunctions and the imaginary part of the potential:

$$T_l = \int |\psi_l|^2 W(r)\, d^3r . \qquad \text{A.B.5}$$

The T_l's were then summed over excited states. Known properties of these levels were used, whenever possible; usually below 6 or 7 MeV of excitation. Beyond this we integrated over a parametrization of the level

density:

$$T^{J^\pi} = \sum_i T_i^{J^\pi} + \int_{E_1}^{E_2} T(E,J)\,\rho(E,J)\,dE \quad . \qquad \text{A.B.6}$$

The form of $\rho(E,J)$ is that given by Gilbert and Cameron (Gi65), where the parameters have been fitted to the known bound states (Table B1). Above the energy of the highest discrete state used, E_c, the level density is closely approximated by the constant temperature formula:

$$\rho(E) = T^{-1}\exp[\,(E-E_0)/T\,] \quad . \qquad \text{A.B.7}$$

At higher energies, this is joined smoothly to a back-shifted Fermi gas formula. Defining $U \equiv E-\Delta$, where Δ is the correction for shell and pairing effects:

$$\rho = \frac{\sqrt{\pi}}{12}\,\frac{1}{\sqrt{2\pi}\,\sigma}\,\frac{\exp(2\sqrt{aU})}{(aU^5)^{1/4}} \quad . \qquad \text{A.B.8}$$

In this expression, the quantity, σ, is related to the moment of inertia for a spherical nucleus, $M = (2/5)\,m\,(r_0 A^{1/3})^2$, by

$$\sigma^2 = \frac{M}{\hbar^2}(U/a)^{1/2} \quad . \qquad \text{A.B.9}$$

Gilbert and Cameron (Gi65) provide a prescription for joining eqn. A.B.7 with A.B.8 at an energy $U' = 2.5 + 150/A$ MeV. Taking $r_0 = 1.04$ fm, the values of the other parameters are constrained to be:

$$a = U' [1/T + 3/(2U')]^2 \quad , \qquad \text{A.B.10}$$

and

$$\Delta = E_0 - U' + T\left[2\sqrt{aU'} + \ln\left(\frac{0.579T}{A^{5/6}U'^{3/2}}\right)\right] \quad . \qquad \text{A.B.11}$$

The values of these parameters are also given in Table B1 for each channel considered. The spin-dependence of the level distribution was taken to be a gaussian:

$$\rho(E,J^{\pi}) = \rho(E)\rho(J) = \rho(E)\frac{(2J+1)}{2\sigma^2}\exp[-J(J+1)/2\sigma^2] \quad . \qquad \text{A.B.12}$$

Transmission coefficients for protons, neutrons, deuterons, and alphas were computed for potentials of the form:

$$U(r) = -Vf(r,R_r,a_r) - iW_i f(r,R_i,a_i) + 4i a_s W_s (d/dr) f(r,R_s,a_s) \quad , \qquad \text{A.B.13}$$

where $f(r,R_j,a_r) \equiv [1+\exp^{(r-R_j)/a_j}]^{-1}$, $R_j = r_j A^{1/3}$ for $j = r, i$, and s (real, imaginary, and spin-orbit indices, respectively). These parameters are listed in Table B2, and are taken from the compilation of Perey and Perey (Pe76). Of course, the usual centrifugal potential is added. The Coulomb potential is that for a sphere of radius $r_c A^{1/3}$, carrying a uniform volume charge density.

Width fluctuation corrections were not included; their effect on the excited state populations was minimal. Only the ratio of elastic scattering cross sections to fusion cross sections was affected significantly by this.

The summing-branching factor for each photopeak was found by convoluting the excited state distributions with the known γ branching ratios and measured detection efficiencies as described in Section II.B and Appendix A. These correction factors as a function of center-of-mass energy are given in figure 11.

References

Aj76 F. Ajzenberg-Selove, Nucl. Phys. **A268** (1976) 1.

Al56 K. Alder, A. Bohr, T. Huus, B. Mottleson, and A. Winther, Rev. Mod. Phys. **28** (1956) 77.

Al60 E. Almquist, D. A. Bromley, and J. A. Kuehner, Phys. Rev. **4** (1960) 515.

Al63 E. Almquist, D. A. Bromley, J. A. Kuehner, and B. Whalen, Phys. Rev. **130** (1963) 130.

Al64 E. Almquist, J. A. Kuehner, D. McPherson, and E. W. Vogt, Phys. Rev. **136** (1964) 884.

Al79 Y. Alhassid, R. D. Levine, J. S. Karp, and S. G. Steadman, Phys. Rev. **C20** (1979) 1789.

Al80 Y. Alhassid, preprint, Kellogg Radiation Lab. **MAP-13** (1980).

Be56a G. Breit and M. E. Ebel, Phys. Rev. **103** (1956) 679.

Be56b G. Breit and M. E. Ebel, Phys. Rev. **104** (1956) 1030.

Be78 Hans-Werner Becker, Diploma Thesis, Institute für Kernphysik, Münster (1978) unpublished.

Be81a K. G. Bernhardt, H. Bohn, K. A. Eberhard, R. Sielemann, R. Vandenbosch, and M. P. Webb, Nucl. Phys. **A365** (1981) 157.

Be81b Hans-Werner Becker, K. U. Kettner, C. Rolfs, and H. P. Trautvetter, Z. Phys. **A303** (1981) 305.

Bo71 H. G. Bohlen and W. von Oertzen, Phys. Lett. **37B** (1971) 451.

Bo72 H. G. Bohlen, M. Feil, A. Gamp, B. Kohlmeyer, N. Marquardt, and W. von Oertzen, Phys. Lett. **41B** (1972) 425.

Bo74 W. W. Bowman and K. W. MacMurdo, Atomic Data and Nuclear Data Tables **13** (1974) 89.

Bu66 P. J. A. Buttle and L. J. B. Goldfarb, Nucl. Phys. **78** (1966) 409.

Bu68 P. J. A. Buttle and L. J. B. Goldfarb, Nucl. Phys. **A115** (1968) 461.

Ca71 D. C. Camp and G. Meredith, Nucl. Phys. **A166** (1971) 349.

Ca79 J. Gomez del Campo, R. A. Dayras, J. A. Biggerstaff, D. Shapira, A. H. Snell, P. H. Stelson, and R. G. Stokstad, Phys. Rev. Lett. **43** (1979) 26.

Ch70 K. C. Chung, A. Mittler, J. D. Brandenberger, and M. T. McEllistrem, Phys. Rev. **C2** (1970) 139.

Ch76 P. R. Christensen and A. Winther, Phys. Lett. **65B** (1976) 19.

Ch77a P. R. Christensen, Z. E. Switkowski, and R. A. Dayras, Nucl. Phys. **A280** (1977) 189.

Ch77b P. R. Christensen and Z. E. Switkowski, Nucl. Phys. **A280** (1977) 205.

Ch80 M. L. Chatterjee, L. Potvin and B. Čujec, Nucl. Phys. **A333** (1980) 273.

Co10 P. H. Cowell and A. C. D. Commelin, Appendix to Greenwich Observatories for 1909, Edinburgh (1910).

Cu76 B. Čujec and C. A. Barnes, Nucl. Phys. **A266** (1976) 461.

Cu81 B. Čujec, private communication.

Da76a R. A. Dayras, R. G. Stokstad, Z. E. Switkowski, and R. M. Wieland, Nucl. Phys. **A261** (1976) 478.

Da76b R. A. Dayras, R. G. Stokstad, Z. E. Switkowski, and R. M. Wieland, Nucl. Phys. **A265** (1976) 153.

Da82 B. Dasmahapatra, B. Čujec, and F. Lahlou, Nucl. Phys. **A384** (1982) 257.

De81 J.-L. Dethier and F. L. Stancu, Phys. Rev. **C23** (1981) 1503.

De82 P. Descouvemont, D. Baye, and P.-H. Heenen, Z. Phys. **A306** (1982) 79.

Di82 D. E. DiGregorio, J. Gomez del Campo, Y. D. Chan, J. L. C. Ford, Jr., D. Shapira, and M. E. Ortiz, Phys. Rev. **C26** (1982) 1490.

Dr81 D. M. Drake, M. Cates, N. Cindro, D. Pocanic, and E. Holub, Phys. Lett. **98B** (1981) 36.

Er80 K. A. Erb, in *Proc. Int. Conf. on the Resonant Behavior of Heavy Ion Systems*, Athens, Greece, June 23-26, 1980, (G. Vourvopoulos, ed.) 323.

Ev55 Robley D. Evans, *The Atomic Nucleus*, McGraw-Hill, New York (1955) 876.

Fo49 J. Fox and E. T. Goodwin, Proc. Cambridge Phil. Soc. **45** (1949) 373.

Fo75 W. A. Fowler, G. R. Coughlan, and B. A. Zimmerman, Ann. Rev. Astron. Astrophys. **13** (1975) 69.

Fr78 R. M. Freeman and F. Haas, Phys. Rev. Lett. **40** (1978) 927.

Ga49 G. Gamow and C. L. Critchfield, *Theory of the Atomic Nucleus and Nuclear Energy Sources*, Oxford University Press, London (1949) 173.

Gi65 A. Gilbert and A. G. Cameron, Can. J. Phys. **43** (1965) 1446.

Go68 A. Gobbi, U. Matter, J.-L. Perrenoud, and P. Marmier, Nucl Phys. **A112** (1968) 537.

Gr62 K. R. Greider, Phys. Rev. Lett. **9** (1962) 392.

Ha72 M. L. Halbert and K. Nagatani, Bull. Am. Phys. Soc. **17** (1972) 530.

He73 H.-D. Helb, P. Dück, G. Hartmann, G. Ischenko, F. Siller and H. Voit, Nucl. Phys. **A206** (1973) 385.

Hi53 D. L. Hill and J. A. Wheeler, Phys. Rev. **89** (1953) 1102.

Hi77 M. D. High and B. Čujec, Nucl. Phys. **A282** (1977) 181.

Ho65 J. T. Holdeman and R. M. Thaler, Phys. Rev. Lett. **14** (1965) 81.

Ho71 P. E. Hodgson, *Nuclear Reactions and Nuclear Structure*, Clarendon Press, Oxford (1971).

Hu80 G. Hulke, C. Rolfs, and H. P. Trautvetter, Z. Phys. **A297** (1980) 161.

Ja57 E. T. Jaynes, Phys. Rev. **106** (1957) 620.

Ke35 E. C. Kemble, Phys. Rev. **48** (1935) 549.

Ke80 K. U. Kettner, H. Lorenz-Wirzba, and C. Rolfs, Z. Phys. **A298** (1980) 65.

Ko70 B.-Z. Kozlovsky, Astrophys. Space Sci. **8** (1970) 114.

Ko79 D. G. Kovar, D. F. Geesaman, T. H. Braid, Y. Eisen, W. Henning, T. R. Ophel, M. Paul, K. E. Rehm, S. J. Sanders, P. Sperr, J. P. Schiffer, S. L. Tabor, S. Vigdor, B. Zeidman, and F. W. Prosser, Jr., Phys. Rev. **C20** (1979) 1305.

Ko80 D. Konnerth, K. G. Bernhardt, K. A. Eberhard, R. Singh, A. Strzalkowski, W. Trautmann and W. Tombik, Phys. Rev. Lett. **45** (1980) 1154.

Ko81 S. K. Korotky, K. A. Erb, S. J. Willet, and D. A. Bromley, in *Proc. Int. Conf. on Nucl. Phys.*, Berkeley, 1980, (North-Holland, Amsterdam, R. M. Diamond, and J. O. Rasmussen, ed., 1981) 549.

Ma71 M. G. Mazarakis, Ph.D. Thesis, University of Pennsylvania, Philadelphia (1971) unpublished.

Ma73a R. A. Malfliet, S. Landowne, and V. Rostokin, Phys. Lett. **44B** (1973) 238.

Ma73b M. G. Mazarakis and W. E. Stephens, Phys. Rev. **C7** (1973) 1280.

Ma75 F. M. Mann, Ph.D. Thesis, Caltech, Pasadena (1975) unpublished.

Ma76 F. M. Mann, Hanford Engineering Development Laboratory-**TME 76-80, UC-79d** (1976).

Me78 R. A. Meyer, *Multigamma- ray Calibration Sources*, Lawrence Livermore Laboratory **M-100**, Berekeley (1978).

Mi54 E. A. Milne, Phys. Rev. **93** (1954) 762.

Mi72 G. J. Michaud and E. W. Vogt, Phys. Rev. **C5** (1972) 350.

Mi73 G. J. Michaud, Phys. Rev. **C8** (1973) 525.

No70 L. C. Northcliffe and R. F. Schilling, Nuclear Data Tables **A7** (1970) 233.

Oe70 W. von Oertzen, Nucl Phys. **A148** (1970) 529.

Oe73 W. von Oertzen and W. Nörenberg, Nucl Phys. **A207** (1973) 113.

Oe75 W. von Oertzen and H. G. Bohlen, Phys. Rep. **19** (1975) 1.

Ol74 C. Olmer, R. G. Stokstad, D. L. Hanson, K. A. Erb, M. W. Sachs, and D. A. Bromley, Phys. Rev. **C10** (1974) 1722.

Pa69 J. R. Patterson, H. Winkler, and C. S. Zaidins, Ap. J. **157** (1969) 367.

Pa71 J. R. Patterson, B. N. Nagorcka, G. D. Symons, and W. M. Zuk, Nucl. Phys. **A167** (1971) 545.

Pe67 J.-L. Perrenoud and Eric Sheldon, Nucl. Phys. **A102** (1967) 105.

Pe76 C. M. Perey and F. G. Perey, Atomic Data and Nuclear Data Tables **17** (1976) 1.

Ra63 G. H. Rawitscher, Nucl. Phys. **85** (1963) 337.

Re73 W. Reilly, R. Wieland, A. Gobbi, M. W. Sachs, and D. A. Bromley, Nuovo Cimento **A13** (1973) 897.

Sc67 J. P. Schiffer, G. C. Morrison, R. H. Siemssen, and B. Zeidman, Phys. Rev. **164** (1967) 1274.

Si74 R. H. Siemssen, Elastic and Inelastic Scattering of Heavy Ions, in: *Nuclear Spectroscopy* (ed. J. Cerny), Academic Press (1974).

St72 W. E. Stephens, private communication to W. F. Fowler (1972).

St76 R. G. Stokstad, Z. E. Switkowski, R. A. Dayras, and R. M. Wieland, Phys. Rev. Lett. **37** (1976) 888.

St80 R. G. Stokstad, presented at the XIII International Summer School in Nuclear Physics, Mikolajki, Poland, Sept. 1, 1980.

Sw74 Z. E. Switkowski, R. M. Wieland, and A. Winther, Phys. Rev. Lett. **33** (1974) 840.

Sw75 Z. E. Switkowski and R. A. Dayras, Nucl. Instr. and Methods **128** (1975) 9.

Sw76 Z. E. Switkowski, R. G. Stokstad, and R. M. Wieland, Nucl. Phys. **A274** (1976) 202.

Sw77 Z. E. Switkowski, R. G. Stokstad, and R. M. Wieland, Nucl. Phys. **A279** (1977) 502.

Tr80 W. Treu, H. Fröhlich, W. Galster, P. Dück, and H. Voit, Phys. Rev. **C22** (1980) 2462.

Tr83 S. Trentalange, J. L. Osborne, S.-C. Wu, and C. A. Barnes, to be published.

We76 M. P. Webb, R. Vandenbosch, K. A. Eberhard, K. G. Bernhardt, and M. S. Zisman, Phys. Rev. Lett. **36** (1976) 779.

Wo73 C. Y. Wong, Phys. Rev. Lett. **31** (1973) 766.

Wo76 H. Wojciechowski, D. E. Gustafson, L. R. Medsker, and R. H. Davis, Phys. Lett. **63B** (1976) 413.

Wu78 S.-C. Wu, Ph.D. Thesis, Caltech, Pasadena (1978) unpublished.

TABLE 1

$^{13}C+^{13}C$ PARTIAL AND TOTAL FUSION CROSS SECTIONS

Table 1 lists the elemental and total fusion cross sections, as well as the S-factor, which were deduced from the γ-ray measurements described in Section II.B. These data are plotted in figures 12, 13, 14, and 20.

Exit channels are labeled by heavy residual nucleus. Cross sections are obtained by multiplying by 10^x, where x is given in parentheses. The error quoted for the total cross section reflects counting statistics only. The systematic error is estimated to be ±15%. It is the sum (in quadrature) of uncertainties of ±10% in the summing-branching factors, ±4% in target thickness, ±5% in beam integration and ±4% in Ge(Li) efficiency.

TABLE 1

$^{13}C+^{13}C$ Partial and Total Fusion Cross Sections

$E_{c.m.}$ (MeV)	Partial Cross Sections [a] (barns)						σ_{Fus} (b)	S(E) (MeV-b)	Error (%)
	^{24}Mg	^{24}Na	^{21}Ne	^{25}Mg	^{22}Ne	^{18}O			
3.264	1.65(-6)		1.54(-7)	2.30(-6)			4.35(-6)	9.70(16)	35
3.364	5.56		2.37	1.26			6.47	7.00	27
3.464	6.70	0.86(-6)	4.96	0.17	1.49(-6)		9.71	5.26	14
3.565	1.17(-5)	1.33	1.52(-6)	4.34	3.99		2.29(-5)	6.40	11
3.665	2.45	2.13	5.33	4.99	6.54		4.35	6.44	7
3.765	3.80	4.68	6.59	1.09(-5)	1.03(-5)		7.04	5.67	4.9
3.865	6.13	7.16	1.63(-5)	1.62	1.58		1.17(-4)	5.25	2.2
3.918	7.43	1.22(-5)	2.52	1.77	1.89		1.48	4.95	
3.968	1.02(-4)	0.96	2.06	2.58	2.21		1.80	4.56	5.5
4.018	1.40	1.64	2.52	3.90	2.87		2.49	4.79	<3
4.068	1.73	2.10	4.67	3.44	4.12		3.16	4.66	
4.118	2.07	2.65	4.34	4.81	4.28		3.68	4.17	
4.168	2.78	3.17	1.04(-4)	3.46	5.86		5.07	4.43	
4.218	3.62	5.39	1.06	7.25	7.62		6.71	4.56	
4.268	4.51	6.25	1.38	1.14(-4)	1.05(-4)		8.70	4.61	
4.318	5.53	7.74	1.71	1.09	1.08		1.02(-3)	4.23	
4.368	6.42	1.11(-4)	2.14	1.57	1.61		1.28	4.20	
4.419	7.72	1.31	2.84	1.70	1.66		1.52	3.94	
4.466	9.59	1.85	3.73	2.17	1.93		1.93	3.99	
4.519	1.15(-3)	2.18	4.40	2.75	2.65		2.35	3.83	
4.569	1.42	2.62	5.13	2.89	2.72		2.75	3.59	
4.619	1.59	3.28	5.90	3.37	3.42		3.19	3.33	
4.669	1.96	3.83	7.52	4.42	3.78		3.92	3.30	
4.719	2.34	4.84	8.84	5.12	4.71		4.70	3.20	
4.769	2.81	6.26	1.06(-3)	5.87	5.82		5.66	3.13	
4.819	3.35	7.10	1.32	7.12	6.61		6.75	3.03	
4.869	3.95	8.92	1.54	8.65	7.64		8.01	2.94	
4.920	4.61	1.10(-3)	1.83	1.02(-3)	8.50		9.40	2.82	
4.967	5.11	1.30	2.16	1.00	9.78		1.05(-2)	2.62	
5.02	5.99	1.46	2.49	1.23	1.17(-3)		1.25	2.53	
5.07	7.14	1.71	3.02	1.57	1.27		1.49	2.49	
5.12	8.18	1.90	3.24	1.50	1.40		1.64	2.28	
5.22	1.03(-2)	2.63	4.36	2.16	1.88		2.18	2.10	
5.27	1.17	3.02	4.69	2.35	2.08		2.44	1.96	
5.32	1.30	3.53	5.51	2.43	2.28		2.73	1.84	
5.37	1.48	3.99	6.15	2.98	2.63		3.11	1.76	
5.42	1.66	4.43	6.99	3.23	3.01		3.49	1.66	
5.47	1.78	5.11	7.83	3.33	3.22		3.80	1.54	
5.52	2.03	5.57	8.64	3.82	3.48		4.31	1.46	
5.57	2.23	6.42	9.82	4.09	3.82		4.79	1.38	
5.62	2.48	7.34	1.10(-2)	4.14	4.36		5.32	1.30	
5.67	2.71	8.32	1.23	4.89	4.78		5.91	1.23	
5.72	2.92	9.28	1.31	5.20	4.78		6.34	1.13	
5.77	3.30	1.07(-2)	1.44	5.90	5.65		7.18	1.10	
5.82	3.53	1.19	1.64	5.99	5.90		7.79	1.02	

TABLE 1 (continued)

$^{13}C+^{13}C$ Partial and Total Fusion Cross Sections

$E_{c.m.}$ (MeV)	Partial Cross Sections [a] (barns)						σ_{Fus} (b)	S(E) (MeV-b)	Error (%)
	^{24}Mg	^{24}Na	^{21}Ne	^{25}Mg	^{22}Ne	^{18}O			
5.87	3.77(-2)	1.33(-2)	1.78(-2)	6.92(-3)	6.17(-3)		8.43(-2)	9.43(15)	<2.5
5.92	4.13	1.43	1.88	7.31	6.42		9.08	8.74	
5.97	4.26	1.61	2.04	7.48	6.64		9.60	8.02	
6.07	4.65	1.73	2.27	8.13	7.54		1.06(-1)	6.60	
6.12	5.05	1.93	2.41	9.77	7.30		1.16	6.21	
6.17	5.35	2.06	2.53	8.73	8.27		1.21	5.66	
6.27	5.89	2.34	2.88	9.03	9.31		1.35	4.77	
6.37	6.42	2.67	3.16	1.05(-2)	1.01(-2)		1.49	4.03	
6.47	7.35	3.19	3.68	1.22	1.15		1.73	3.60	
6.57	7.78	3.29	3.86	1.30	1.19	1.02(-2)	1.84	2.95	
6.67	8.28	3.55	4.21	1.52	1.18	1.06	1.98	2.46	
6.77	9.26	4.05	4.78	1.62	1.33	1.39	2.24	2.18	
6.87	9.57	4.28	4.97	1.43	1.35	1.16	2.28	1.74	
6.97	1.04(-1)	5.04	5.67	1.60	1.55	1.16	2.54	1.54	
7.07	1.11	5.32	6.09	1.98	1.66	1.33	2.75	1.32	
7.18	1.18	5.54	6.49	1.91	1.73	1.19	2.86	1.10	
7.28	1.25	6.01	6.92	1.97	1.71	1.31	3.04	9.33(14)	
7.38	1.30	6.51	7.41	1.98	1.73	1.22	3.18	7.86	
7.48	1.32	7.19	7.90	2.25	1.75	1.41	3.37	6.76	
7.58	1.37	7.14	7.94	2.25	1.82	1.31	3.42	5.54	
7.68	1.41	7.73	8.45	2.50	1.81	1.37	3.60	4.77	
7.78	1.46	8.08	8.72	2.26	1.87	1.46	3.70	4.01	
7.88	1.53	8.58	9.39	2.53	1.96	1.53	3.93	3.51	
7.98	1.57	9.39	9.91	2.75	2.11	1.87	4.17	3.08	

[a]) Exit channels are labeled by heavy residual nuclei. Cross sections are obtained by multiplying by 10^x, where x is given in parentheses.

TABLE 2

ELASTIC SCATTERING DATA: EXCITATION FUNCTIONS

Table 2 gives the ratio of the measured $^{13}C+^{13}C$ differential elastic scattering cross section to the Mott cross section in the center of mass as a function of energy for $\vartheta_{c.m.} = 60°$, 70°, 80°, and 90°. These data are plotted in figure 18.

TABLE 2

Elastic Scattering Data: Excitation Functions

$\vartheta_{c.m.} = 60°$

$E_{c.m.}$ (MeV)	$R(E,\vartheta)$	Error	$E_{c.m.}$ (MeV)	$R(E,\vartheta)$	Error
4.464	0.964	0.010	6.594	1.124	0.018
4.590	1.016	0.012	6.719	1.151	0.019
4.715	1.055	0.014	6.844	1.096	0.018
4.840	1.009	0.014	6.969	1.115	0.016
4.965	0.992	0.014	7.220	1.056	0.013
5.091	0.983	0.015	7.470	0.950	0.013
5.216	1.104	0.015	7.721	0.865	0.016
5.342	1.051	0.016	7.971	0.799	0.015
5.466	1.066	0.017	4.464	0.981	0.011
5.592	1.083	0.017	4.464	1.008	0.014
5.717	1.138	0.018	4.715	0.956	0.015
5.842	1.113	0.018	4.965	1.036	0.018
5.967	1.122	0.017	6.969	0.993	0.021
6.093	1.150	0.017	7.470	0.939	0.031
6.218	1.170	0.018	7.971	0.736	0.017
6.343	1.175	0.018	8.222	0.708	0.014
6.468	1.126	0.015	8.472	0.597	0.013

$\vartheta_{c.m.} = 70°$

$E_{c.m.}$ (MeV)	$R(E,\vartheta)$	Error	$E_{c.m.}$ (MeV)	$R(E,\vartheta)$	Error
4.446	0.985	0.016	6.202	0.935	0.016
4.571	1.024	0.017	6.328	0.912	0.017
4.697	0.997	0.016	6.453	0.885	0.018
4.823	1.007	0.017	6.578	0.847	0.018
4.949	1.026	0.020	6.704	0.782	0.015
5.074	1.029	0.016	6.829	0.793	0.013
5.199	0.979	0.013	6.955	0.774	0.013
5.324	0.999	0.017	7.205	0.674	0.013
5.450	0.979	0.015	7.456	0.628	0.010
5.575	0.975	0.015	7.707	0.533	0.009
5.700	0.976	0.014	7.958	0.463	0.008
5.826	0.983	0.010	8.208	0.397	0.006
5.951	0.960	0.022	8.460	0.350	0.005
6.077	0.911	0.015			

TABLE 2 (continued)

Elastic Scattering Data: Excitation Functions

$\vartheta_{c.m.} = 80°$

$E_{c.m.}$ (MeV)	$R(E,\vartheta)$	Error	$E_{c.m.}$ (MeV)	$R(E,\vartheta)$	Error
4.446	0.979	0.018	6.077	0.918	0.019
4.571	0.981	0.018	6.202	0.920	0.022
4.697	1.043	0.020	6.328	0.895	0.022
4.823	1.030	0.016	6.453	0.897	0.023
4.949	0.967	0.016	6.578	0.771	0.017
5.074	1.008	0.013	6.704	0.753	0.018
5.199	0.985	0.016	6.829	0.720	0.017
5.324	0.992	0.023	6.955	0.686	0.018
5.450	1.027	0.021	7.205	0.599	0.014
5.450	0.988	0.015	7.456	0.522	0.012
5.575	0.996	0.017	7.707	0.447	0.011
5.700	0.987	0.017	7.958	0.387	0.009
5.826	0.967	0.018	8.208	0.350	0.008
5.951	0.933	0.019	8.460	0.244	0.009

$\vartheta_{c.m.} = 90°$

$E_{c.m.}$ (MeV)	$R(E,\vartheta)$	Error	$E_{c.m.}$ (MeV)	$R(E,\vartheta)$	Error
3.432	0.976	0.018	6.695	0.602	0.012
3.683	0.994	0.020	6.821	0.559	0.012
3.933	1.027	0.021	6.946	0.500	0.022
4.059	1.077	0.022	7.071	0.454	0.015
4.185	0.945	0.021	4.561	1.005	0.021
4.310	1.045	0.027	4.686	1.016	0.021
4.434	0.980	0.022	4.185	1.033	0.026
4.561	1.011	0.027	4.434	1.007	0.026
4.686	0.938	0.022	4.434	0.956	0.023
4.812	1.000	0.022	4.434	0.980	0.024
4.938	0.993	0.023	6.444	0.730	0.024
5.063	1.039	0.023	6.695	0.587	0.029
5.184	0.994	0.023	7.247	0.347	0.015
5.315	1.033	0.024	7.448	0.321	0.012
5.440	0.953	0.024	7.573	0.256	0.014
5.566	1.006	0.025	7.698	0.232	0.014
5.691	0.937	0.023	7.824	0.223	0.014
5.816	0.984	0.024	7.949	0.186	0.011
5.942	0.908	0.021	8.074	0.175	0.012
6.193	0.857	0.021	8.200	0.129	0.009
6.319	0.817	0.020	8.325	0.144	0.011
6.444	0.721	0.018	8.451	0.121	0.008
6.569	0.713	0.018			

TABLE 3

ELASTIC SCATTERING: ANGULAR DISTRIBUTIONS

Table 3 gives the measured $^{13}C+^{13}C$ differential elastic scattering cross section in the center of mass as a function of angle for $E_{c.m.} = 6.946$ MeV and 7.956 MeV. These points are plotted in figure 19.

TABLE 3

Elastic Scattering Data: Angular Distributions

$E_{c.m.}$ = 6.946 MeV			$E_{c.m.}$ = 7.956 MeV		
$\vartheta_{c.m.}$ (deg.)	$(d\sigma/d\Omega)_{el}$ (b/sr)	Error (b/sr)	$\vartheta_{c.m.}$ (deg.)	$(d\sigma/d\Omega)_{el}$ (b/sr)	Error (b/sr)
31.	7.113	0.111	23.	15.37	0.28
35.	4.691	0.081	27.	8.796	0.16
39.	2.953	0.062	31.	4.940	0.10
43.	2.249	0.041	35.	3.045	0.070
48.	1.376	0.051	39.	2.131	0.049
51.	1.088	0.024	43.	1.621	0.036
52.	1.002	0.025	47.	1.029	0.022
56.	0.6802	0.0188	51.	0.688	0.014
60.	0.4562	0.0189	55.	0.435	0.010
64.	0.3888	0.0117	59.	0.304	0.007
68.	0.3695	0.0101	63.	0.247	0.006
71.	0.3792	0.0091	67.	0.204	0.005
72.	0.3586	0.0088	71.	0.188	0.005
76.	0.2656	0.0076	75.	0.161	0.005
79.	0.2256	0.0068	79.	0.110	0.004
80.	0.1921	0.0063	83.	0.058	0.003
84.	0.1168	0.0054	85.	0.034	0.002
85.	0.1251	0.0057	89.	0.019	0.001
88.	0.0662	0.0045	91.	0.022	0.002
89.	0.0727	0.0047	95.	0.048	0.002
90.	0.0674	0.0047	97.	0.070	0.003
92.	0.0751	0.0048	99.	0.090	0.003
96.	0.1080	0.0052			
100.	0.1869	0.0059			
102.	0.2058	0.0060			

TABLE A1

ABSOLUTE GAMMA RAY ABUNDANCES

Table A1 provides relevant data on the radioactive sources used in the efficiency calibration of the Ge(Li) detector. Next to each nuclide are listed the γ transitions used in the calibration. The third column gives the reported abundances (Bo74), while the fourth column has been summing-corrected for our source/detector geometry. The absolute efficiencies are plotted in figure 10. The efficiency determination is discussed in more detail in Section II.B.4 and Appendix A.

TABLE A1

Absolute Gamma Ray Abundances

Source	E_γ(keV)	Measured	Sum-Corrected	Strength (dis/sec)
^{22}Na	511	1.811	1.685	1.01×10^4 (±4.7%)
	1274	0.999	0.870	
^{60}Co	1173	0.999	0.931	2.03×10^4 (±2.1%)
	1333	1.000	0.929	
^{133}Ba	276	0.075	0.075	8.07×10^4 (±3.3%)
	303	0.196	0.196	
	356	0.670	0.670	
	384	0.094	0.094	
^{137}Cs	661	0.851	0.851	3.70×10^4 (±6.2%)
^{56}Co	847	1.000	1.000	$I_{rel}(847) \equiv 1.000$
	1038	0.140	0.140	
	1238	0.676	0.676	
	1771	0.157	0.157	
	2035	0.079	0.079	
	2598	0.169	0.169	
	3253	0.074	0.074	

TABLE B1

LEVEL DENSITY PARAMETERS

The level density of excited states for each residual nucleus is required by the Hauser-Feshbach statistical model calculation. Parameters T and E_0 were determined by a least-squares fit of the constant temperature formula (eqn. A.B.7) to the level density at low excitation. The high energy form of the level density is a back-shifted Fermi gas formula (eqn. A.B.8) whose parameters, a and Δ, are fixed by smoothly joining to the constant temperature form at energy, U'. Finally, below excitation, E_c, the properties of the discrete states were used. Further details of the statistical model calculation are given in Appendix B.

TABLE B1

Level Density Parameters

Nucleus	T(MeV)	E_0(MeV)	U'(MeV)	a(MeV^{-1})	Δ(MeV)	E_c(MeV)
^{13}C	3.366	1.110	14.04	2.291	6.959	9.897
^{18}O	1.975	2.032	10.83	4.506	7.240	8.122
^{21}Ne	1.714	0.648	9.64	5.266	5.247	6.747
^{22}Ne	1.874	1.510	9.32	4.496	5.502	7.423
^{24}Mg	2.416	1.839	8.75	2.997	4.388	9.515
^{24}Na	2.712	-5.014	8.75	2.553	-2.910	4.048
^{25}Mg	2.407	-2.038	8.50	2.979	0.299	6.168
^{25}Na	1.995	-0.989	8.50	3.905	2.029	2.914

TABLE B2

OPTICAL POTENTIAL PARAMETERS

Optical potential parameters for light particle absorption by heavier nuclei are used as input to the statistical model code HAUSER*4 (Ma75, Ma76). These potentials are used to calculate transmission functions for the inverse process: particle evaporation. Further details are given in Appendix B.

TABLE B2

Optical Model Parameters

Neutrons:

$$V = 47.01 - 0.267E - 0.0018E^2$$
$$r_r = r_c = 1.322 - 7.6A\times10^{-4} + 4A^2\times10^{-6} - 8A^3\times10^{-9}$$
$$a_r = 0.66$$
$$W_s = 9.52 - 0.053E$$
$$r_s = 1.266 - 3.7A\times10^{-4} + 2A^2\times10^{-6} - 4A^3\times10^{-9}$$
$$a_s = 0.48$$

Protons:

$$V = 53.3 - 0.55E + 27.0(N-Z)/A + 0.4(Z/A^{1/3})$$
$$r_r = r_c = r_s = 1.25$$
$$a_r = 0.65$$
$$W_s = 13.5$$
$$a_s = 0.47$$

Deuterons:

$$V = 81.0 - 0.22E + 2.0(Z/A^{1/3})$$
$$r_r = r_c = 1.15$$
$$a_r = 0.81$$
$$W = 14.4 + 0.24E$$
$$r_i = 1.34$$
$$a_i = 0.68$$

Alphas:

$$V = 185.0$$
$$r_r = r_c = r_i = 1.40$$
$$a_r = a_i = 0.52$$
$$W = 25.0$$

$^{13}C+^{13}C$:

$$V = 100.0$$
$$r_r = r_c = r_i = 2.488$$
$$a_r = a_i = 0.50$$
$$W = 18.0$$

The Optical Potential is of the form:

$$U(r) = -Vf(r, R_r, a_r) - iW_i f(r, R_i, a_i) + 4i a_s W_s (d/dr) f(r, R_s, a_s) \quad ,$$

where $f(r, R_j, a_r) \equiv [1 + \exp(r - R_j)/a_j]^{-1}$, $R_j = r_j A^{1/3}$ for $j = r, i,$ and s (real, imaginary, and spin-orbit indices, respectively). These parameters are taken from the compilation of Perey and Perey ((Pe76). The usual form for the centrifugal potential is added. The Coulomb potential is that for a uniformly charged sphere of radius $r_c A^{1/3}$.

FIGURE 1

HEAVY ION FUSION AND TOTAL REACTION CROSS SECTIONS

The heavy ion fusion and total reaction cross sections *vs.* 1/E are given schematically in figure 1. At low energies (region I), the fusion cross section dominates the reaction cross section. Its functional form is governed by barrier penetration. At higher energies (region II), σ_{Fus} decreases due to competition from direct reactions. At very high energies (region III), the liquid drop limit of the compound nucleus is reached and the fusion cross section drops off proportionally to 1/E.

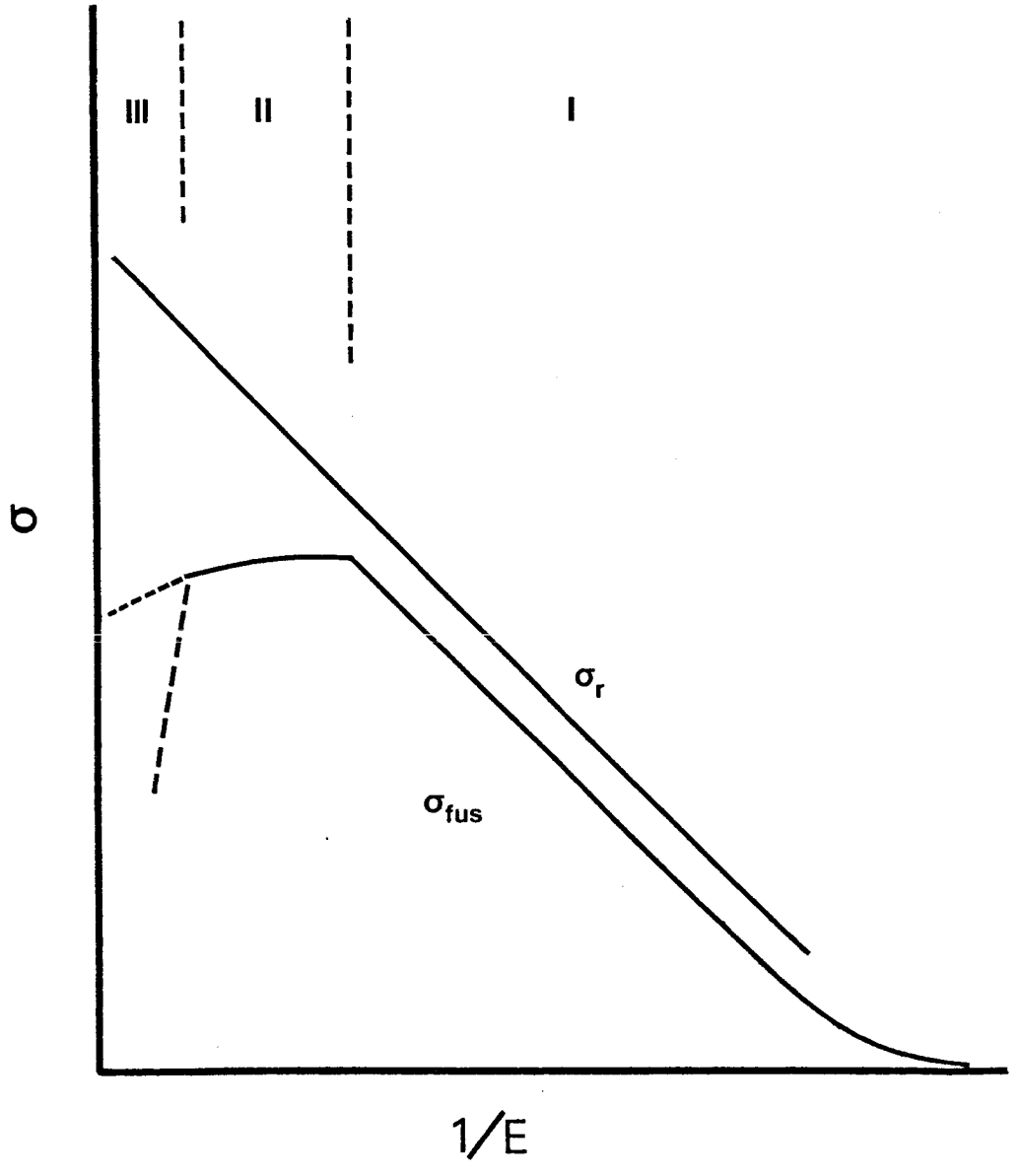
III
II
I
σ
σr
σfus
1/E

FIGURE 2

POPULATION OF NUCLEAR EXCITED STATES

The excited states of heavy residual nuclei are populated by light particle emission. The curves in this figure were generated for the sequential evaporation:

$$^{26}Mg^{*}(32.463\ MeV) \rightarrow \alpha + {}^{22}Ne^{*} \rightarrow \alpha + \alpha + {}^{18}O^{*} \quad .$$

The dotted curves are the excited state distributions corresponding to maximum entropy under conservation of energy and momentum. These are not identical to the density of nuclear excited states (solid curves) because they take into account the density of two-body final states in the relative motion of the heavy and light particles.

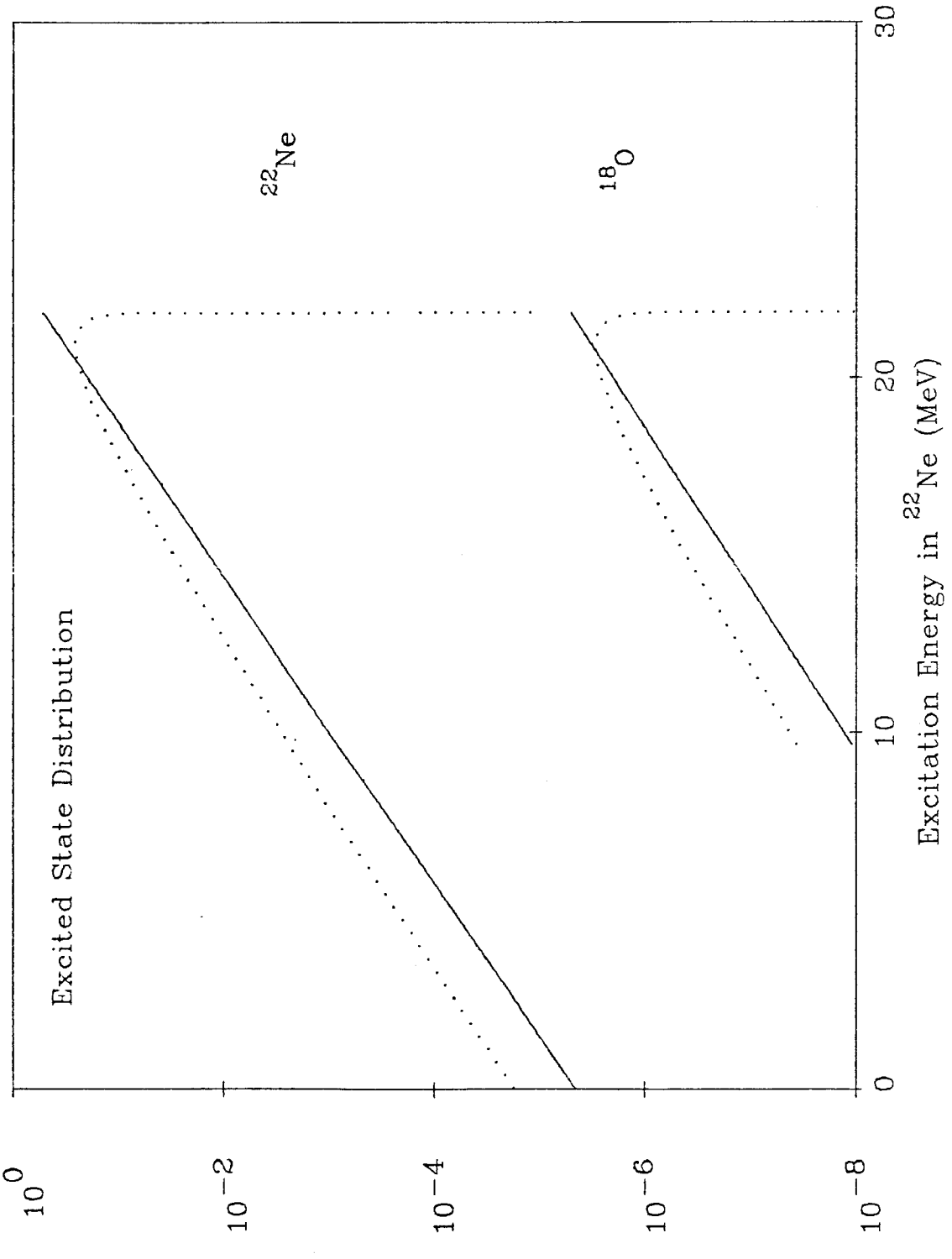
Excited State Distribution
^{22}Ne
^{18}O
10^{0}
10^{-2}
10^{-4}
10^{-6}
10^{-8}
0
10
20
30
Excitation Energy in ^{22}Ne (MeV)

FIGURE 3

ANGULAR DISTRIBUTIONS FOR $^{15}N+^{12}C$ REACTION PRODUCTS

Angular distributions for the partial and total fusion yields are shown for the $^{15}N+^{12}C$ system. This figure is reproduced from Kovar *et al.* (Ko79). These distributions are strongly peaked by kinematics in the forward direction. The degree of dispersion depends on the light particle evaporation process. Generally, the lighter the residual nucleus, the greater the angular dispersion.

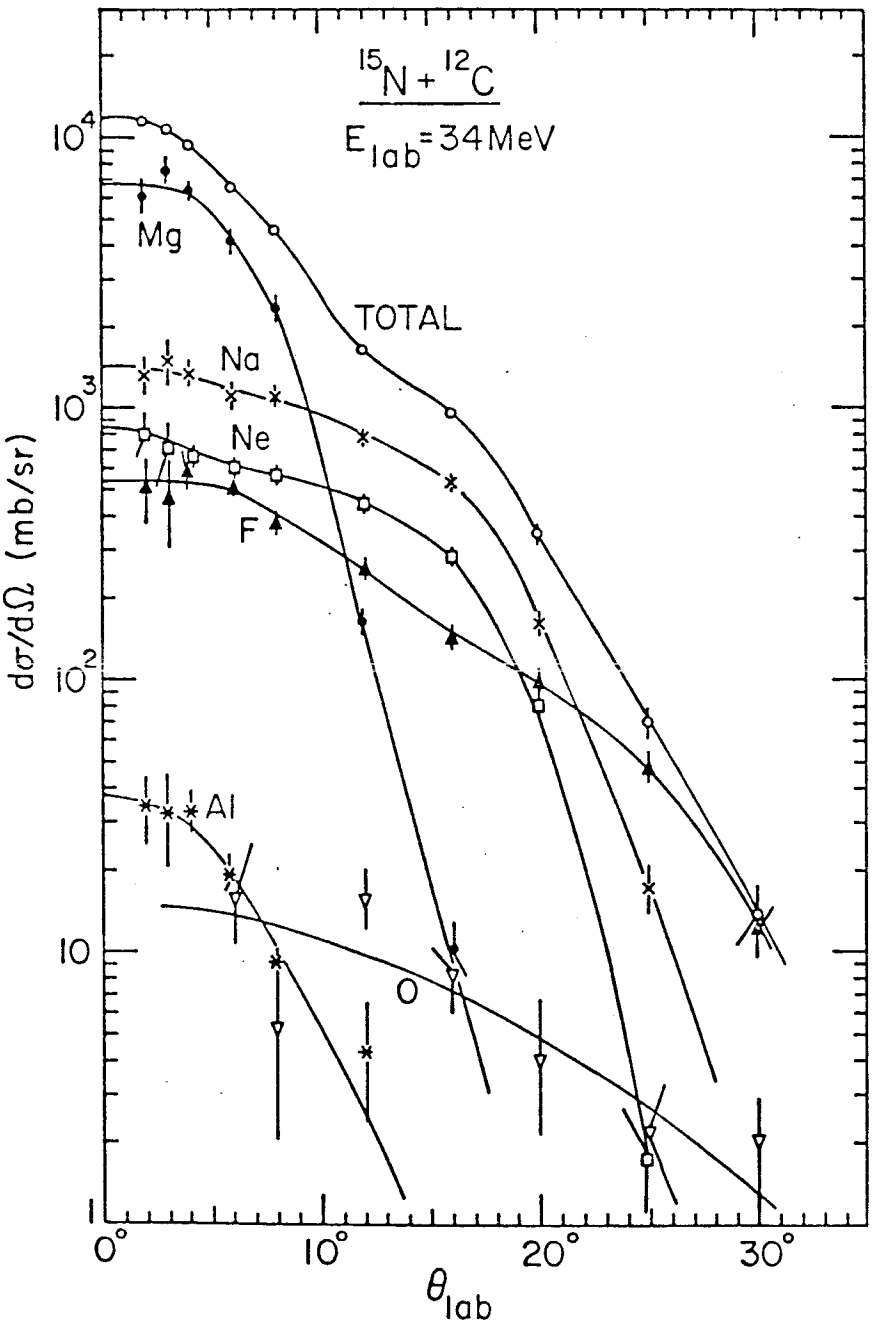
$^{15}N + ^{12}C$
E_{lab}=34MeV
Mg
TOTAL
Na
Ne
F
Al
O
10^4
10^3
10^2
10
1
$d\sigma/d\Omega$ (mb/sr)
0°
10°
20°
30°
θ_{lab}

FIGURE 4

SURPRISAL ANALYSIS OF HEAVY ION REACTIONS

The distribution of the final excitation energy in the $^{232}Th(^{16}O,^{12}C)^{236}U$ channel (bottom panel) and its surprisal (top panel-points) are given as a function of the excitation energy, E^*. This figure is taken from Alhassid *et al.* (Al79). The ordinate of the bottom graph shows the number of counts per channel. The surprisal of these experimental results (points) is well approximated by a straight line; an exactly linear surprisal produces the continuous curve shown along with the data.

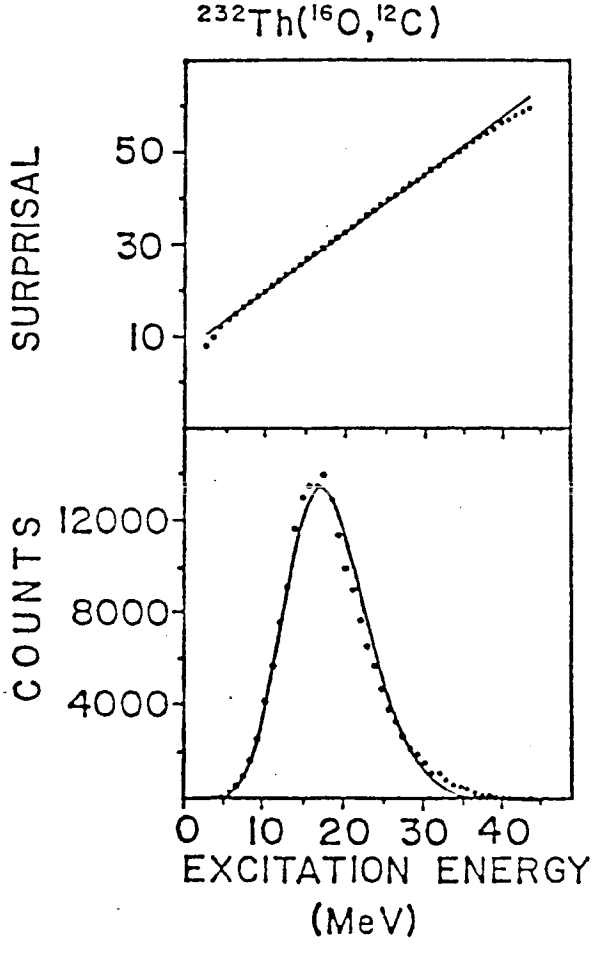
232Th(16O,12C)
SURPRISAL
50
30
10
COUNTS
12000
8000
4000
0
10
20
30
40
EXCITATION ENERGY
(MeV)

FIGURE 5

RATIO OF OPTICAL MODEL TO MOTT CROSS SECTION

The oscillating curve in this log-log plot is the ratio of an optical model cross section to the Mott elastic differential scattering cross section. Note that although the amplitude of the "ringing" increases with decreasing angle, the exponential decrease in the angular interval rapidly diminishes the importance of small angle contributions to the sum-of-differences integral, I.C.5.

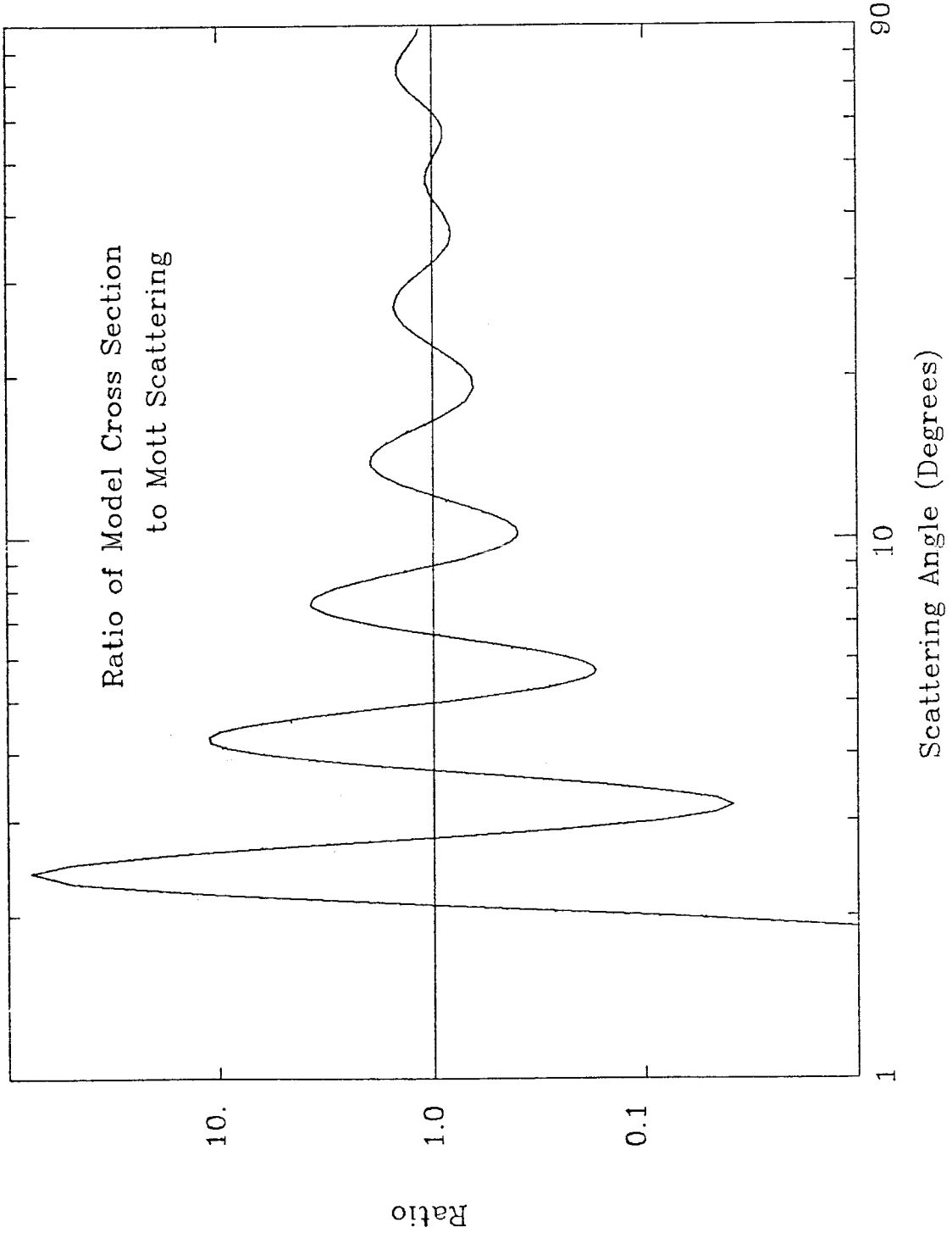
Ratio of Model Cross Section
to Mott Scattering
10.
1.0
0.1
Ratio
1
10
90
Scattering Angle (Degrees)

FIGURE 6

EXPERIMENTAL APPARATUS

The detector, target, and ultra-high vacuum target chamber used to measure the fusion cross section were set up on the South 20° beamline of the ONR-Caltech EN tandem. The experimental apparatus used to measure the fusion cross section is described more fully in Section II.B and Appendix A.

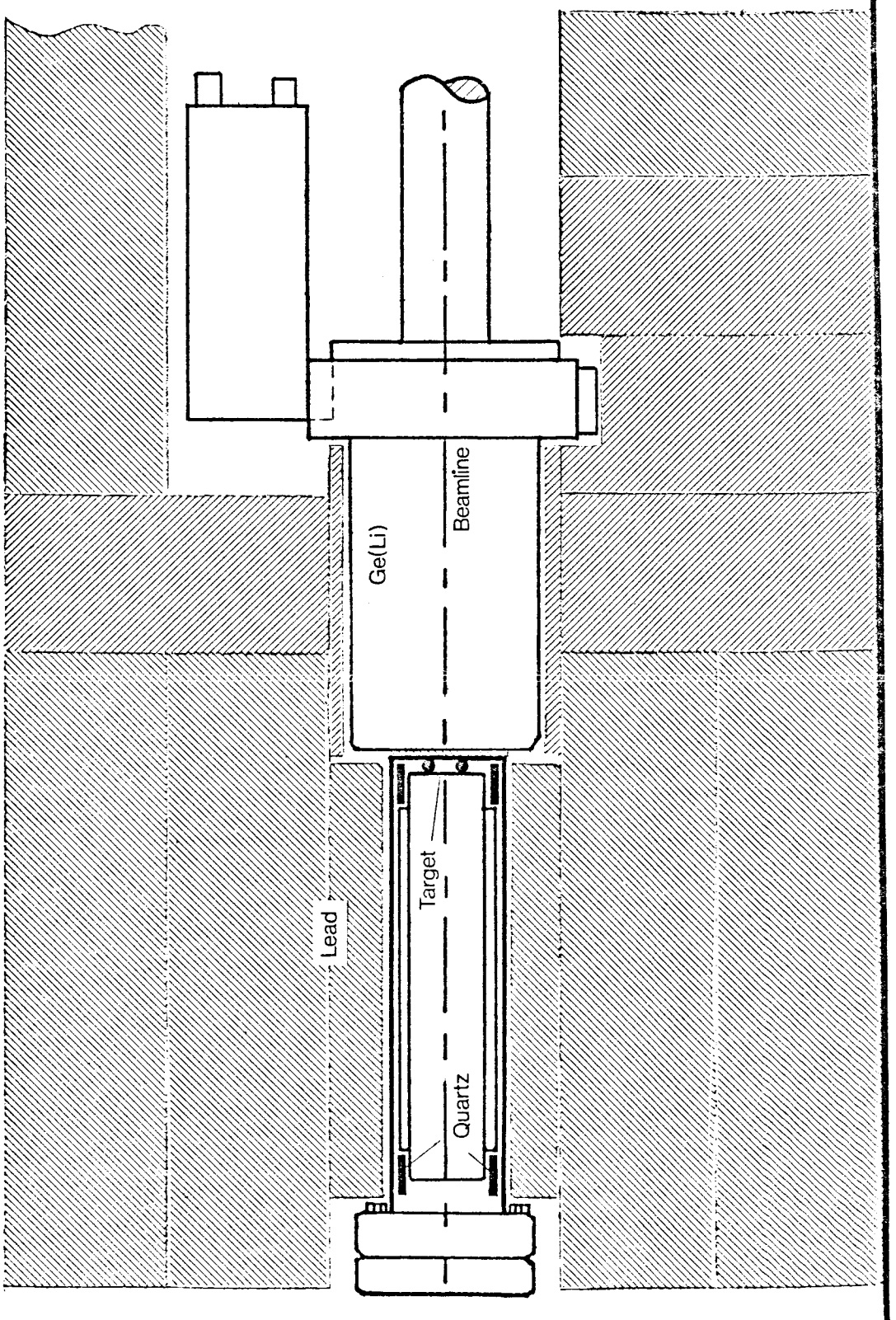
Ge(Li)
Beamline
Target
Lead
Quartz

FIGURE 7

ENERGY LEVEL DIAGRAM FOR THE $^{13}C+^{13}C$ SYSTEM

The observed transitions and reaction Q-values are indicated for each residual nucleus. The shaded region of excitation energy in the compound nucleus ^{26}Mg corresponds to the range of energies covered by the fusion measurements.

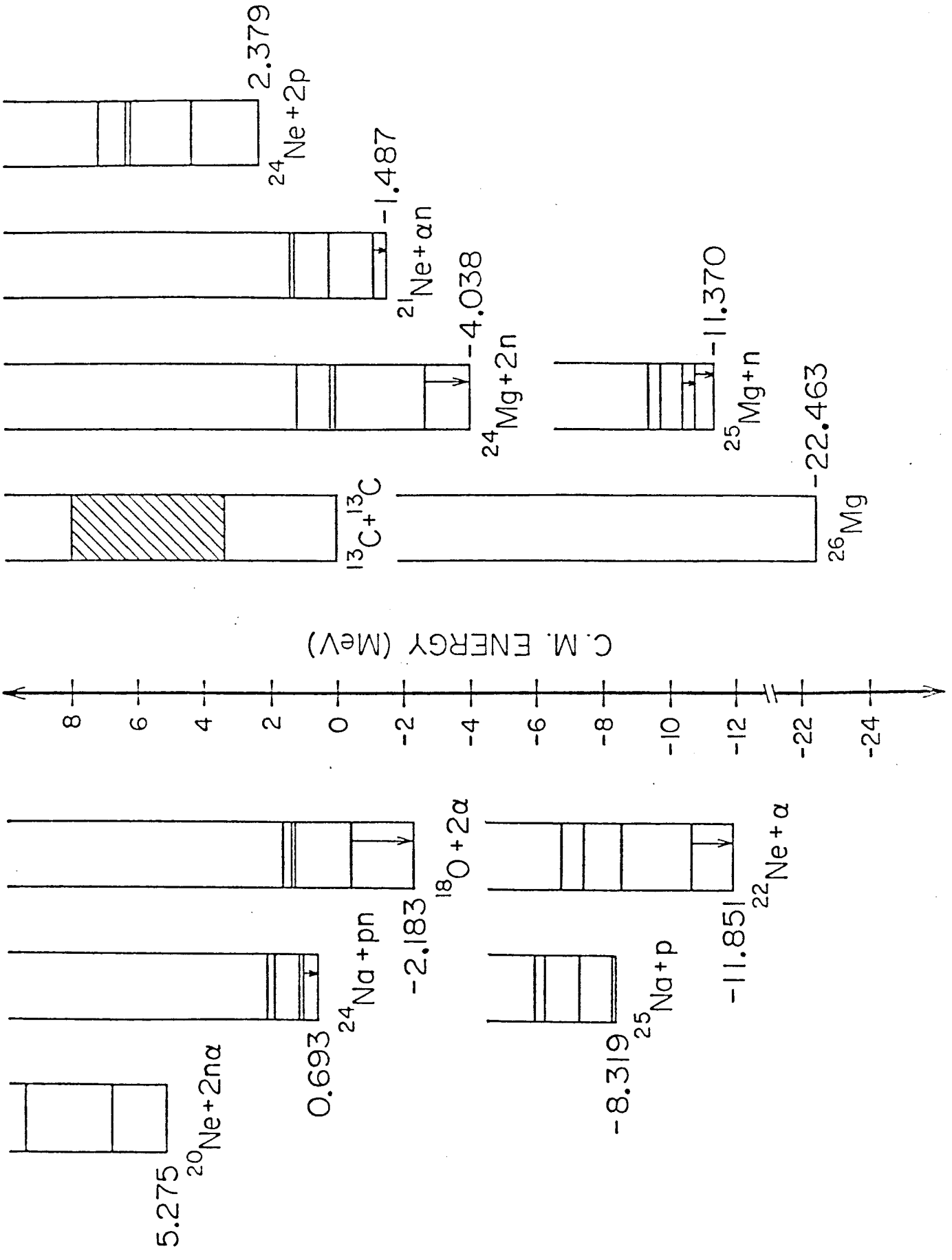
2.379
^{24}Ne+2p
-1.487
^{21}Ne+αn
-4.038
^{24}Mg+2n
-11.370
^{25}Mg+n
-22.463
^{26}Mg
^{13}C+^{13}C
C.M. ENERGY (MeV)
8
6
4
2
0
-2
-4
-6
-8
-10
-12
-22
-24
5.275
^{20}Ne+2nα
0.693
^{24}Na+pn
-2.183
^{18}O+2α
-8.319
^{25}Na+p
-11.851
^{22}Ne+α

FIGURE 8

SAMPLE GE(LI) SPECTRA: PROMPT ACTIVITY

Sample Ge(Li) spectra are given for 14.0 MeV ^{13}C on ^{13}C-enriched (upper spectrum) and reactor grade graphite (lower spectrum) targets. The data were taken as 4096 channel spectra; however, only the first 2500 channels are displayed. The labeled γ-rays are a:^{21}Ne(350.5 keV), b:^{25}Mg(390), c:^{24}Na(472), d:^{25}Mg(585), e:^{22}Ne (1274), f:^{24}Mg(1369), and h:^{18}O(1982). Some of the gamma rays, such as g:^{20}Ne(1634), arise from the ^{12}C content of the enriched target and are considerably weaker in the upper spectrum. Note the strong 0° doppler broadening of the peaks, especially at high energies, and the large number of lines produced by neutron reactions.

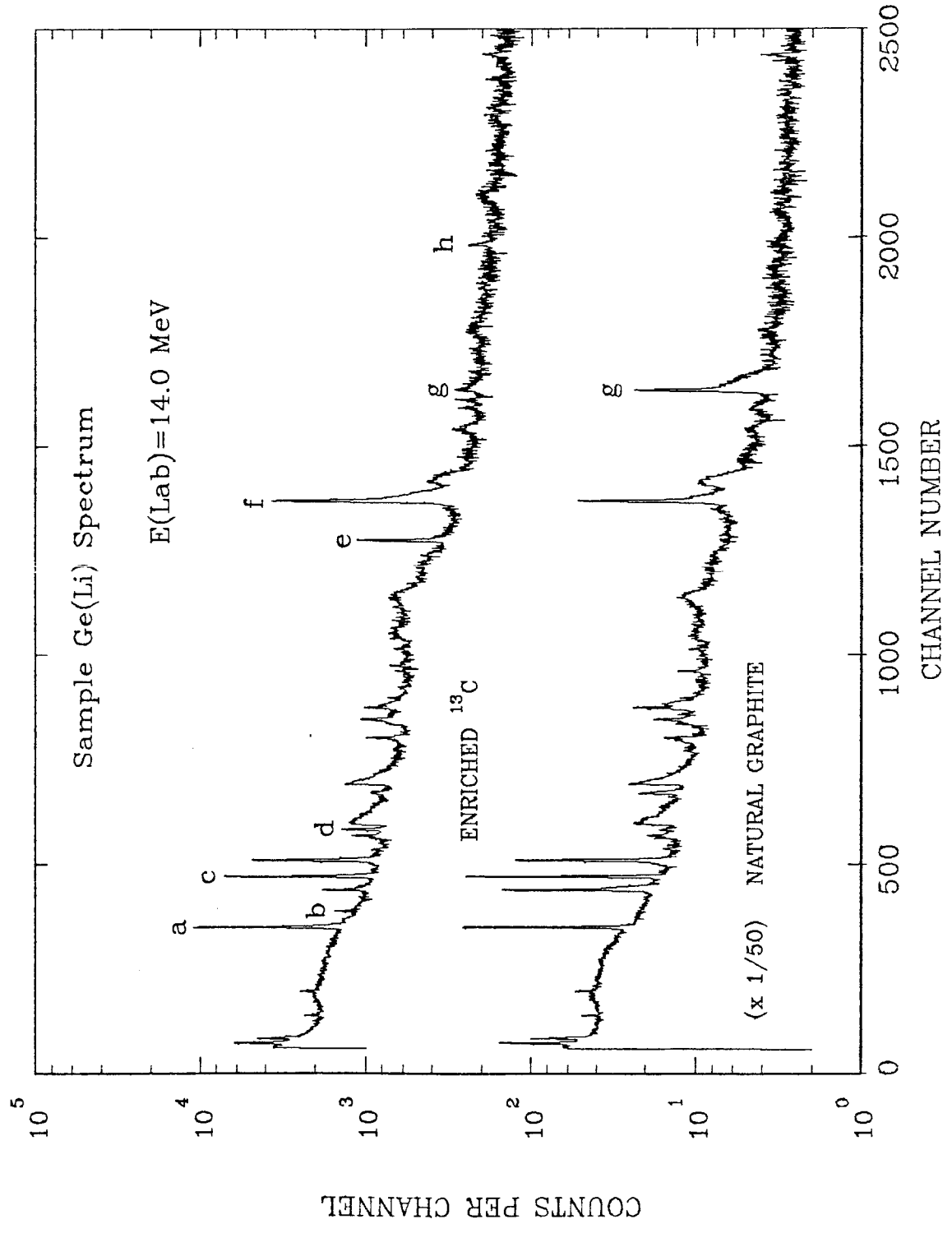
Sample Ge(Li) Spectrum
E(Lab)=14.0 MeV
a
b
c
d
e
f
g
h
ENRICHED ^{13}C
(x 1/50) NATURAL GRAPHITE
COUNTS PER CHANNEL
CHANNEL NUMBER
0
500
1000
1500
2000
2500
10^0
10^1
10^2
10^3
10^4
10^5

FIGURE 9

SAMPLE GE(LI) SPECTRUM: DELAYED ACTIVITY

Sample Ge(Li) spectrum of the delayed activity from ^{13}C on a ^{13}C-enriched target. This spectrum was acquired in 10 minutes of counting. All of the labeled peaks arise from $^{24}Na(\beta^-)^{24}Mg^*$. These are a: β^-- annihilation (511 keV), b: $^{24}Mg^*[1 \rightarrow 0]$ (1369), e:$^{24}Mg^*$ $[2 \rightarrow 1]$ (2754) (d: first escape peak (2243), c: second escape peak (1732)).

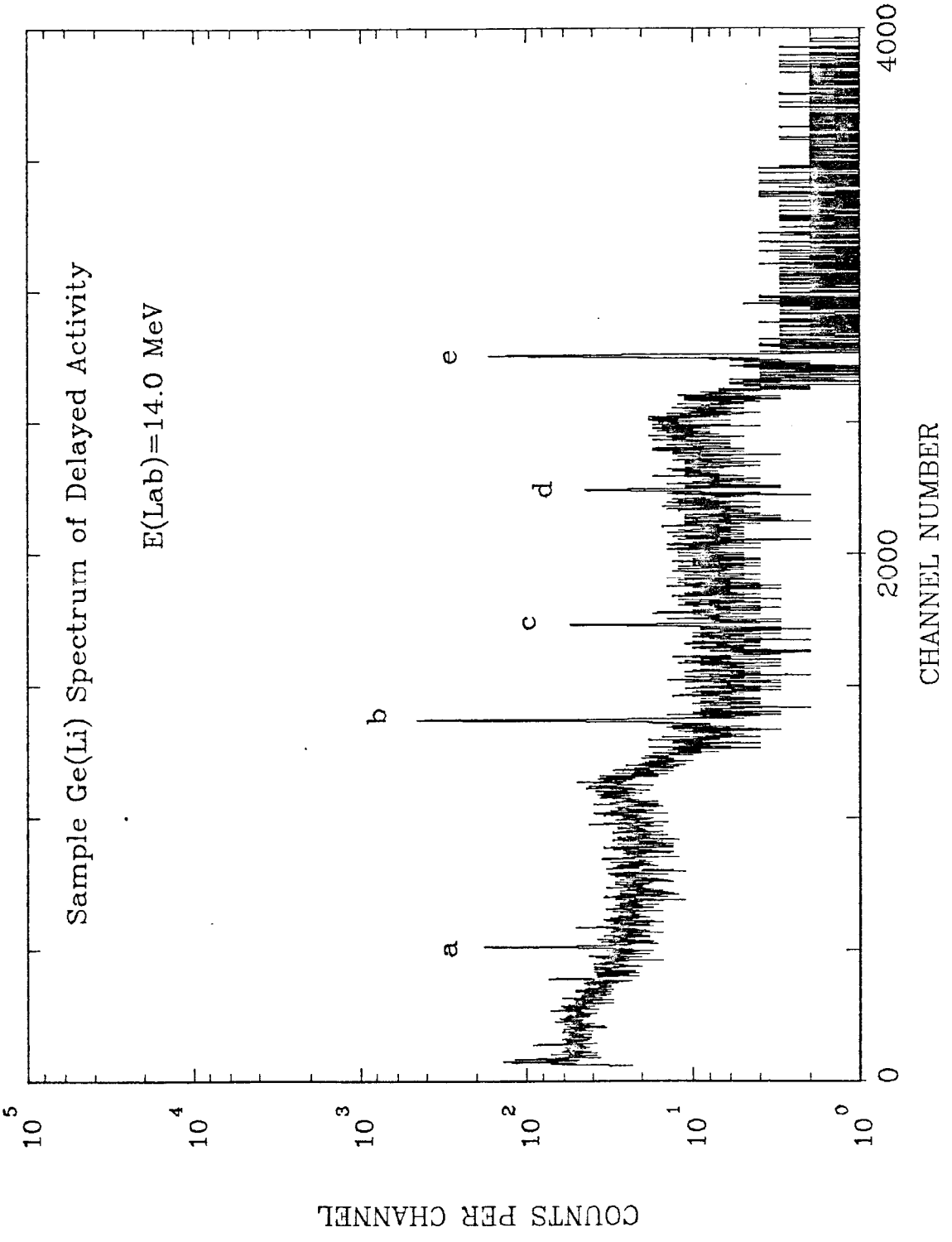
Sample Ge(Li) Spectrum of Delayed Activity
E(Lab)=14.0 MeV
a
b
c
d
e
COUNTS PER CHANNEL
CHANNEL NUMBER
0
2000
4000
10^0
10^1
10^2
10^3
10^4
10^5

FIGURE 10

ABSOLUTE GE(LI) PHOTOPEAK EFFICIENCIES

Full-energy peak efficiencies were determined over the range 250 keV $< E_\gamma <$ 3300 keV for the Ge(Li) detector in the geometry of figure 6. The experimental points are labeled by radioactive nuclide. Full details are given in Section II.B.4 and Appendix A.

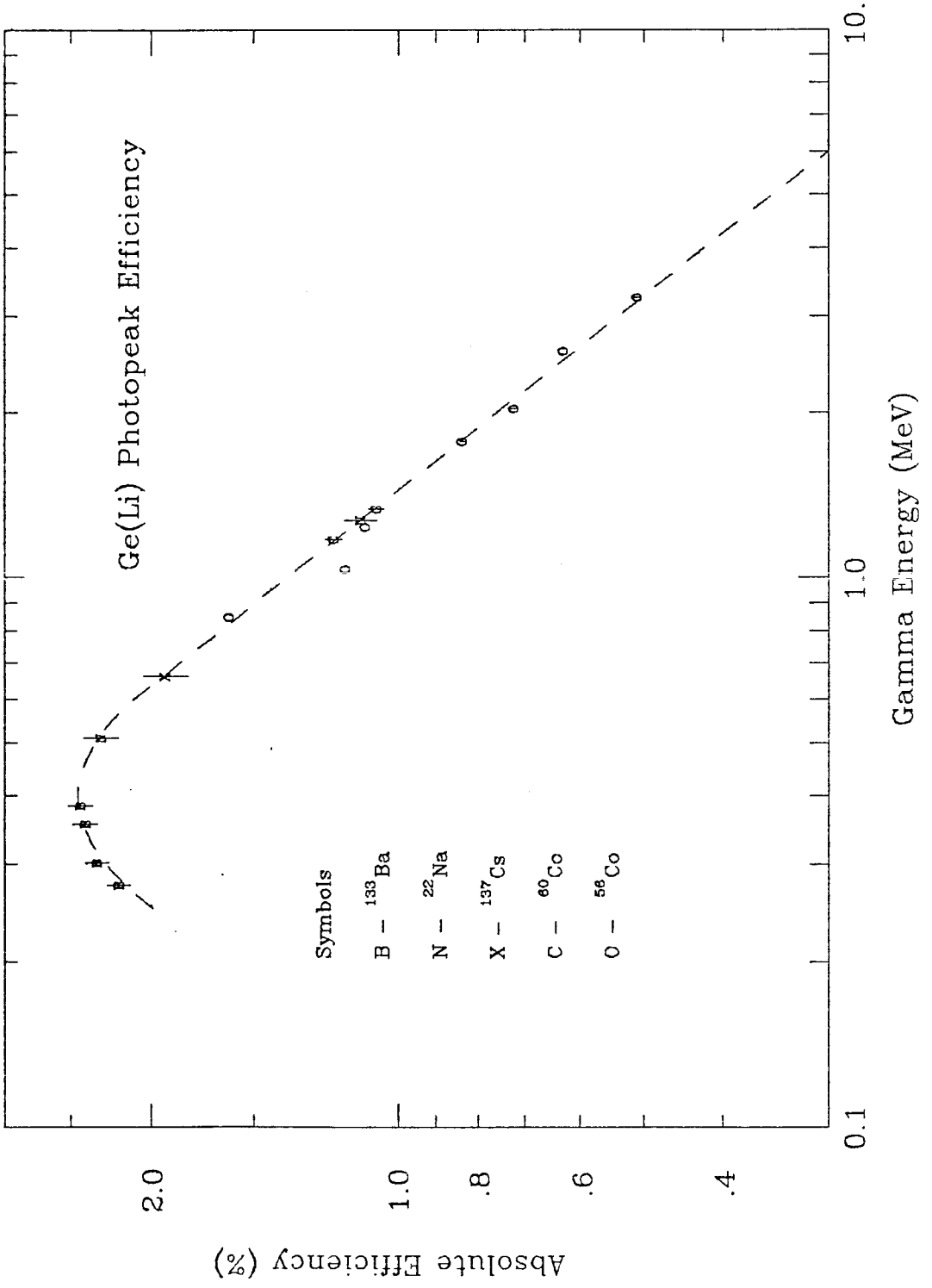
Ge(Li) Photopeak Efficiency
Absolute Efficiency (%)
2.0
1.0
.8
.6
.4
0.1
1.0
10.
Gamma Energy (MeV)
Symbols
B - 133Ba
N - 22Na
X - 137Cs
C - 60Co
O - 56Co

FIGURE 11

SUMMING AND BRANCHING CORRECTION FACTORS

Summing and branching correction factors (β)calculated for γ transitions observed in the $^{13}C+^{13}C$ reaction are given as a function of collision energy. The excited state population is obtained from a Hauser-Feshbach statistical model and the resulting cascade corrections are computed using published branching ratios. This procedure is explained more fully in Section II.B.4 and Appendix B.

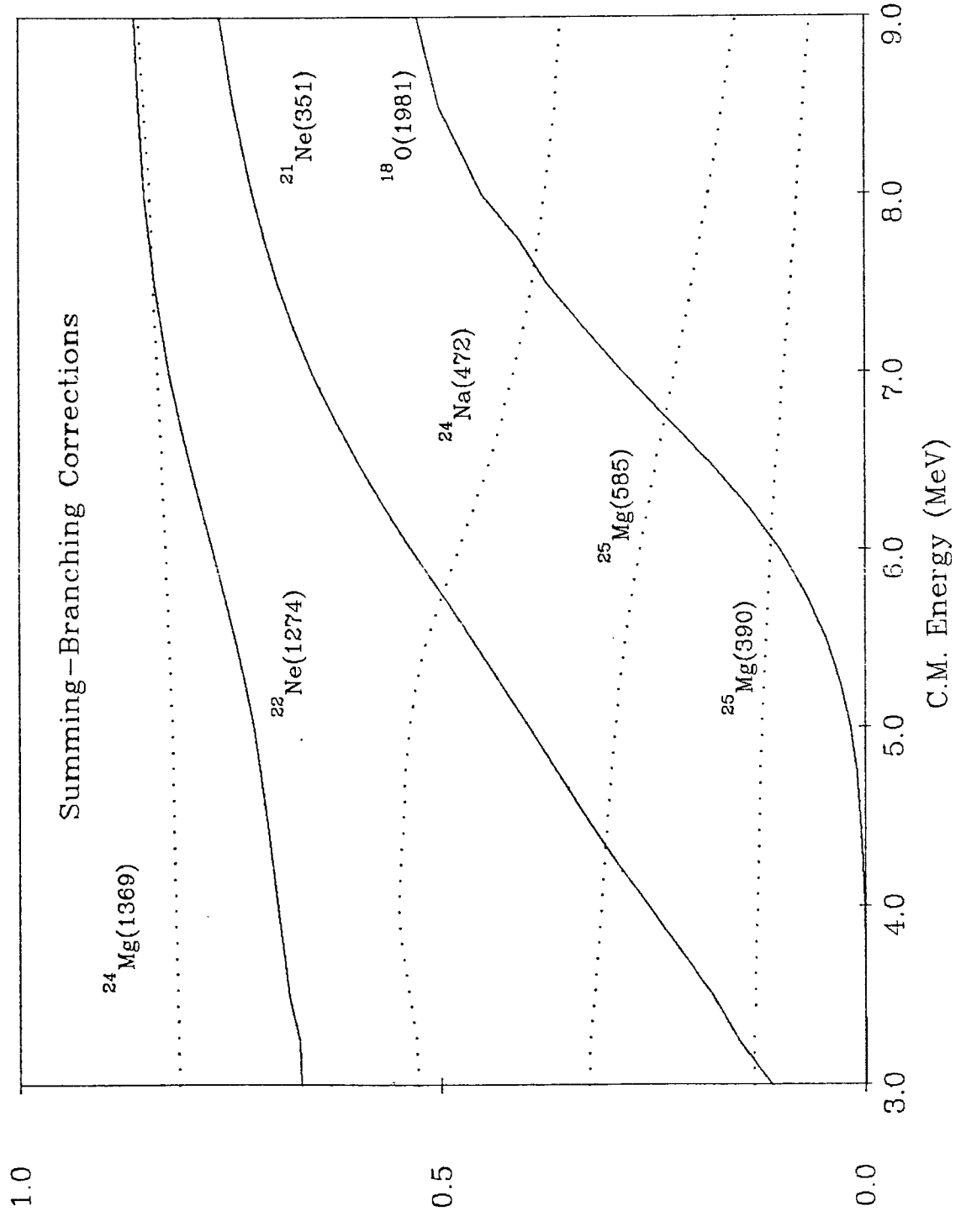
Summing-Branching Corrections
^{24}Mg(1369)
^{22}Ne(1274)
^{21}Ne(351)
^{18}O(1981)
^{24}Na(472)
^{25}Mg(585)
^{25}Mg(390)
1.0
0.5
0.0
3.0
4.0
5.0
6.0
7.0
8.0
9.0
C.M. Energy (MeV)
Summing-Branching Factor

FIGURE 12

PARTIAL PRODUCTION CROSS SECTIONS FOR $^{13}C+^{13}C$

Elemental production cross sections for the residual nuclei: ^{18}O, ^{22}Ne, and ^{25}Mg, as deduced from γ-ray measurements. Numerical values are listed in Table 1. Error bars reflect counting statistics only.

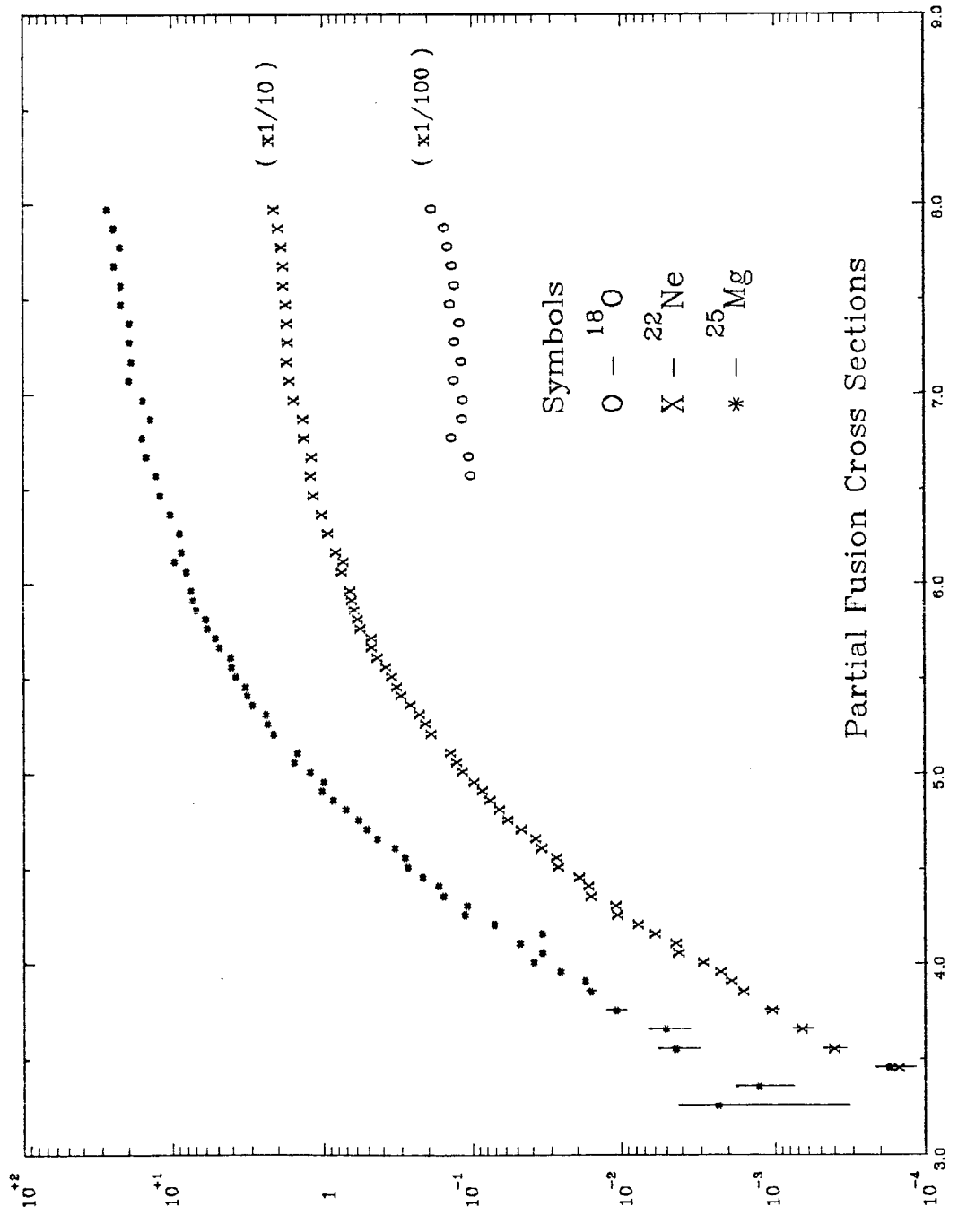
Partial Fusion Cross Sections
Symbols
O – ^{18}O
X – ^{22}Ne
* – ^{25}Mg
(x1/10)
(x1/100)
C. M. Energy (MeV)
Cross Section (mb)
10^{+2}
10^{+1}
1
10^{-1}
10^{-2}
10^{-3}
10^{-4}
3.0
4.0
5.0
6.0
7.0
8.0
9.0

FIGURE 13

PARTIAL PRODUCTION CROSS SECTIONS FOR $^{13}C+^{13}C$

Elemental production cross sections for the residual nuclei: ^{21}Ne, ^{24}Na, and ^{24}Mg, as deduced from γ-ray measurements. Numerical values are listed in Table 1. Error bars reflect counting statistics only.

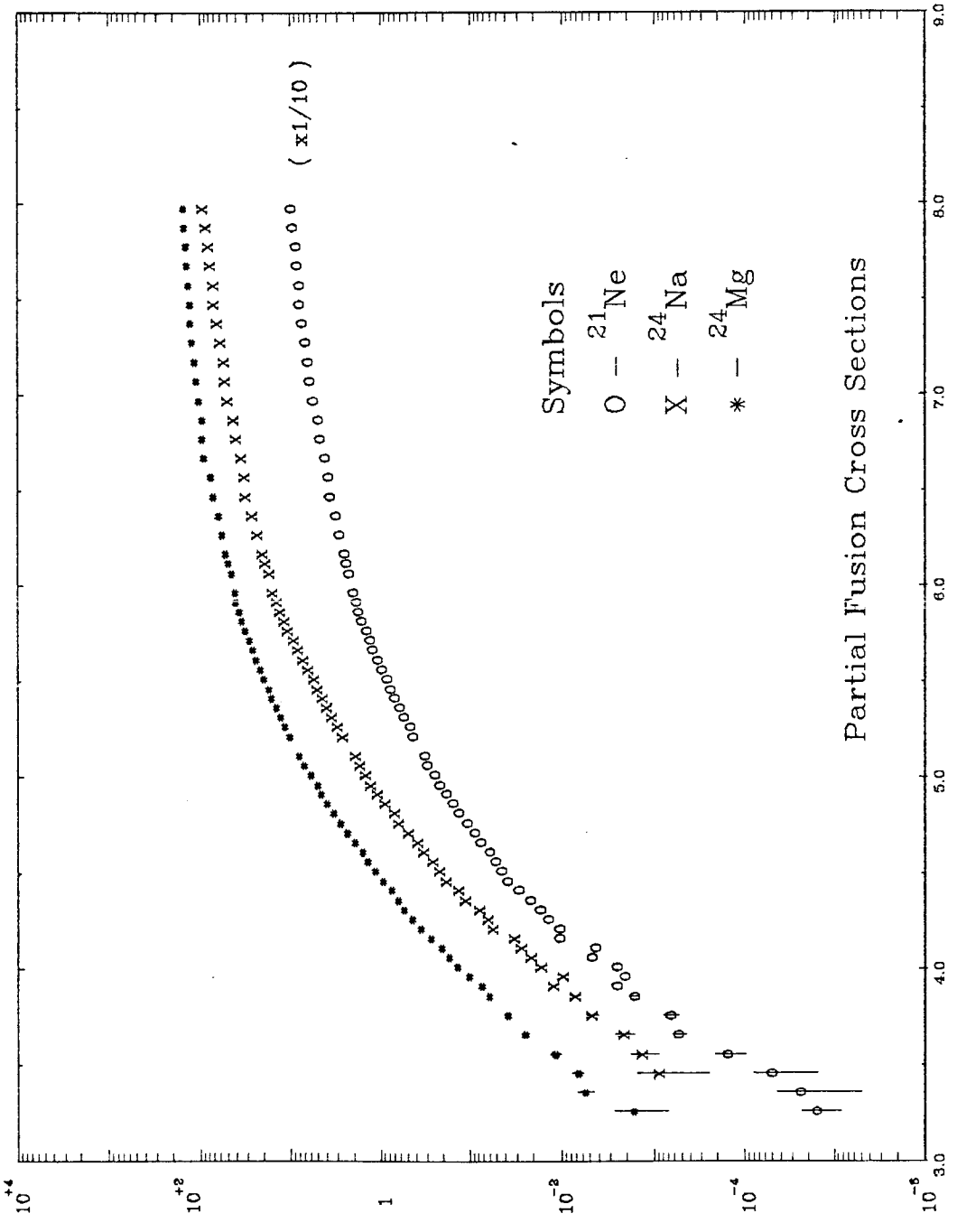
Partial Fusion Cross Sections
Symbols
O — ^{21}Ne
X — ^{24}Na
* — ^{24}Mg
(x1/10)
Cross Section (mb)
C. M. Energy (MeV)
10^+4
10^+2
1
10^-2
10^-4
10^-6
3.0
4.0
5.0
6.0
7.0
8.0
9.0

FIGURE 14

PARTIAL AND TOTAL FUSION CROSS SECTIONS FOR $^{13}C+^{13}C$

Data from figure 12 and figure 13 are compared to the total cross section. The partial and total fusion cross sections are listed in Table 1. Channels involving the evaporation of at least one neutron dominate the reaction cross section, as expected. The reaction channel $p + {}^{25}Na$ was not observed. Error bars reflect only counting statistics. The total cross section has an additional systematic error of ±15%, which is the sum (in quadrature) of uncertainties of ±10% in the summing-branching factors, ±4% in target thickness, ±5% in beam integration and ±4% in Ge(Li) efficiency.

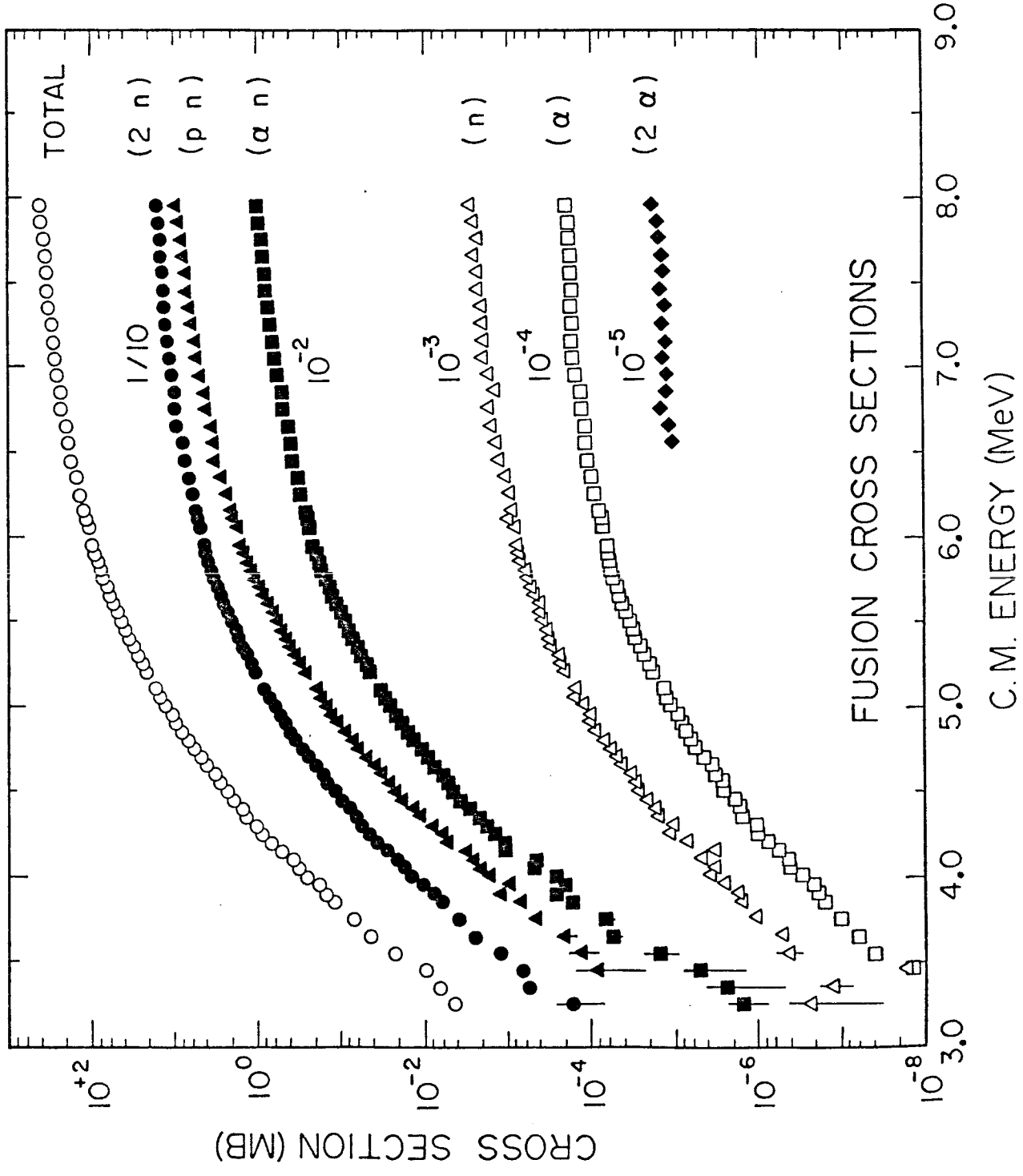
FUSION CROSS SECTIONS
CROSS SECTION (MB)
C.M. ENERGY (MeV)
TOTAL
(2 n)
(p n)
(α n)
(n)
(α)
(2 α)
1/10
10^-2
10^-3
10^-4
10^-5
10^+2
10^0
10^-2
10^-4
10^-6
10^-8
3.0
4.0
5.0
6.0
7.0
8.0
9.0

FIGURE 15

RATIO OF ^{25}Mg CROSS SECTIONS

The ratio of the ^{25}Mg production cross sections as found from the yield of 390 keV gamma rays to that determined by the yield of 585 keV gamma rays is plotted as a function of energy. Error bars are omitted for clarity. The scatter of points, especially at low energies, indicates that the statistical errors become rather large. The average of all points is given by the dotted line. Despite the systematic linear deviation, $\sigma_{390}/\sigma_{585}$ remains within ±25% of unity.

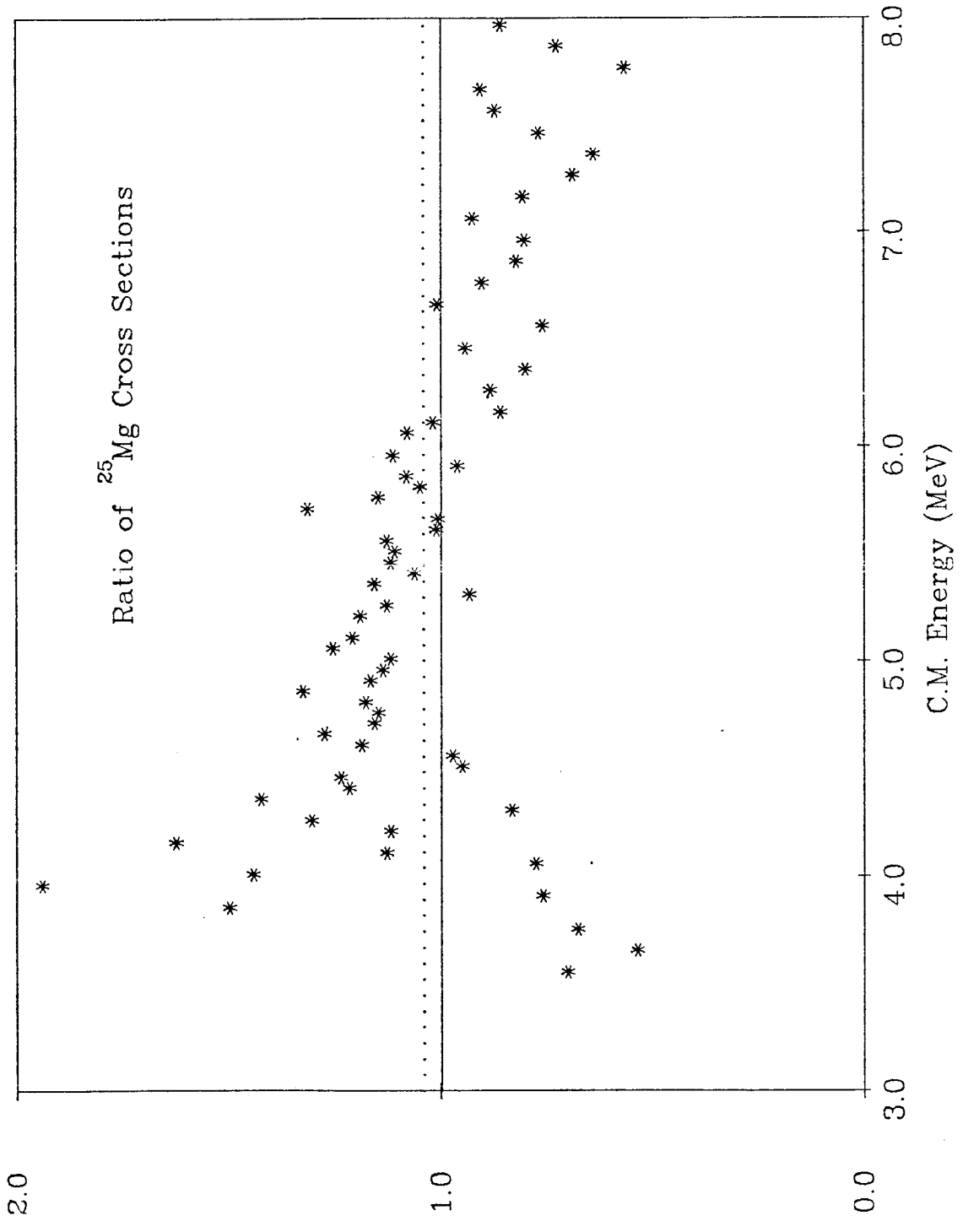
Ratio of ^{25}Mg Cross Sections
Ratio
2.0
1.0
0.0
3.0
4.0
5.0
6.0
7.0
8.0
C.M. Energy (MeV)

FIGURE 16

PARTICLE SPECTRA: ENRICHED TARGETS

These particle spectra were observed at various angles in ^{13}C bombardment of ^{13}C-enriched targets at $E_{lab} = 16.0$ MeV. The energy scale is arbitrary. Peak labels are as follows: a: $^{13}C+^{1}H$, ^{1}H recoil; b: $^{13}C+^{12}C$, ^{13}C scattering; c: $^{13}C+^{13}C$, ^{13}C scattering and recoil, $^{13}C+^{12}C$, ^{12}C recoil, $^{13}C+^{16}O$, ^{16}O recoil; d: $^{13}C+^{16}O$, ^{13}C scattering; e: $^{13}C+^{197}Au$, ^{13}C scattering.

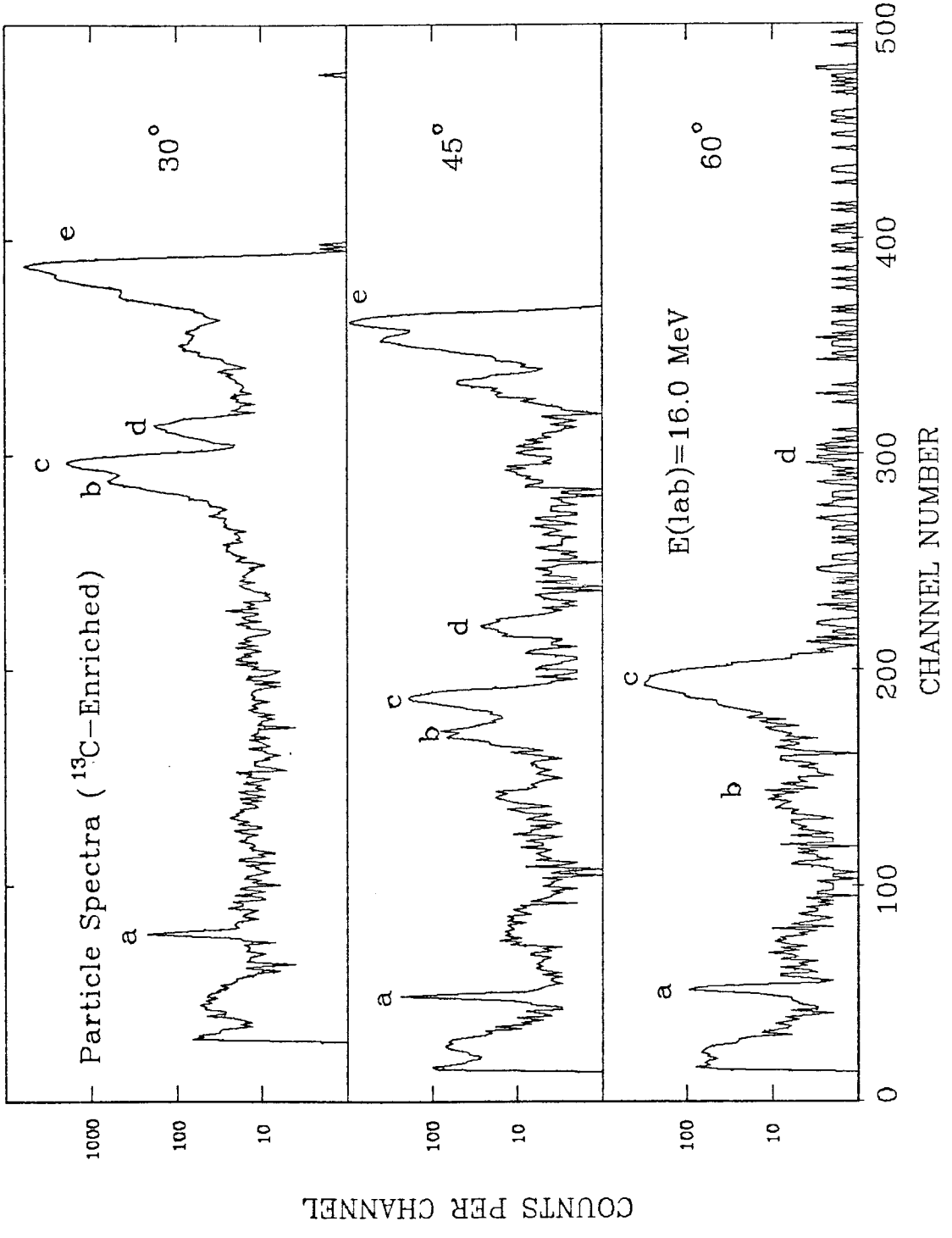
Particle Spectra (^{13}C–Enriched)
E(lab)=16.0 MeV
30°
45°
60°
a
b
c
d
e
COUNTS PER CHANNEL
CHANNEL NUMBER
1000
100
10
0
100
200
300
400
500

FIGURE 17

PARTICLE SPECTRA: NATURAL GRAPHITE TARGETS

These particle spectra were observed at various angles in ^{13}C bombardment of commercial carbon foils at E_{lab} = 16.0 MeV. The energy scale is arbitrary. Peak labels are as follows: a: $^{13}C+^{1}H$, ^{1}H recoil; b: $^{13}C+^{12}C$, ^{13}C scattering; c: $^{13}C+^{13}C$, ^{13}C scattering and recoil (small), $^{13}C+^{12}C$, ^{12}C recoil, $^{13}C+^{16}O$, ^{16}O recoil; d: $^{13}C+^{16}O$, ^{13}C scattering; e: $^{13}C+^{197}Au$, ^{13}C scattering.

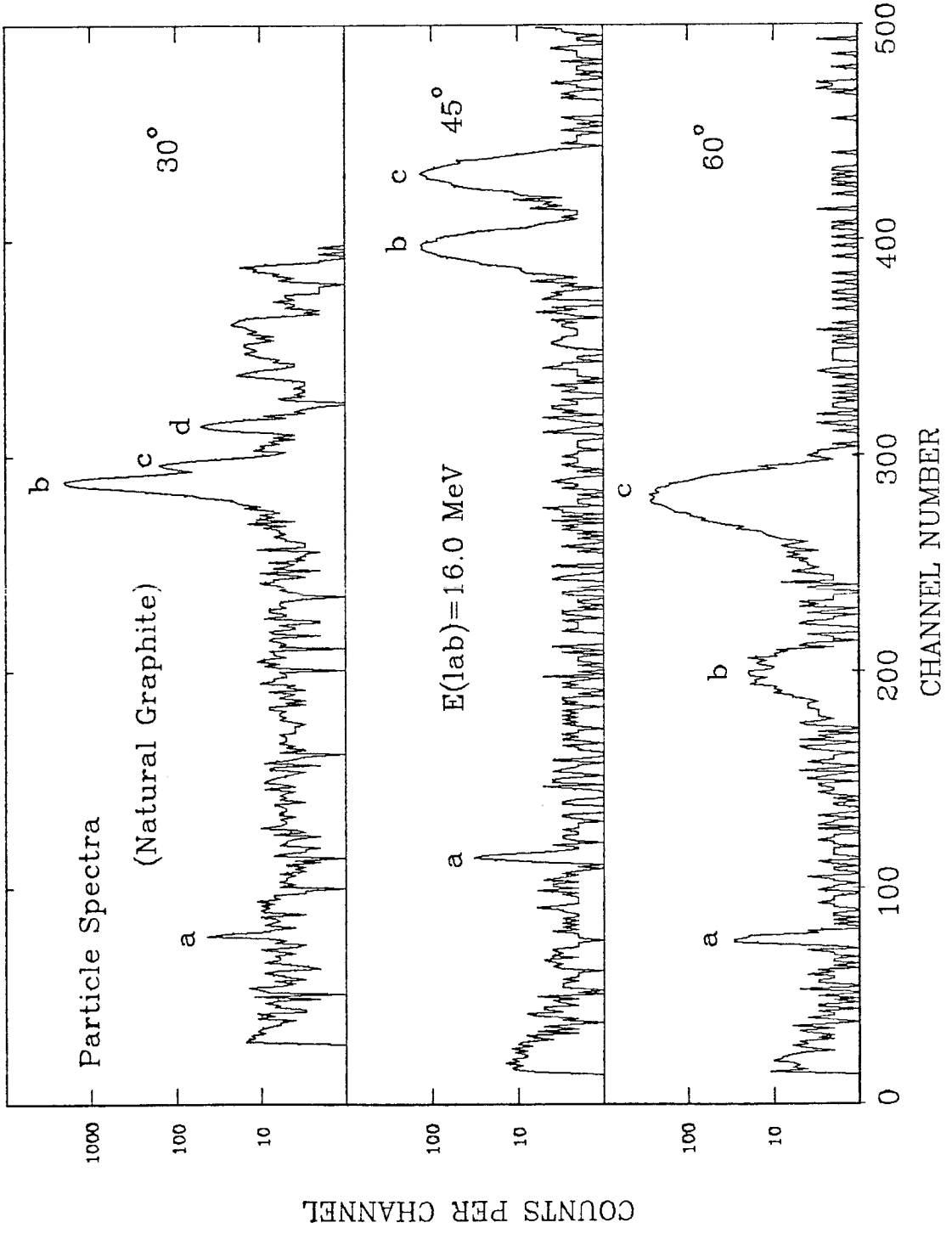
Particle Spectra
(Natural Graphite)
E(lab)=16.0 MeV
30°
45°
60°
a
b
c
d
COUNTS PER CHANNEL
CHANNEL NUMBER
1000
100
10
0
100
200
300
400
500

FIGURE 18

ELASTIC SCATTERING DATA: EXCITATION FUNCTIONS

The data plotted are the result of the present measurement of the $^{13}C+^{13}C$ elastic scattering excitation functions for $\vartheta_{c.m.} = 60°$, 70°, 80°, and 90° (Tr83). These numbers are listed in Table 2. Excitation functions measured by Helb *et al.* (He73) ($\vartheta_{c.m.} = 60°$ and 90°) and Korotky *et al.* (Ko81) ($\vartheta_{c.m.} = 90°$) are included for comparison. Error bars represent counting statistical uncertainties only.

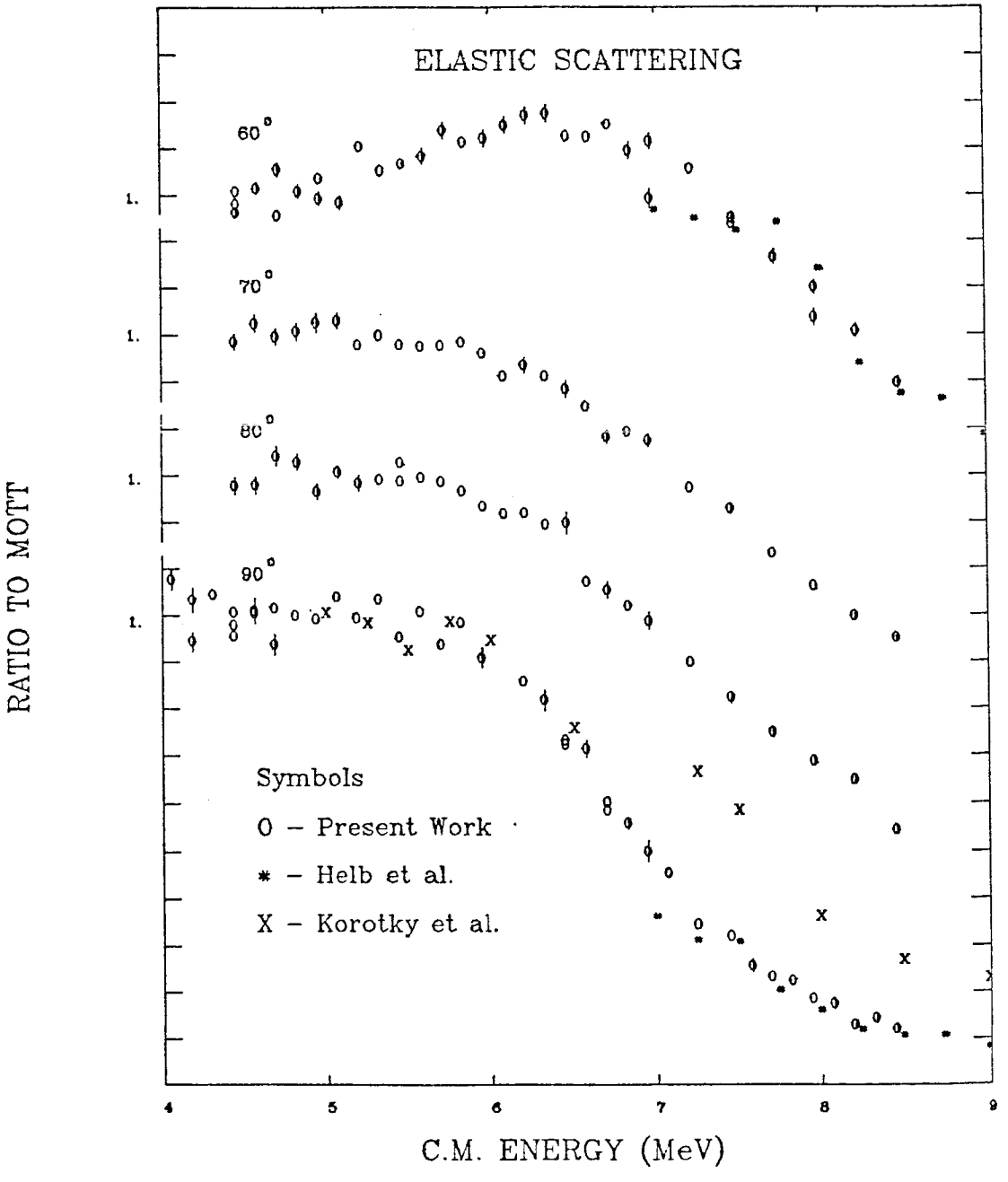
ELASTIC SCATTERING
60°
70°
80°
90°
1.
1.
1.
1.
Symbols
O – Present Work
* – Helb et al.
X – Korotky et al.
4
5
6
7
8
9
C.M. ENERGY (MeV)
RATIO TO MOTT

FIGURE 19

ELASTIC SCATTERING DATA: ANGULAR DISTRIBUTIONS

The data plotted are the result of the present measurement of $^{13}C+^{13}C$ elastic scattering angular distributions taken at $E_{c.m.} = 7.0$ MeV and 8.0 MeV (Tr83). These numbers are listed in Table 3. The data at 8.0 MeV is compared to the data of Helb *et al.* (He73). Error bars refer to counting statistical uncertainties only.

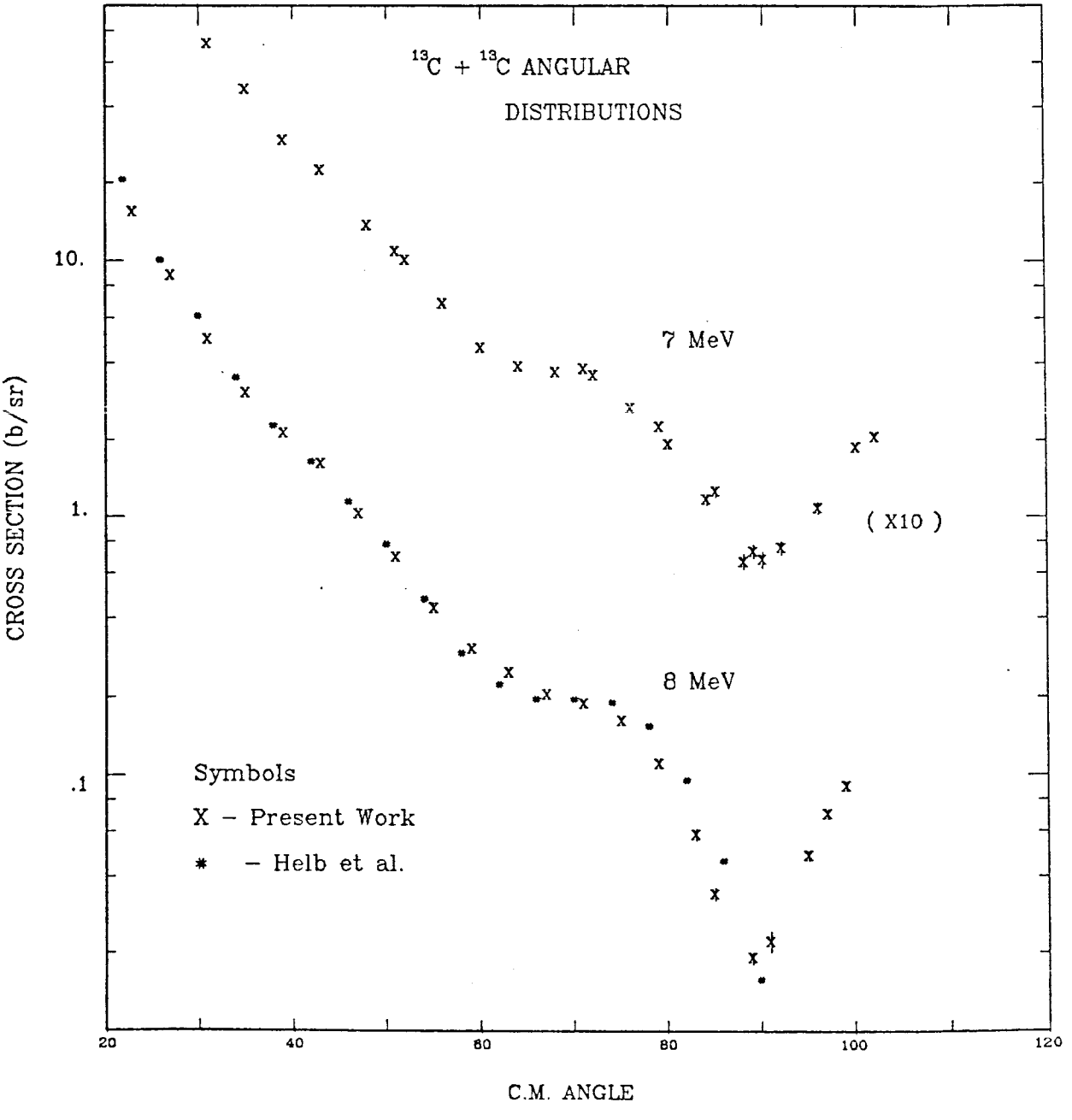
$^{13}C + ^{13}C$ ANGULAR
DISTRIBUTIONS
7 MeV
(X10)
8 MeV
Symbols
X – Present Work
* – Helb et al.
CROSS SECTION (b/sr)
10.
1.
.1
20
40
60
80
100
120
C.M. ANGLE

FIGURE 20

COMPARISON OF $^{13}C+^{13}C$ S-FACTOR DATA

This figure is a comparison of the low energy S-factor data available for $^{13}C+^{13}C$. The present data (Tr83) are compared to the NaI measurements of Chatterjee *et al.* (Ch80) and Dasmahapatra *et al.* (Da82). The latter measurements have been corrected for ground state branching. Error bars represent counting statistical uncertainties only.

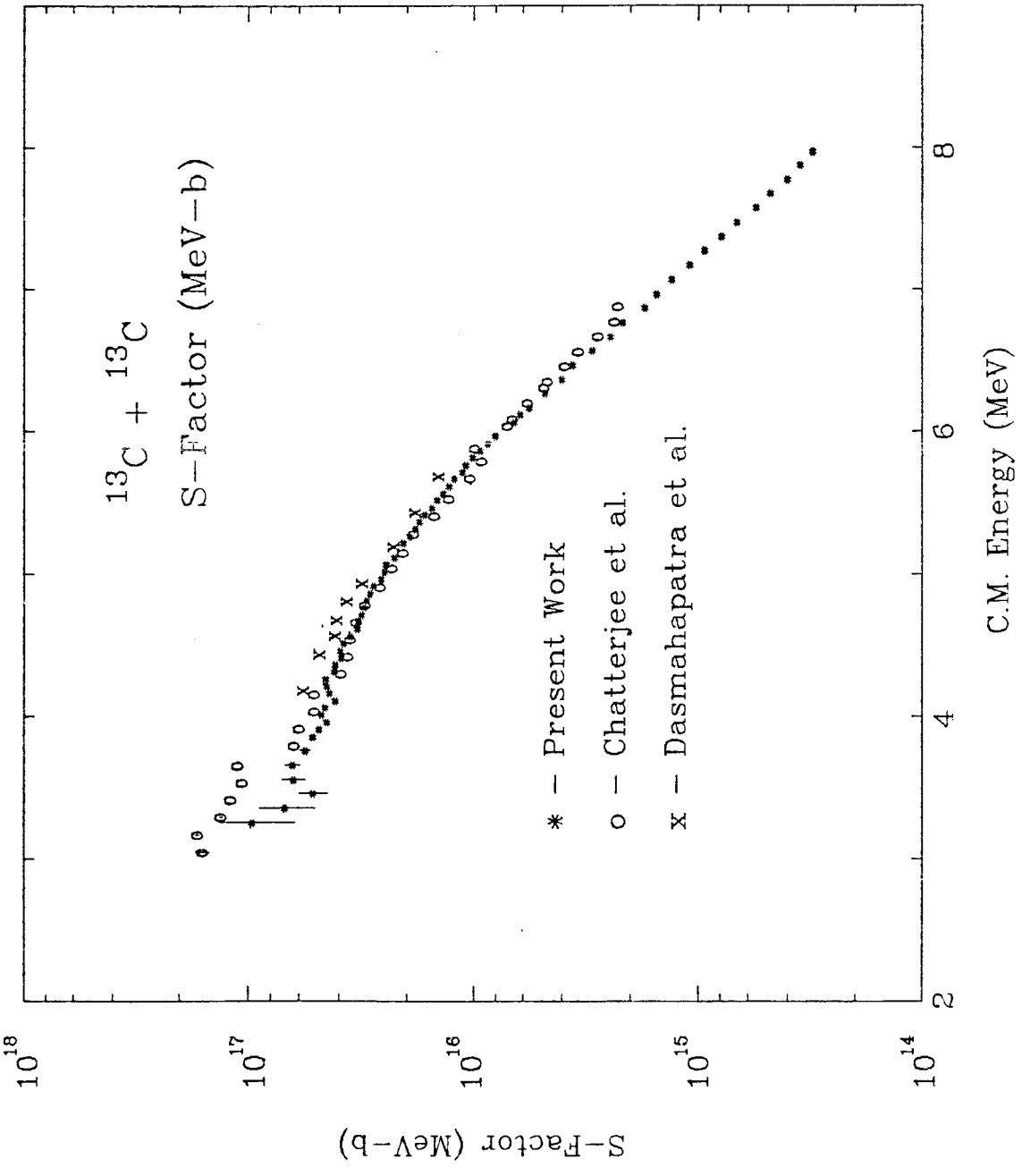
$^{13}C + ^{13}C$
S-Factor (MeV-b)
* - Present Work
o - Chatterjee et al.
x - Dasmahapatra et al.
S-Factor (MeV-b)
C.M. Energy (MeV)
10^{18}
10^{17}
10^{16}
10^{15}
10^{14}
2
4
6
8

FIGURE 21

CARBON ISOTOPE FUSION

Carbon isotope fusion S-factors are compared for data available prior to the year 1980. Symbols have meaning as follows:

$^{13}C+^{13}C$:	C -	Chatterjee *et al.*	(Ch80)
$^{12}C+^{13}C$:	D -	Dayras *et al.*	(Da76b)
$^{12}C+^{12}C$:	H -	High and Cujec	(Hi77)
	M -	Mazarakis and Stephens	(Ma73b)
	P -	Patterson *et al.*	(Pa69)

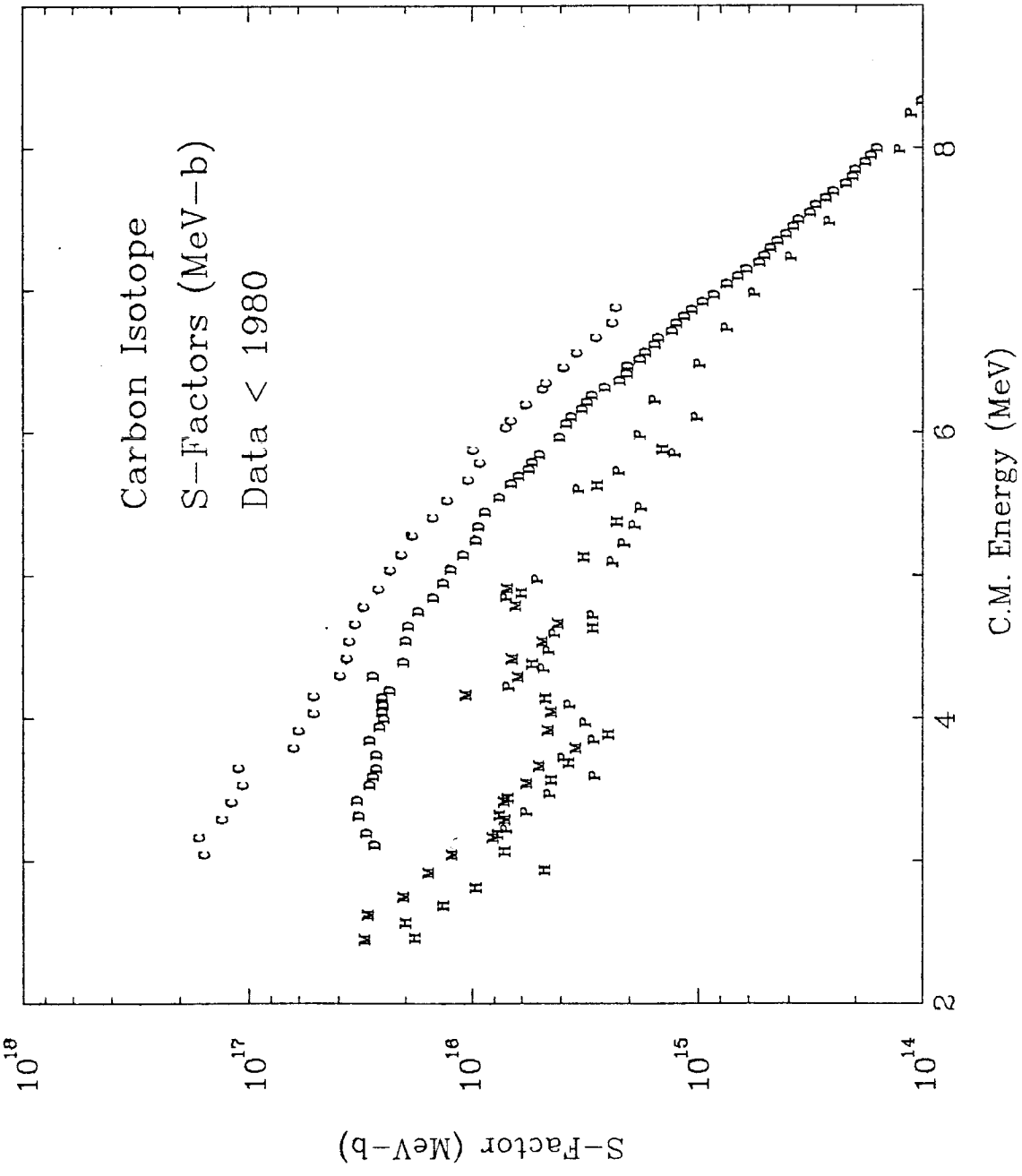
Carbon Isotope
S-Factors (MeV-b)
Data < 1980
S-Factor (MeV-b)
C.M. Energy (MeV)
10^{19}
10^{17}
10^{16}
10^{15}
10^{14}
2
4
6
8

FIGURE 22

EFFECTIVE ENERGY CORRECTIONS

Corrections to the effective energies in the $^{12}C+^{12}C$ data of Mazarakis and Stephens (Ma73b) were found to produce substantial changes in the resulting values of $\tilde{S}(E)$. The solid line connects the data points of Becker *et al.* (Be78, Be81b), which is a remeasurement of the light charged particles. The effective energy corrections are explained more fully in Section III.A.

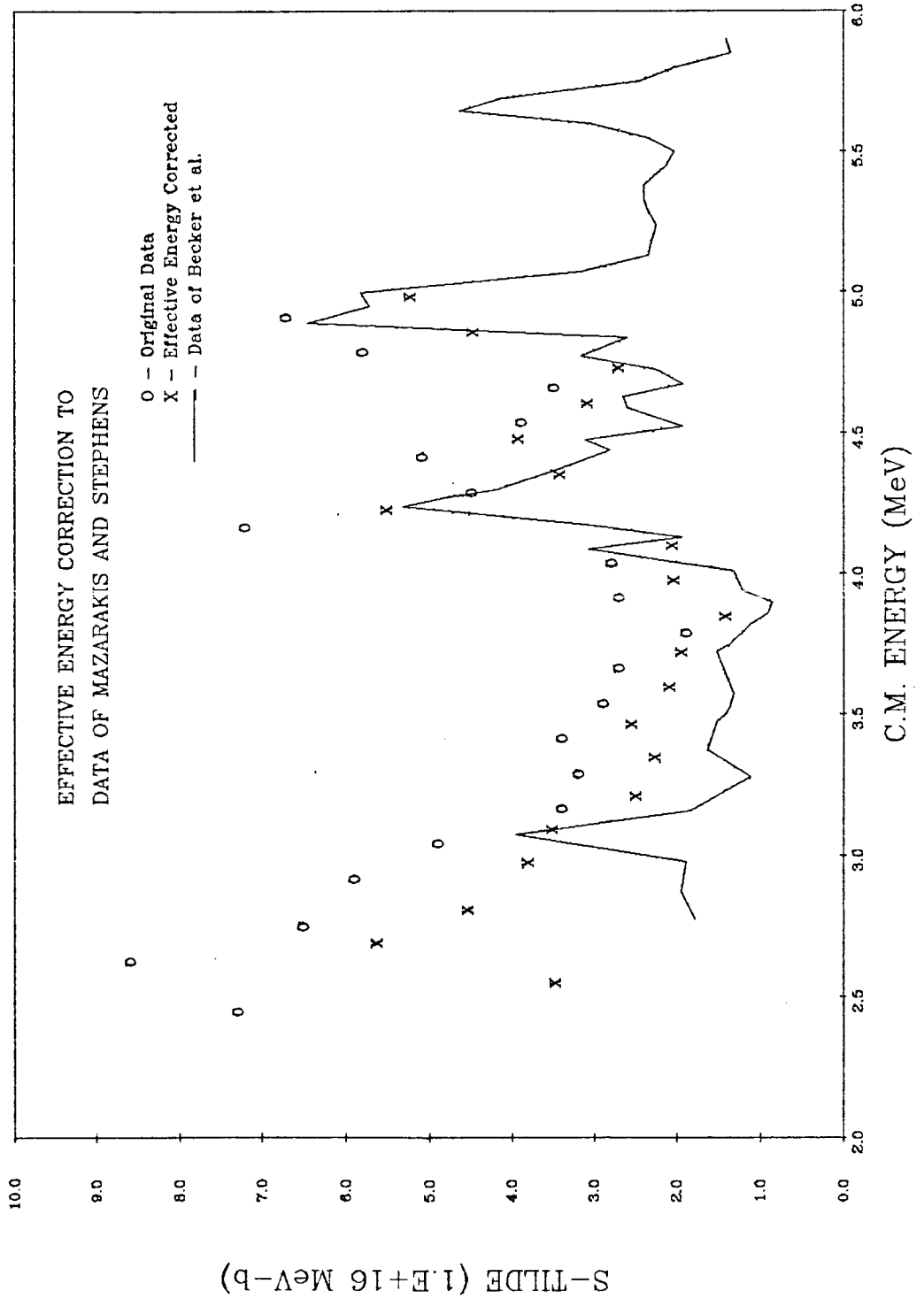
EFFECTIVE ENERGY CORRECTION TO
DATA OF MAZARAKIS AND STEPHENS
O – Original Data
X – Effective Energy Corrected
—— – Data of Becker et al.
S-TILDE (1.E+16 MeV-b)
C.M. ENERGY (MeV)
10.0
9.0
8.0
7.0
6.0
5.0
4.0
3.0
2.0
1.0
0.0
2.0
2.5
3.0
3.5
4.0
4.5
5.0
5.5
6.0

FIGURE 23

COMPARISON OF LOW ENERGY $^{12}C+^{12}C$ DATA

Several sets of low energy $\tilde{S}$ factors for $^{12}C+^{12}C$ are compared. The symbol table is as follows:

B -	Becker *et al.*	(Be78, Be81b)
H -	High and Cujec	(Hi77)
M -	Mazarakis and Stephens	(Ma73b)
P -	Patterson *et al.*	(Pa69)

The solid line connecting the thin target data of Becker *et al.* is merely to guide the eye. At high energies, all data sets generally agree, but below about 5 MeV the thin target data "off-resonance" are much less than the thick target data. Since the normalization at the resonances agrees, this effect may be introduced by the energy-averaging over the closely-spaced peaks.

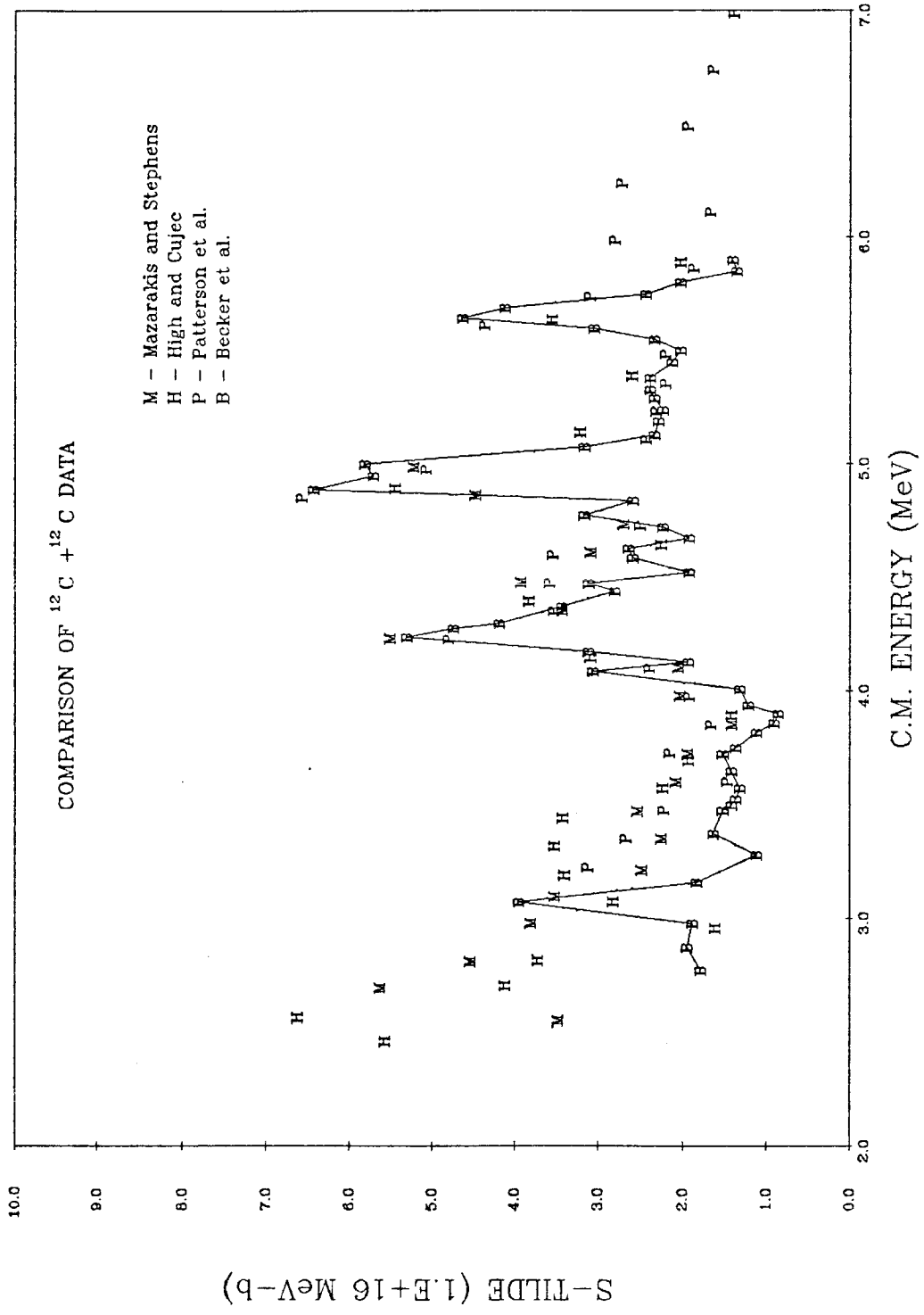
COMPARISON OF $^{12}C + ^{12}C$ DATA
M – Mazarakis and Stephens
H – High and Cujec
P – Patterson et al.
B – Becker et al.
S–TILDE (1.E+16 MeV–b)
C.M. ENERGY (MeV)
10.0
9.0
8.0
7.0
6.0
5.0
4.0
3.0
2.0
1.0
0.0
2.0
3.0
4.0
5.0
6.0
7.0

FIGURE 24

CARBON ISOTOPE FUSION

The S-factors for the most recent data on carbon isotope fusion are compared. Symbols have meaning as follows:

$^{13}C+^{13}C$:	T -	Trentalange *et al.*	(Tr83)
	+ -	Dasmahapatra *et al.*	(Da82)
	C -	Chatterjee *et al.*	(Ch80)
$^{12}C+^{13}C$:	O -	Dasmahapatra *et al.*	(Da82)
	D -	Dayras *et al.*	(Da76b)
$^{12}C+^{12}C$:	B -	Becker *et al.*	(Be78, Be81b)
	H -	High and Cujec	(Hi77)
	P -	Patterson *et al.*	(Pa69)

The lowest energy points of Chatterjee *et al.* have been omitted for reasons explained in Section II.D.1.

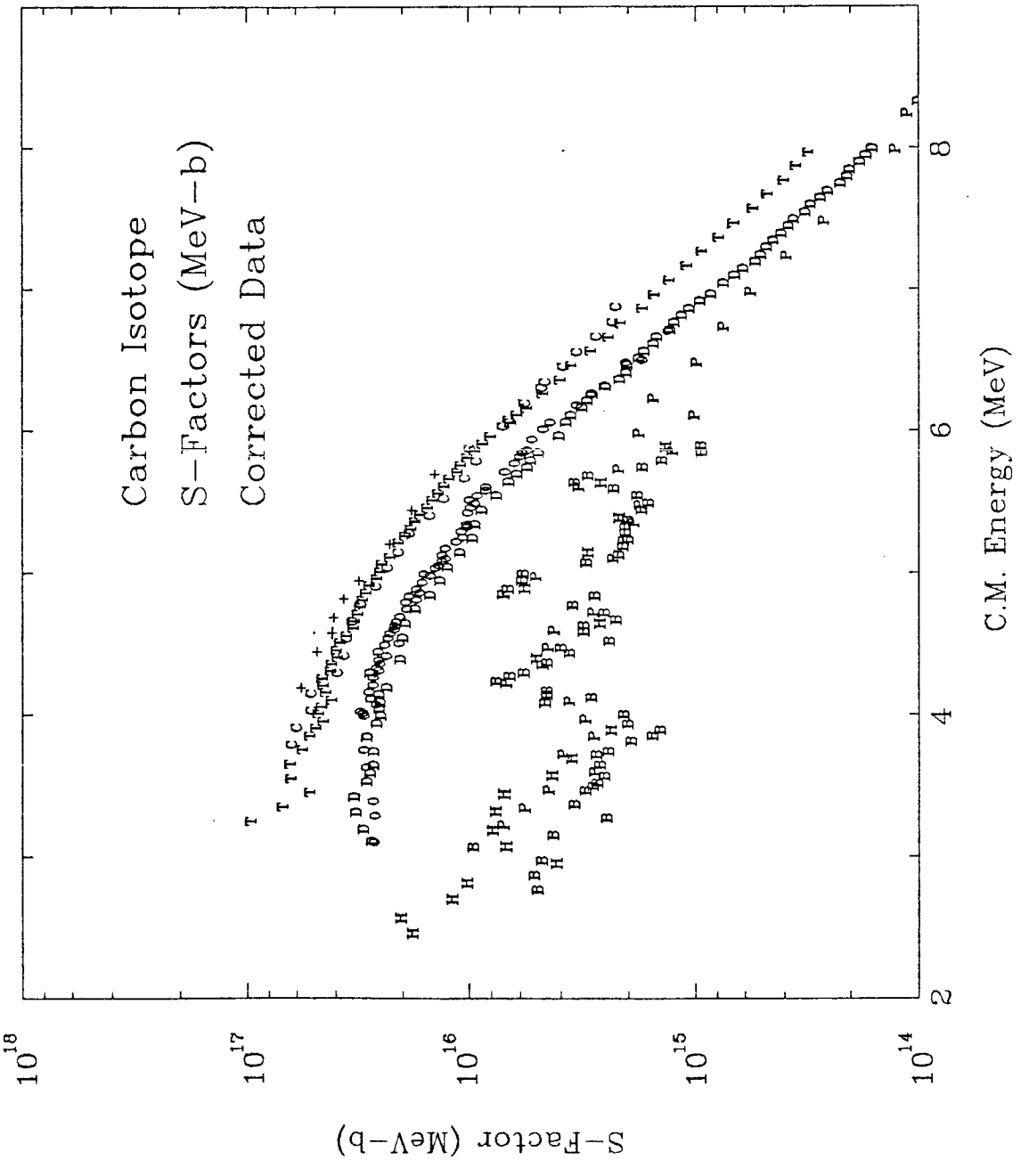
Carbon Isotope
S-Factors (MeV-b)
Corrected Data
S-Factor (MeV-b)
C.M. Energy (MeV)
10^18
10^17
10^16
10^15
10^14
2
4
6
8

FIGURE 25

HILL-WHEELER / GAMOW TRANSMISSION FUNCTIONS

Ratio of Hill-Wheeler to Gamow form of the transmission function. The curve plotted is $e^{\gamma}/(1+e^{\gamma})$, where

$$\gamma = 4\eta\,[\cos^{-1}(E/B)^{1/2} - (E/B)^{1/2}(1-E/B)^{1/2}] \quad ,$$

for the case of $^{12}C+^{12}C$ ($\eta = 87.21/\sqrt{E}$ and $B = 6.0$ MeV). This demonstrates that the Gamow form is a valid approximation to the Hill-Wheeler expression only for $E/B < 0.7$.

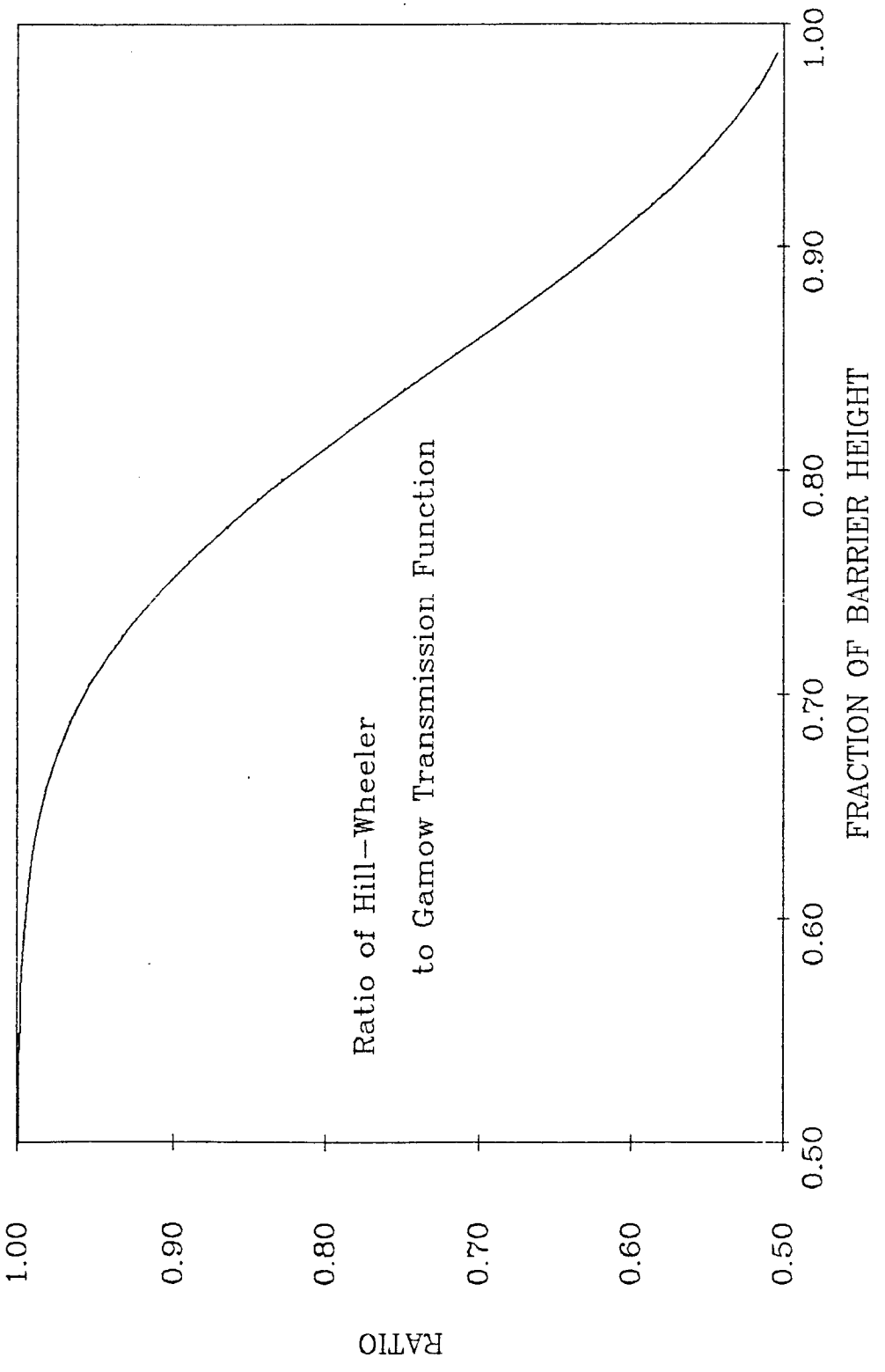
Ratio of Hill-Wheeler
to Gamow Transmission Function
RATIO
1.00
0.90
0.80
0.70
0.60
0.50
0.50
0.60
0.70
0.80
0.90
1.00
FRACTION OF BARRIER HEIGHT

FIGURE 26

CROSS SECTION DECOMPOSITION BY PARTIAL WAVES

The partial wave contributions to the fusion cross section for $^{12}C+^{12}C$ are given as a function of energy. The fraction of the reaction strength in each partial wave was computed from the transmission functions of an optical model using a shallow potential (see Section III.C.3). The salient features of these curves were found to be insensitive to the parameters of the optical potential. Curves are labeled by their orbital angular momentum quantum number. Odd L values are forbidden because the colliding particles are identical bosons.

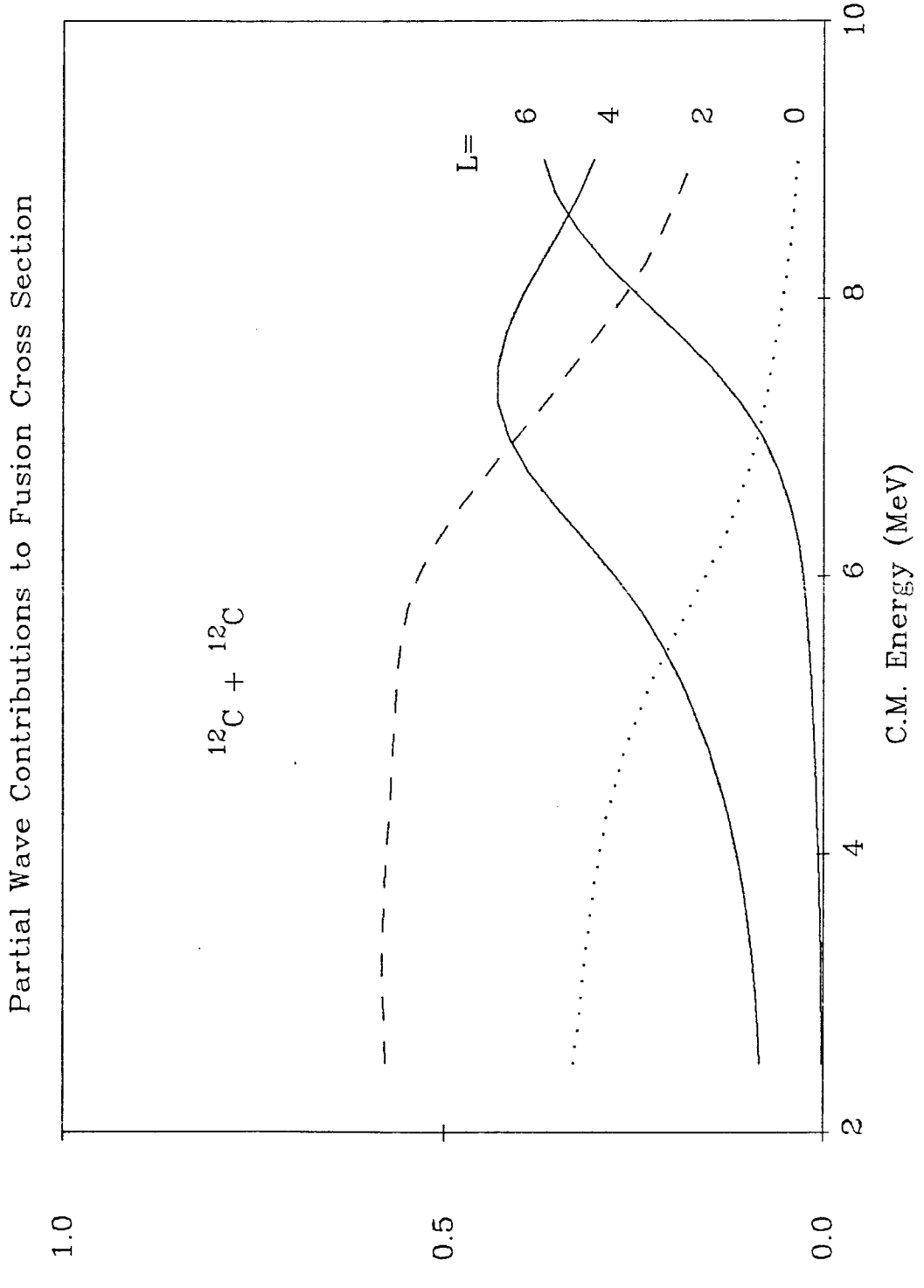
Partial Wave Contributions to Fusion Cross Section
$^{12}C + ^{12}C$
L=
6
4
2
0
Fraction
1.0
0.5
0.0
2
4
6
8
10
C.M. Energy (MeV)

FIGURE 27

CROSS SECTION DECOMPOSITION BY PARTIAL WAVES

The partial wave contributions to the fusion cross section for $^{12}C+^{13}C$ are given as a function of energy. The fraction of the reaction strength in each partial wave was computed from the transmission functions of an optical model using a shallow potential (see Section III.C.3). The salient features of these curves were found to be insensitive to the parameters of the optical potential. Curves are labeled by their orbital angular momentum quantum number.

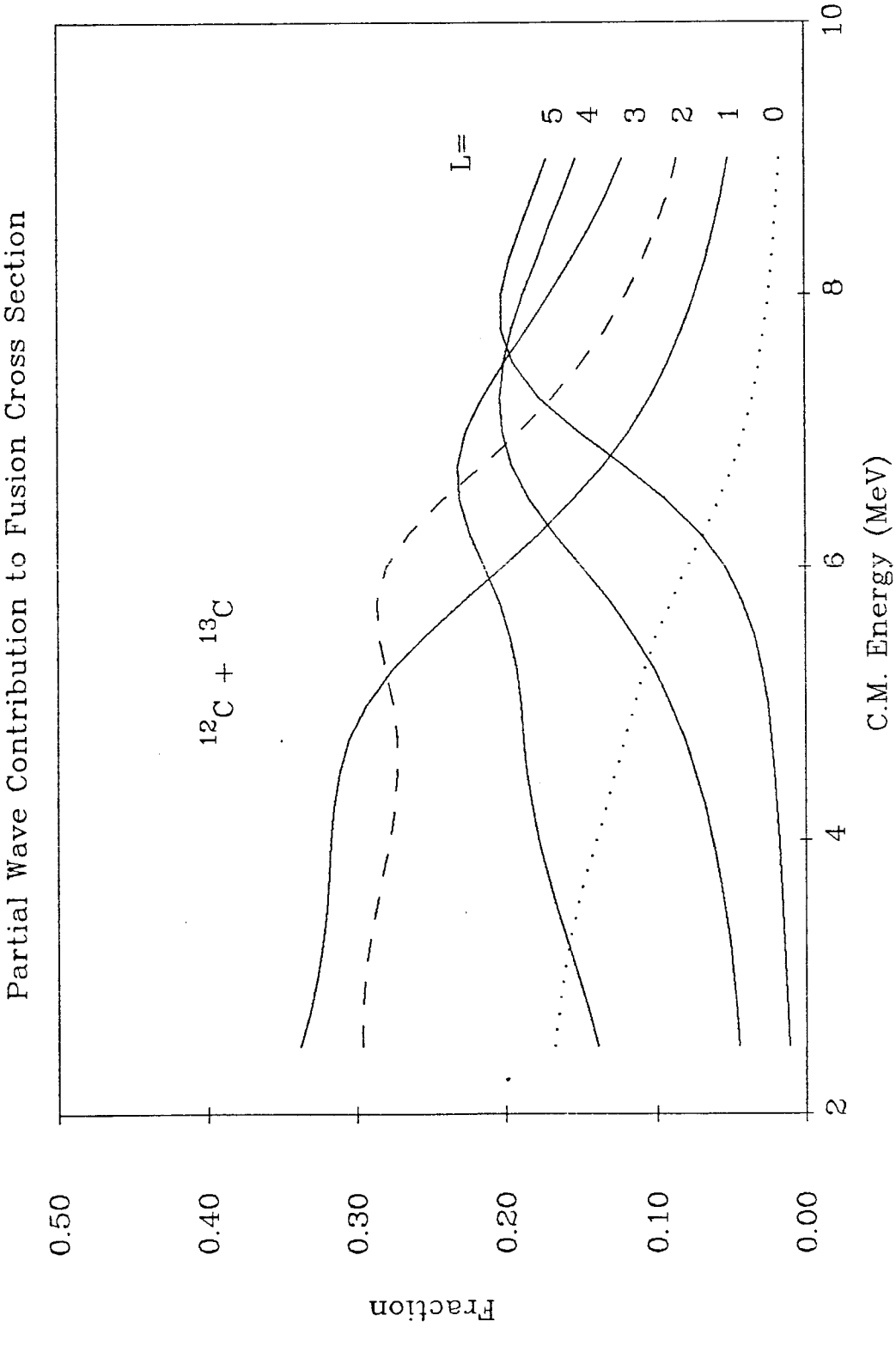
Partial Wave Contribution to Fusion Cross Section
$^{12}C + ^{13}C$
L=
5
4
3
2
1
0
Fraction
0.50
0.40
0.30
0.20
0.10
0.00
2
4
6
8
10
C.M. Energy (MeV)

FIGURE 28

CARBON ISOTOPE FUSION: STANDARD OPTICAL MODEL

The predictions of the standard optical model (solid curves) are compared to the fusion data for the systems $^{12}C+^{12}C$, $^{12}C+^{13}C$, and $^{13}C+^{13}C$. The symbols used to plot the data are defined in the caption to figure 24. The optical potential parameters are $V_0 = 50$ MeV, $W_0 = 10$ MeV, $r_0 = 1.27$ fm and $a = 0.40$ fm.

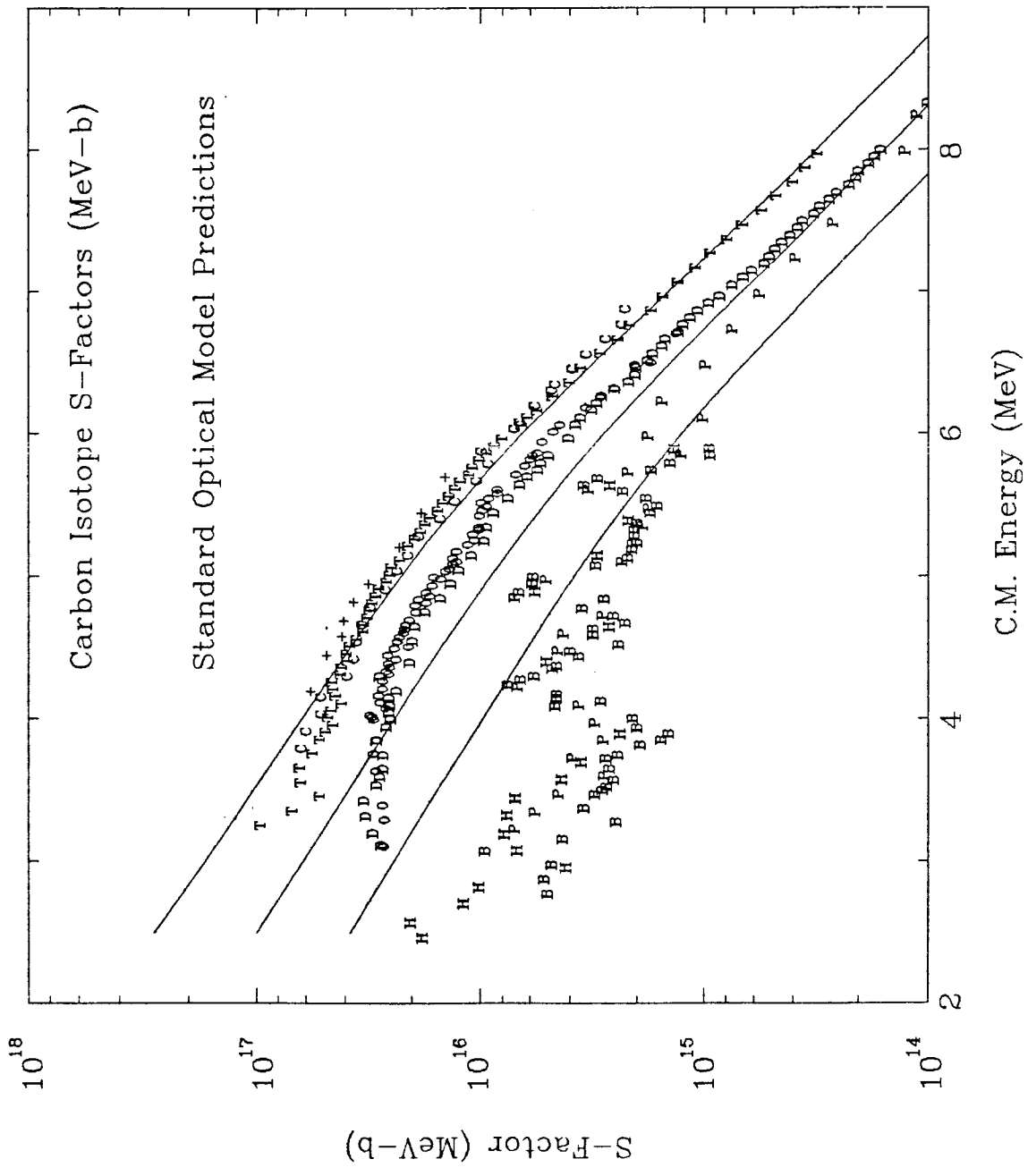
Carbon Isotope S-Factors (MeV-b)
Standard Optical Model Predictions
S-Factor (MeV-b)
C.M. Energy (MeV)
10^18
10^17
10^16
10^15
10^14
2
4
6
8

FIGURE 29

MODEL PREDICTIONS: ELASTIC EXCITATION FUNCTIONS

The ratio of the measured $^{13}C+^{13}C$ differential elastic scattering cross section to the Mott cross section are compared to model predictions at $\vartheta_{c.m.}$ = 60°, 70°, 80°,and 90°. The solid curves are the results of an IWBC calculation (a_{real} = 0.64 fm and R_{real} = 5.19 fm) described in Section III.C.2. The dotted curves are an optical model calculation using a shallow, energy-dependent potential of the form suggested by Korotky *et al.* (Ko81). The parameters have been adjusted to fit our data, giving V_{real} = 12.5 MeV, W_{imag} = 1.0 + 0.22 $E_{c.m.}$, R_{real} = R_{imag} = 6.35 fm, a_{real} = 0.52 fm, and a_{imag} = 0.30 fm.

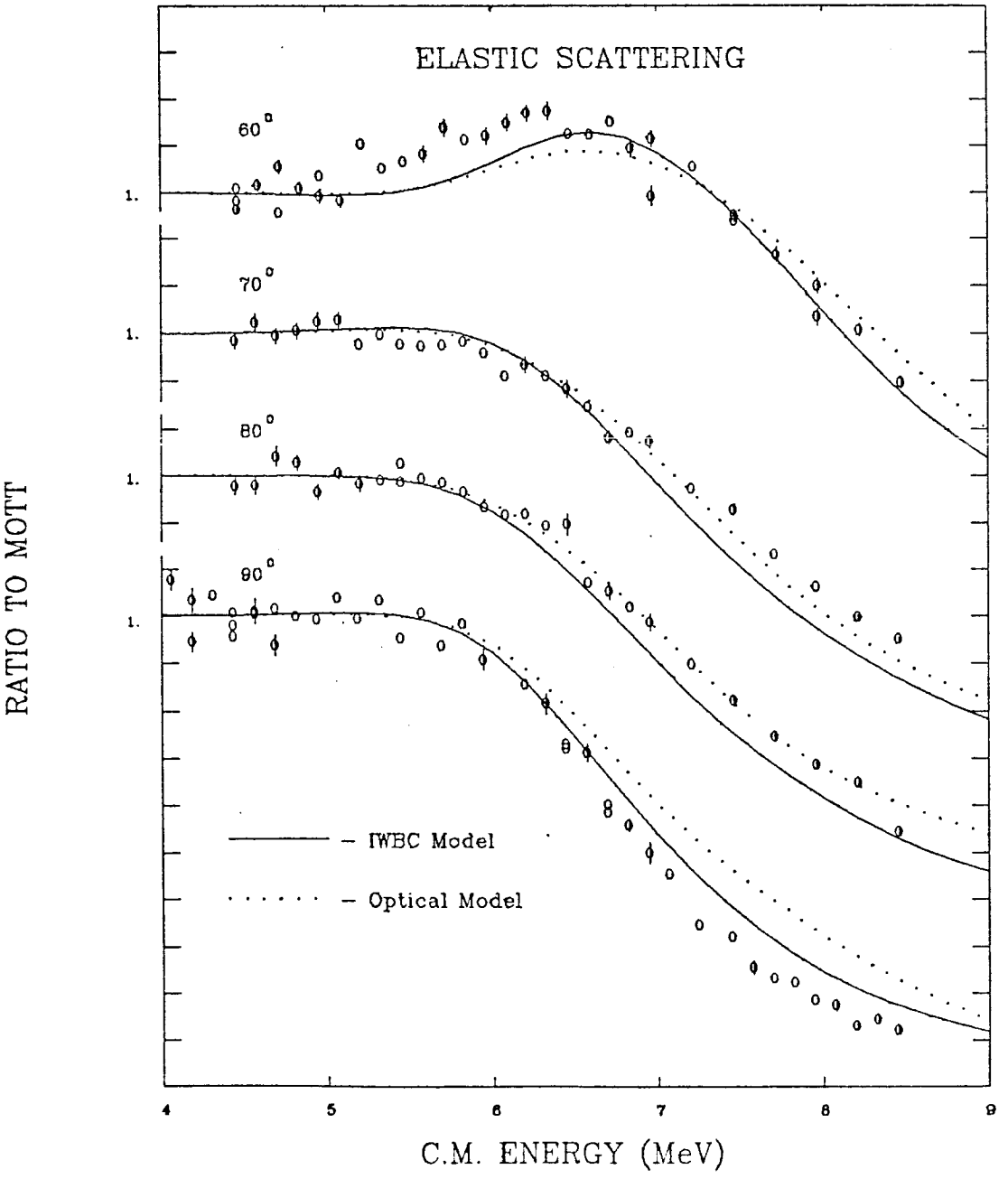
ELASTIC SCATTERING
60°
70°
80°
90°
1.
1.
1.
1.
— IWBC Model
· · · · · — Optical Model
4
5
6
7
8
9
C.M. ENERGY (MeV)
RATIO TO MOTT

FIGURE 30

MODEL PREDICTIONS: ELASTIC ANGULAR DISTRIBUTIONS

The elastic scattering angular distributions for $^{13}C+^{13}C$ are compared to model predictions at two energies, $E_{c.m.}$ = 7.0 MeV and $E_{c.m.}$ = 8.0 MeV. The solid curves are the results of an IWBC calculation (a_{real} = 0.64 fm and R_{real} = 5.19 fm) described in Section III.C.2. The dotted curves are an optical model calculation using a shallow, energy-dependent potential of the form suggested by Korotky *et al.* (Ko81). The parameters have been adjusted to fit our data; giving V_{real} = 12.5 MeV, W_{imag} = 1.0 + 0.22 $E_{c.m.}$, $R_{real} = R_{imag}$ = 6.35 fm, a_{real} = 0.52 fm, and a_{imag} = 0.30 fm.

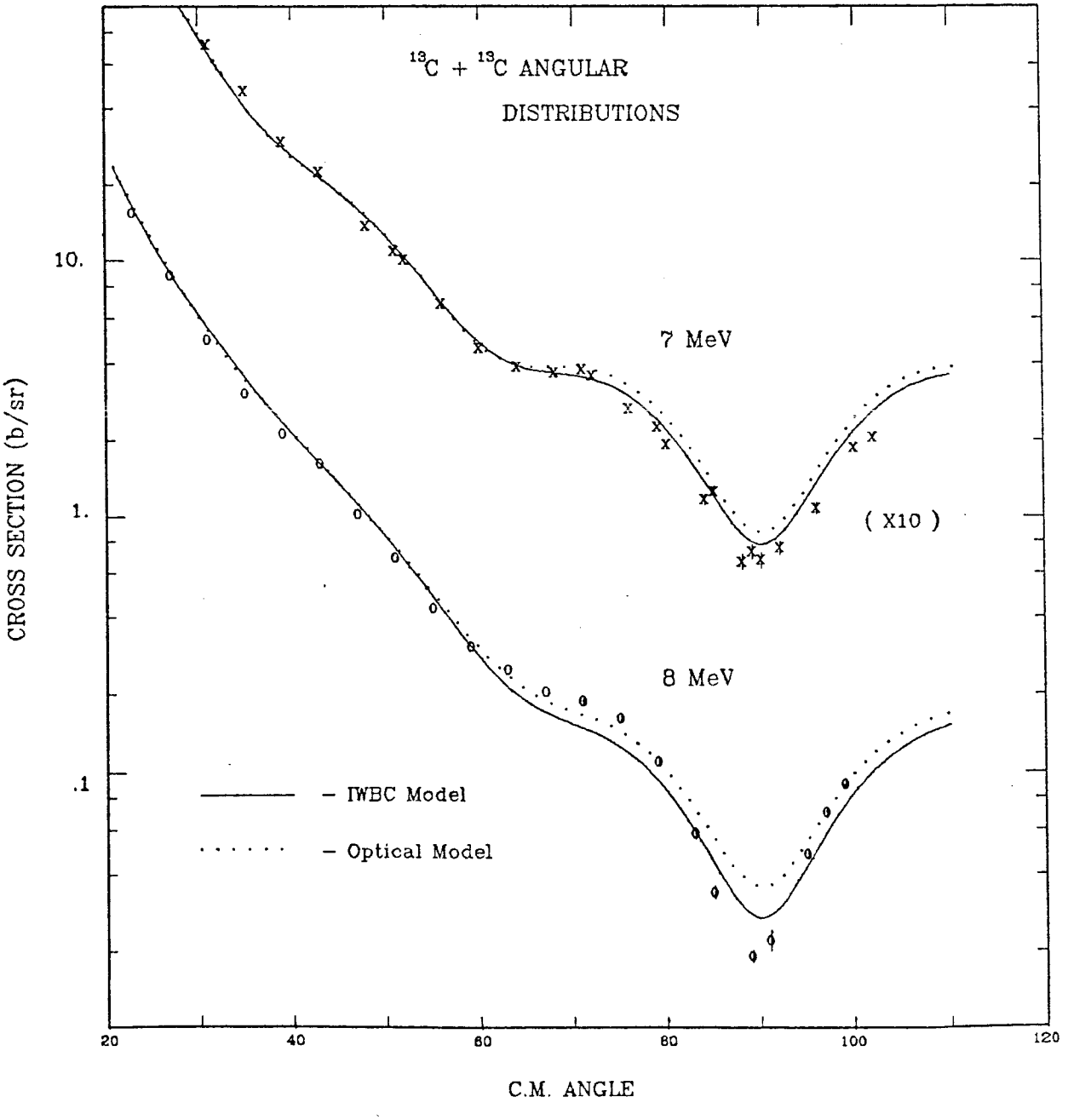
$^{13}C + ^{13}C$ ANGULAR
DISTRIBUTIONS
7 MeV
(X10)
8 MeV
– IWBC Model
– Optical Model
CROSS SECTION (b/sr)
10.
1.
.1
20
40
60
80
100
120
C.M. ANGLE

FIGURE 31

MODEL PREDICTIONS: FUSION S-FACTORS

The $^{13}C+^{13}C$ fusion S-factors are compared to model predictions. The solid curve is the result of an IWBC calculation (a_{real} = 0.64 fm and R_{real} = 5.19 fm) described in Section III.C.2. The dotted curve is an optical model calculation using a shallow, energy-dependent potential of the form suggested by Korotky *et al.* (Ko81). The parameters have been adjusted to fit our data; giving V_{real} = 12.5 MeV, W_{imag} = 1.0 + 0.22 $E_{c.m.}$, R_{real} = R_{imag} = 6.35 fm, a_{real} = 0.52 fm, and a_{imag} = 0.30 fm.

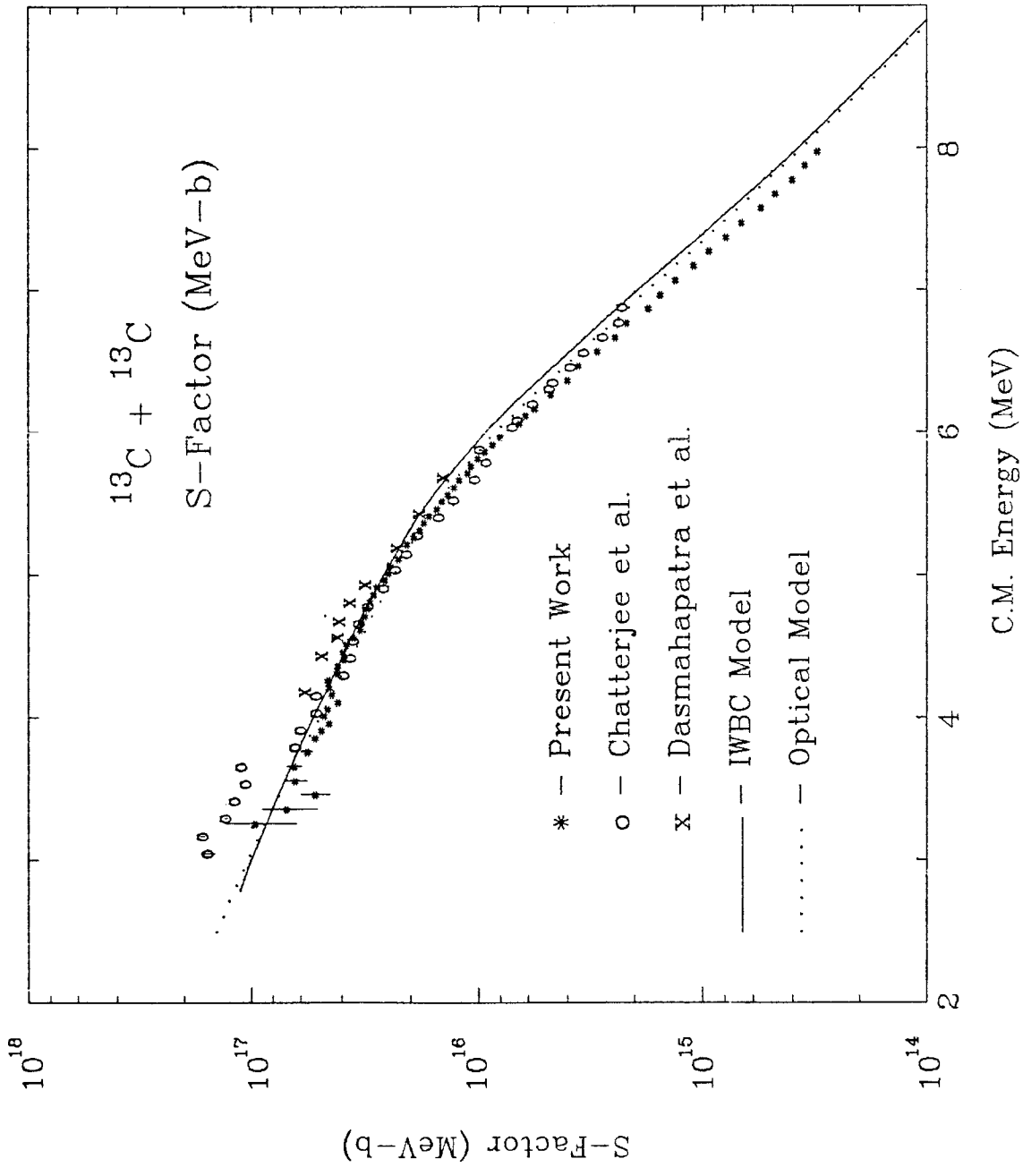
$^{13}C + ^{13}C$
S-Factor (MeV-b)
* - Present Work
o - Chatterjee et al.
x - Dasmahapatra et al.
—— - IWBC Model
..... - Optical Model
S-Factor (MeV-b)
C.M. Energy (MeV)
10^{18}
10^{17}
10^{16}
10^{15}
10^{14}
2
4
6
8

FIGURE 32

NEUTRON EXCHANGE POTENTIALS

Adiabatic potentials for single ($^{12}C+^{13}C$) and double ($^{13}C+^{13}C$) neutron exchange are plotted as a function of distance between the ^{12}C cores. In each system, the sign of the asymptotic potential alternates for even and odd L-waves. The *s*-wave potential is repulsive in $^{12}C+^{13}C$ and attractive in $^{13}C+^{13}C$. Fusion and elastic scattering are only sensitive to the behavior at large R, which changes the position and height of the barrier.

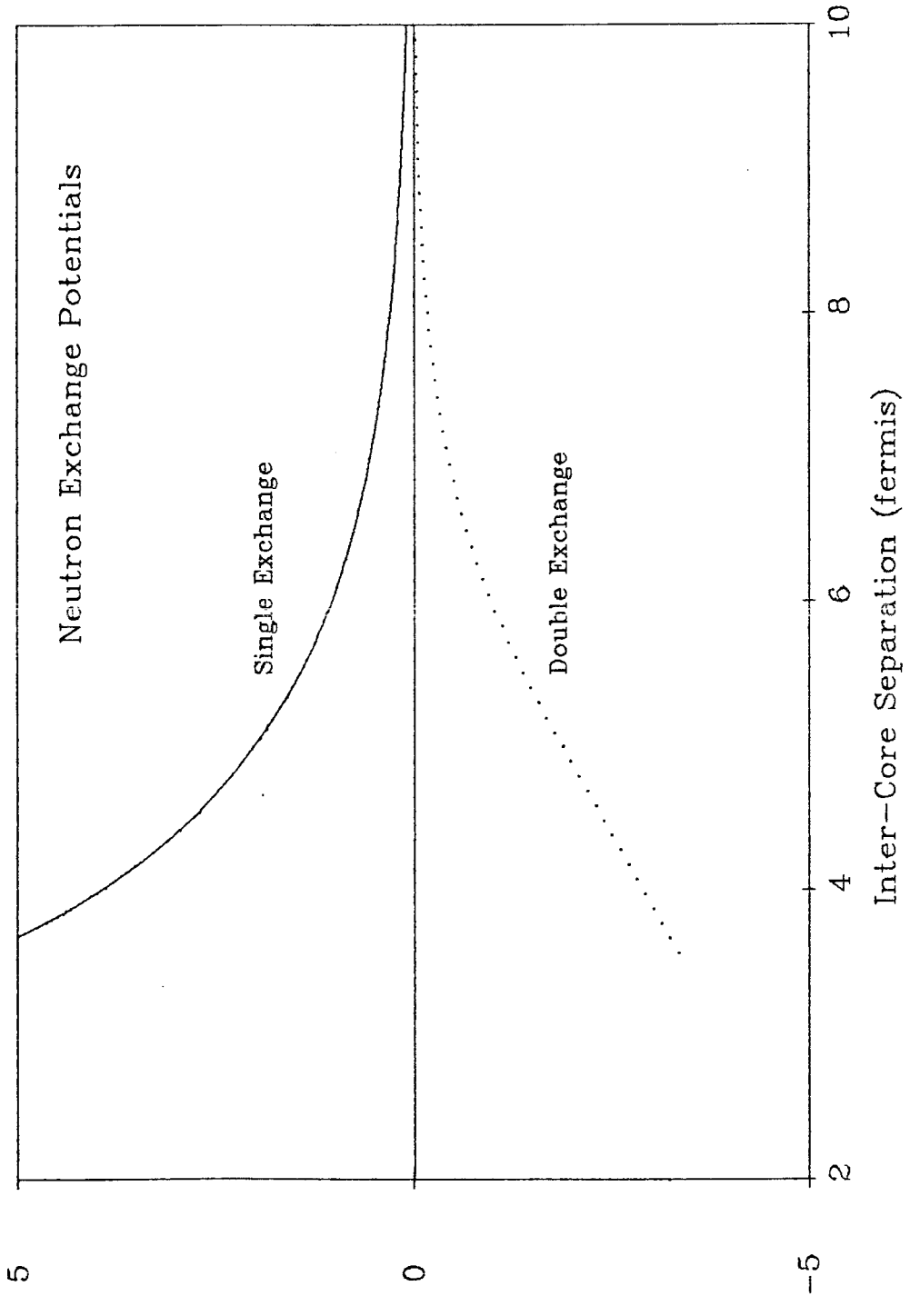
Neutron Exchange Potentials
Single Exchange
Double Exchange
Exchange Potential (MeV)
5
0
-5
2
4
6
8
10
Inter-Core Separation (fermis)

FIGURE 33

MWFM: ANGULAR DISTRIBUTIONS

The effect of neutron exchange on an optical model angular distribution is explored in $^{13}C+^{13}C$ elastic scattering for different values of [SN]. The MWFM curve oscillates about the optical model prediction. The most pronounced (fractional) effect occurs for angles near the minimum at 90°. The broad, central minimum produced by ordinary optical models is largely corrected for by the neutron exchange potential.

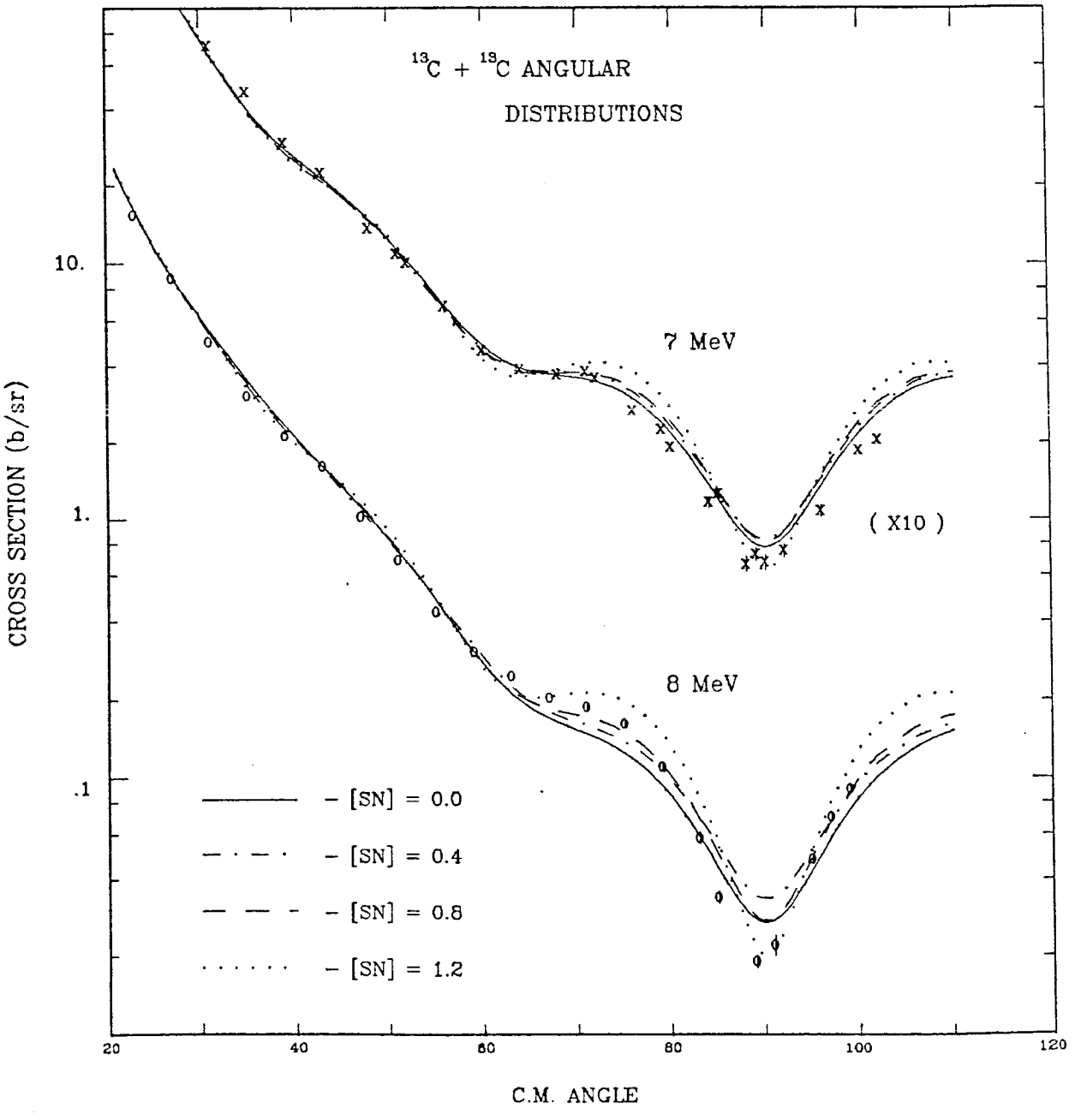
$^{13}C + ^{18}C$ ANGULAR
DISTRIBUTIONS
7 MeV
(X10)
8 MeV
– [SN] = 0.0
– [SN] = 0.4
– [SN] = 0.8
– [SN] = 1.2
CROSS SECTION (b/sr)
10.
1.
.1
20
40
60
80
100
120
C.M. ANGLE

FIGURE 34

MWFM: EXCITATION FUNCTIONS

The effect of neutron exchange on an optical model excitation function is explored in $^{13}C+^{13}C$ elastic scattering for different values of [SN]. The overall effect is to improve the fit to the 90° excitation function while exerting a lesser influence at other angles. The optical model parameters used were: V_{real} = 12.5 MeV, W_{imag} = 2.0, R_{real} = 6.35 fm, R_{imag} = 5.93 fm, a_{real} = 0.52 fm, and a_{imag} = 0.32 fm.

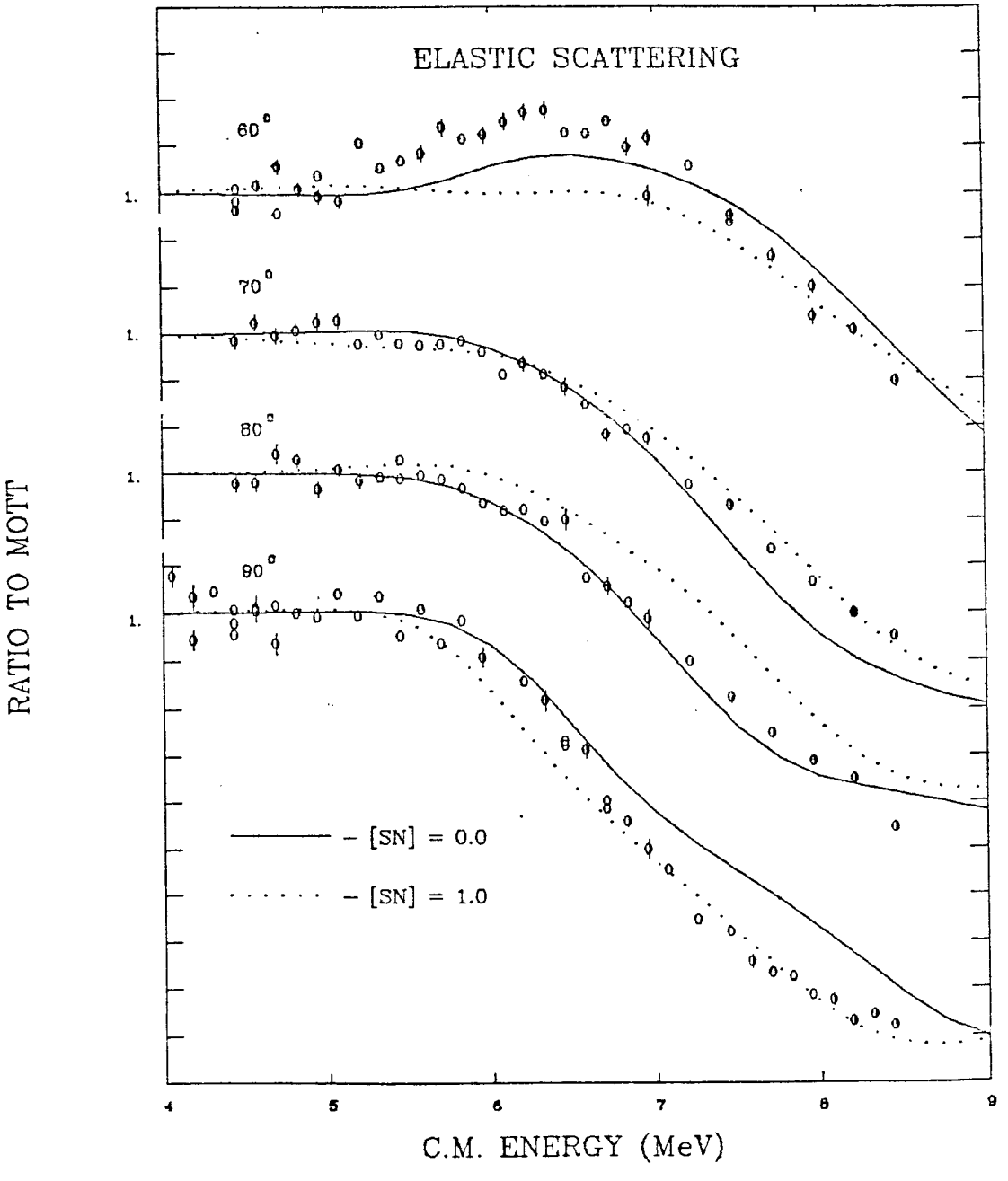
ELASTIC SCATTERING
60°
70°
80°
90°
1.
1.
1.
1.
– [SN] = 0.0
– [SN] = 1.0
4
5
6
7
8
9
C.M. ENERGY (MeV)
RATIO TO MOTT

FIGURE 35

MWFM: FUSION S-FACTOR

The effect of the neutron exchange potential on an optical model prediction is demonstrated for $^{13}C+^{13}C$ fusion. Here [SN]= 1.0, which corresponds to $S = 0.85$. The optical potential parameters are given in the caption to fig. 34.

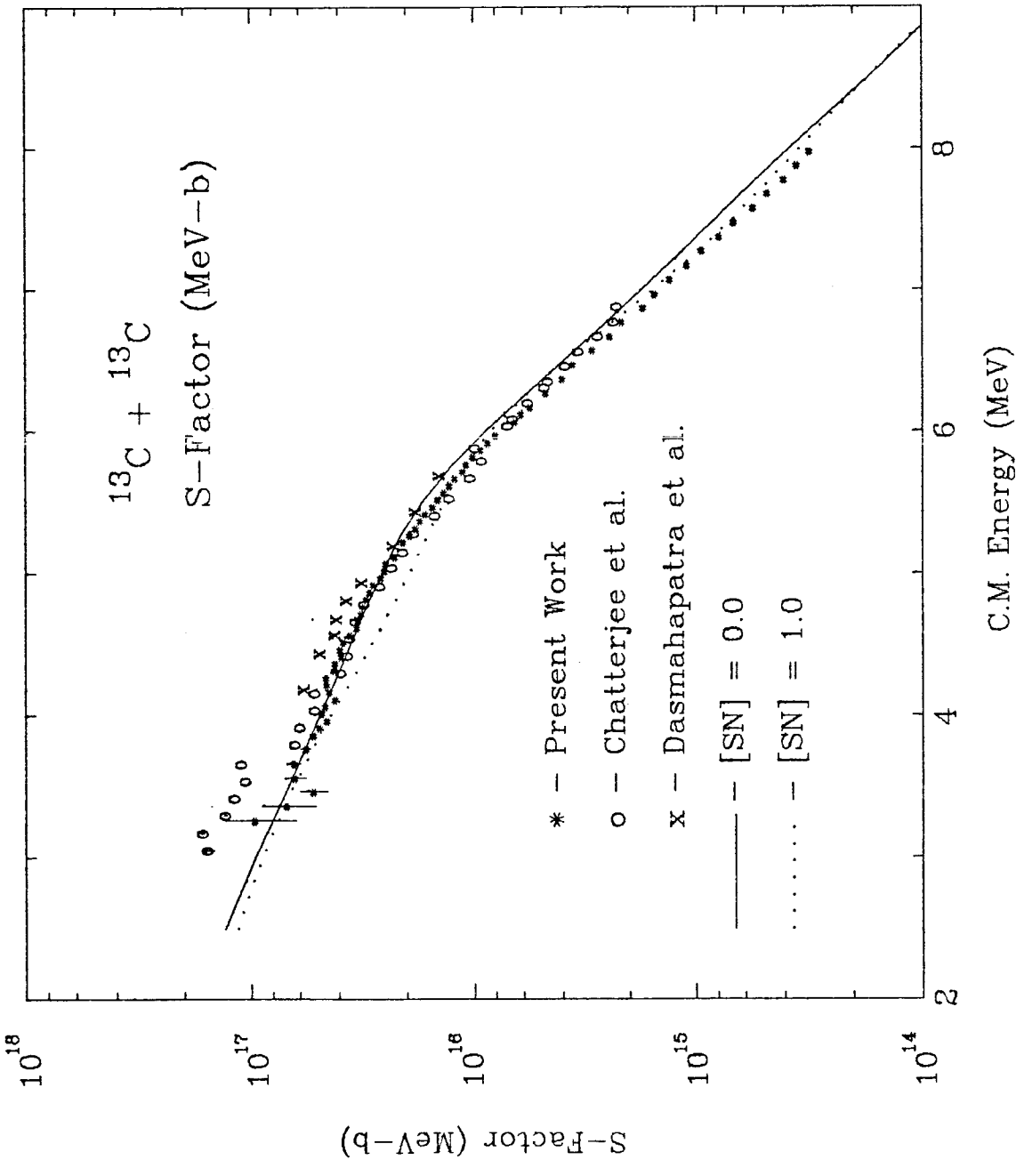
$^{13}C + ^{13}C$
S-Factor (MeV-b)
* - Present Work
o - Chatterjee et al.
x - Dasmahapatra et al.
—— - [SN] = 0.0
..... - [SN] = 1.0
S-Factor (MeV-b)
C.M. Energy (MeV)
10^{18}
10^{17}
10^{16}
10^{15}
10^{14}
2
4
6
8

FIGURE 36

TOTAL GE(LI) DETECTION EFFICIENCY

The total Ge(Li) detection efficiency as a function of γ energy was computed using equation II.B.3 for the detector/source geometry indicated in figure 6, and taking into account the absorption in the materials listed in Appendix A.

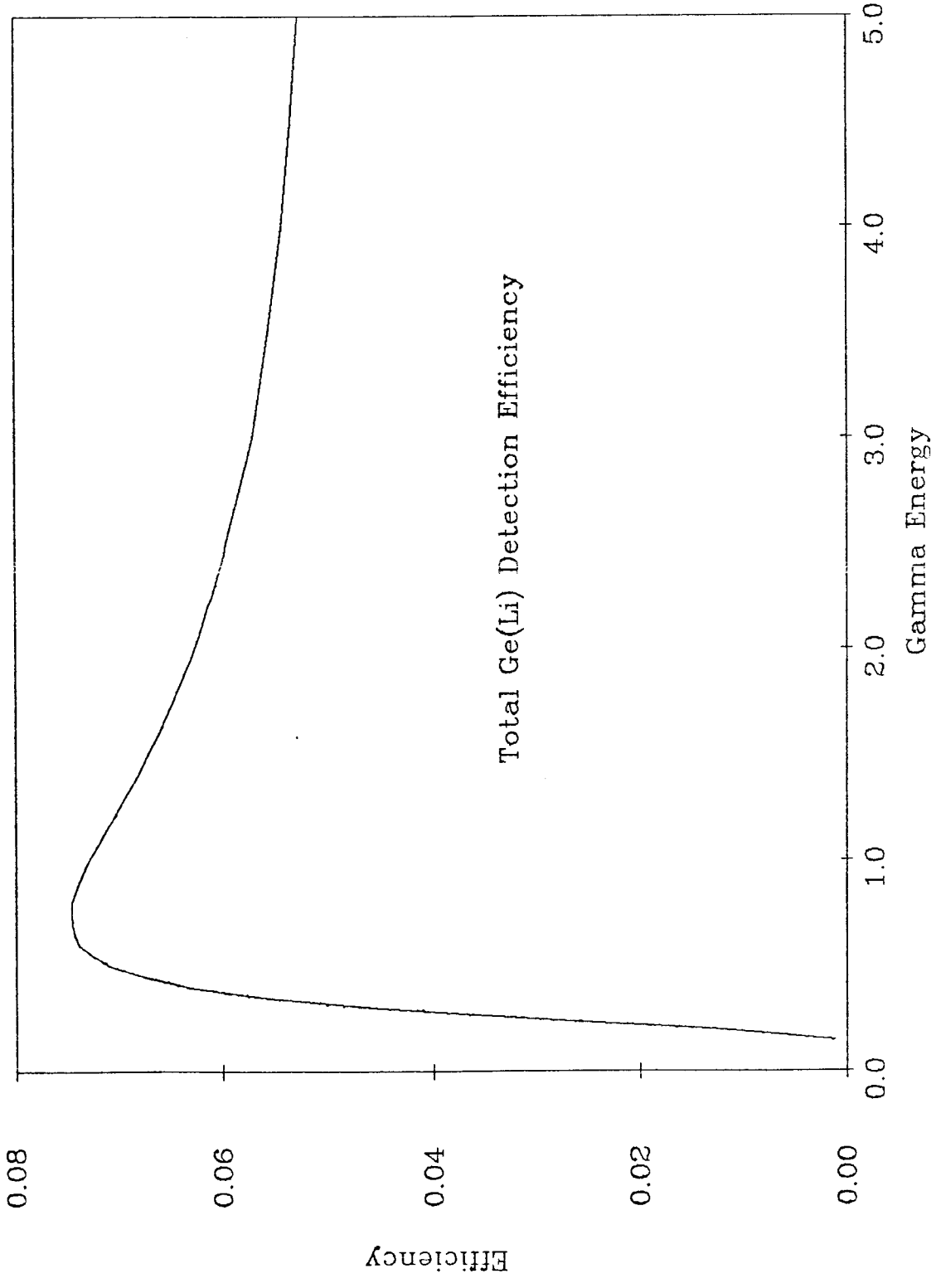
Total Ge(Li) Detection Efficiency
Efficiency
0.08
0.06
0.04
0.02
0.00
0.0
1.0
2.0
3.0
4.0
5.0
Gamma Energy